An Experimental Study of the Aerodynamic Characteristics of a Wing in Close Proximity to a Moving Ground Plane

Steven C. Rhodes

A dissertation submitted to the
Department of Mechanical Engineering,
University of Cape Town,
in fulfilment of the requirements for the degree of
Master of Science in Engineering.

March 2006

Declaration

I know the meaning of plagiarism and declare that all the work in this document, save for that which is properly acknowledged, is my own.

Signature of Author .. Signed by candidate ....

Cape Town

31 March 2006

Abstract

A wind-tunnel investigation was conducted to determine the effect of ground proximity on the aerodynamic characteristics of a slender un-cambered DHMTU rectangular wing of aspect ratio 3. A moving-belt ground plane and elevated aerodynamic balance facility were designed and installed in the UCT McMillan Laboratory open test-section wind tunnel. The lift, drag and pitching moment of the wing, were determined at a flow Reynolds number of 2.2×10^5 for relative ground clearances $0.06 < h_0 < 1.8$, and, angles of attack between -10 and 36 degrees. After the application of the required aerodynamic corrections, the lift, drag and pitching moment data was presented in coefficient form as a function of angle of attack and relative ground clearance. The results indicated that as the ground was approached the wing experienced an increase in the lift-curve slope and a reduction in induced drag, which resulted in an increase in the lift-drag ratio. The aerodynamic centre in height (ACH) was found to be predominantly behind the aerodynamic centre in pitch (ACP). At relative ground clearances, $h_0 < 0.5$, the data indicated significant movement of the ACH. It was concluded that this was a result of a temporary loss in lift as the ground was approached. The data from the analysis indicated that the static stability margin, SSM, was predominantly negative at all ground clearances. Based on these findings, the wing was concluded to be unstable in ground effect.

Acknowledgements

First and foremost I would like to thank my supervisor, Prof. Anthony Sayers, for all his time, patience and expertise throughout the course of the project. Furthermore, I would like to thank all the fellows in the workshop, namely; Glen, Len, Hubert, Horst, Peter, Dylan, Willie, Stanley and Julian, for all their great wisdom and good laughs. Special thanks to Anthony Langevelt from Polynates, for his advice and all the free products. The Postgraduate Funding Office and the Department of Mechanical Engineering must be acknowledged for funding and material assistance, without which, would not have made this project possible. Final thanks must go to my folks; their support has paved the way for opportunities I would otherwise have missed.

Contents

List of Figures

List of Tables

List of Symbols

AR	aspect ratio
b	wing span
B	test-section breadth
c	wing chord
C	test-section cross-sectional area
C_D	drag coefficient
C_{D0}	profile drag coefficient
$C_{D0.min}$	minimum profile drag coefficient
C_{Di}	induced drag coefficient
$C_{D.min}$	minimum drag coefficient
$C_{D.P}$	parasite drag coefficient
$C_{D.Pe}$	equivalent parasite drag coefficient
C_{DS}	drag coefficient due to separated flow
C_L	lift coefficient
$C_{L\alpha}$	$\partial C_L/\partial\alpha$
C_{Lh}	$\partial C_L/\partial h$
$C_{L.max}$	maximum lift coefficient
C_M	moment coefficient
$C_{M\alpha}$	$\partial C_M/\partial\alpha$
C_{Mh}	$\partial C_M/\partial h$
d	diameter of streamlined body
e	span efficiency factor
h	ground clearance
H	test-section height
h_0	relative ground clearance ($= h/c$)
K_1	body shape factor
L	test-section length
l	length of streamlined body
L/D	lift/drag ratio
L/D_{max}	maximum lift/drag ratio
M	pitching moment

$M_{ac.\alpha}$	moment about the aerodynamic centre in pitch
$M_{ac.h}$	moment about the aerodynamic centre in height
M_{tr}	moment about the trunnion
M_{wt}	moment correction due to model weight
q	dynamic pressure
R_e	Reynolds number
S	wing planform area
SSM	static stability margin ($= X_h - X_\alpha$)
t	maximum wing thickness
τ_1	tunnel-model shape factor
$[T\&I]_{low}$	tare and interference on the side of the wing-lower surface
$[T\&I]_{up}$	tare and interference on the side of the wing-upper surface
U	x - component of aircraft velocity vector
V	y - component of aircraft velocity vector
$\mathbf{V}$	aircraft velocity vector
Vol_{wing}	volume of wing
W	z - component of aircraft velocity vector
x	component axis on chordline
X_α	non-dimensional x- coordinate of ACP
X_h	non-dimensional x- coordinate of ACH
z	component axis perpendicular to chordline

α	angle of attack
α_e	equilibrium angle of attack
α_{up}	angle of attack due to upflow
$\alpha_{up.total}$	total angle correction
α_{L0}	zero-lift angle of attack
α_{stall}	angle of attack at stall
β	sideslip angle
ϵ_{sb}	solid blockage correction factor
ϵ_{wb}	wake blockage correction factor
ϵ_t	total blockage correction factor

Glossary

ACH	aerodynamic centre in height
ACP	aerodynamic centre in pitch
CFD	computational fluid dynamics
Ekranoplan	Russian term for ground-effect aircraft
LE	leading edge
MAC	mean aerodynamic chord
TE	trailing edge
VLM	vortex lattice methods
WIG	wing-in-ground-effect aircraft

Chapter 1

Introduction

1.1 Background to the Study

Ground effect is an aerodynamic phenomenon associated with a lifting surface operating in close proximity to another surface. Race cars typically use ground effect to increase the downforce exerted on the car, which leads to improved traction. Aircraft typically use ground effect to increase the lift exerted on the wing, which leads to a greater load carrying capacity. This report is concerned with the effect of the ground on a wing for use on an aircraft.

Aircraft operating in close proximity to the ground experience significant changes in the aerodynamic forces acting upon them. The result is usually characterised by an increase in the lift and decrease in the drag on the wing; otherwise, an increase in the lift/drag (L/D) ratio. It is recognised that most ground effect vehicles will more likely operate as water-based craft, travelling over the ocean. As a result, some vehicle design concepts are based on optimising an aircraft to safely fly close to the ground/sea, while, others make use of ground effect to improve the performance of fast boats. For this reason, these half-airplane/half-ship vehicles are collectively referred to as "Wing-In-Ground-Effect" (WIG) vehicles. Because of the history and strength of Russian technology in this field, many refer to WIG craft by its Russian equivalent Ekranoplan (ekran = screen, plan = plane).

1.2 History

The phenomenon today known as ground effect was observed very early in the birth of aviation. Pilots noted their aircraft tended to "float" in the air, when close to the ground during landing. As early as 1921, the German Wieselsberger[1] was already theoretically and experimentally analysing the effect of the ground on wings. In 1935, a Finnish engineer, Kaario, designed one of the first craft engineered to take advantage of ground proximity effects[2]. Throughout the Cold War era, the Russian Rostislav Alekseev and the German Alexander Lippisch made significant contributions to the field. However, it was not until 1967 that the West began to take serious notice of the benefits of ground effect. This occurred when a US analyst at the Defence Intelligence Agency identified a strange looking aircraft in some satellite imagery taken over Soviet soil, near the Caspian Sea[3]. For a long time, the very large plane was misunderstood as an incomplete aircraft due to its short, stubby wings. Only later was it identified as a craft engineered to take advantage of ground proximity effects, and became know as the *Caspian Sea Monster*. The Caspian Sea Monster, launched in 1966 and known as the KM by its chief designer, Rostislav Alekseev, was over 500 feet long and weighed 550 tons[4]. In 1995, a report illustrated the interest in WIG technology with one of the largest WIG craft envisaged to date[3]. An American company, Aerocon, conducted an investigation for the US Department of Defence on the WIG craft's potential for strategic mobility[1]. The prospective WIG craft, called the AR-1, had a gross weight 5000 tons, a payload capacity of 1500 tons and could cruise at over 400 knots (740 km/h). Compared to a Boeing 747, the AR-1 was 12 times the weight, but had 30 times the payload capacity, with a 44% improvement in operational efficiency[2]. Although the AR-1 was never built, this craft was conceived by the desire for a faster transportation platform over water. However, for several reasons to be identified later, the KM remains the largest WIG craft ever built to date.

1.3 Commercial Interest

WIG craft fill a large gap between low-cost/low-speed shipping and high-cost/high-speed aircraft. A well designed WIG craft will have a relatively high L/D ratio of 15 to 30, and a cruise speed of 100 to 400 km/h[4]. This results in a very attractive commercial and military transport platform, as identified by the KM and AR-1. The Von Karman-Gabrielli diagram of figure 1.1 (a), illustrates the L/D ratio of various vehicles as a function of speed[3]. The technology line represents the limit of the transport efficiency, the product of L/D and speed, for all current forms of transport. The shaded region clearly indicates the gap in transport efficiency, which WIG craft typically fall into. Furthermore, the cruise power requirements per unit weight, the P/W ratio, are very low for WIG craft[4]. This is also illustrated in figure 1.1 (b) in a comparison of WIG craft to other forms of transport.

---

[1] The ability to project force on a global scale.

[2] Payload capacity per unit fuel consumed.

[3] For land-based vehicles the lift is simply the total weight of the vehicle.

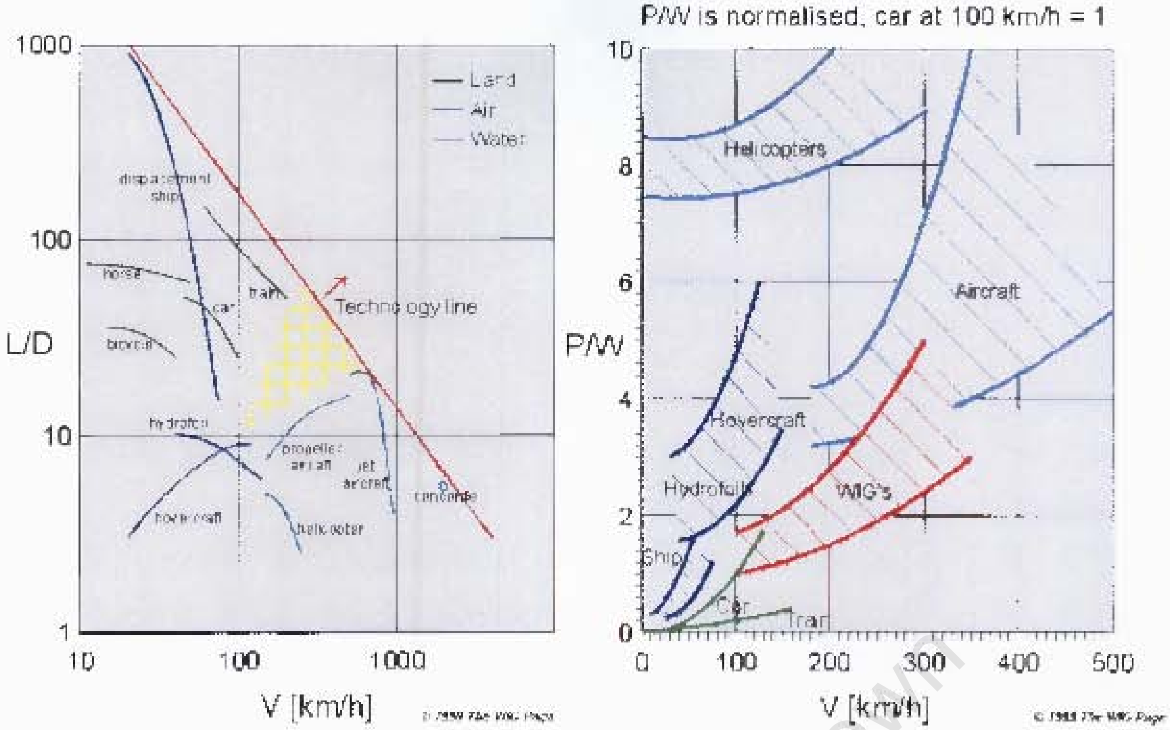

(a) (b)

Figure 1.1: Von Karman-Gabrielli Diagram and Vehicle Power Requirements [5]

However, there are several limitations in the understanding of the technology that impact the commercial viability of WIG craft[4]. Some of these limitations include;

1. WIG craft are sensitive to oceanographic and climate conditions; such as wave height and wind speed. Smaller WIG craft are more sensitive to these effects, and are thus typically less efficient.
2. All WIG craft are susceptible to pitch instability, which must be carefully examined during the design process.
3. Taking off and landing in the sea increases the design requirements in terms of the airframes structural integrity and additional engine power requirements to overcome the drag of the water.

These three areas have been the mainstay for much of the research conducted in previous years. The first two points listed above, have led to extensive research in the areas of aircraft configuration, planform and wing profile design. The third point has initiated research focused at minimising take-off power requirements through a reduction in the take-off drag. This is achieved through the hull design, the use of hydrofoils and power assisted static air cushions[4]. When operating in unfavourable climate conditions, the problems associated with these three points are minimised with very large WIG craft. However, the cost of developing larger craft may not be politically, economically or sociologically feasible. As was the case with the AR-1, with an estimated developmental cost of \$60 billion dollars and a production cost of \$400 million dollars per vehicle[3].

1.4 Purpose of this Investigation

As identified above, there are limitations in WIG craft technology. The purpose of this investigation is to develop the means for experimentally examining the forces and moments on a wing in close proximity to the ground. Furthermore, to examine the performance of a wing in the presence of the ground, and, examine the nature of the stability of the wing in terms of the current literature. The investigation is limited in that it only considers a single, arbitrarily chosen low aspect ratio wing. The experiments are conducted in the low subsonic flow regime, with a test Reynolds number of $R_e = 2.2 \times 10^5$. The results are presented and the nature of the stability determined in terms of the current literature. This report does not suggest any methods for improving wing performance, nor present any solutions for the stability problem usually associated with ground effect.

1.5 Description of the Main Problems Investigated

The main design problem was the design and construction of a moving-belt ground plane for use in the UCT McMillan Laboratory wind tunnel. The original configuration of the wind tunnel and associated instruments were adapted in order to accommodate such a ground simulation device. This involved the design of a support structure for positioning the existing three-component balance (L, D, M) in the over-tunnel configuration. Furthermore, a device for changing the elevation of the wing above the ground plane was designed, followed by the design of a new wing support system.

The main research problem was the study of a wing in the presence of the ground. The longitudinal performance of the wing in the presence of the ground was of primary importance. This involved the capture of the lift, drag and pitching moment versus angle of attack at varying ground clearance. A matrix of the lift, drag and pitching moment data was then generated as functions of angle of attack and ground clearance. The performance of the wing and the nature of the stability was then determined as the wing entered ground effect.

1.6 The Plan of development of the Thesis

The following chapter presents an overview of the basic aerodynamics in ground effect, the general theory of longitudinal static stability in ground effect and various simulation techniques for ground vehicle experiments. Chapter 3 discusses the treatment of flow interference in the test section. Chapter 4 identifies the existing characteristics of the UCT McMillan Laboratory Wind Tunnel. Chapter 5 discusses the design of the moving-belt ground plane and associated test apparatus. The full test procedure is discussed in chapter 6, followed by the presentation and discussion of the results in chapter 7. The final two chapters present the conclusions and recommendations derived from the results of the study.

Chapter 2

Ground Effect, Longitudinal Stability in Ground Effect and Ground Simulation Techniques

2.1 Introduction

Ground effect is an aerodynamic phenomenon associated with wings operating in close proximity to the ground. The phenomenon is characterized by two separate interactions[6]. The first concerns the interaction between the trailing vortex wake system and the ground. The second concerns the nature of the airflow under the body, which is strongly influenced by the interaction of the boundary layer forming on the underside of the body, with the boundary layer on the ground, if it exists, or with the ground itself. For positive angles of attack, below the stalled condition, the influence of the ground, in general, produces an increase in the lift-to-drag ratio. This arises as a result of the restriction in the development of the wing-tip vortices, and, an increase in pressure between the wing and the ground. This usually only becomes apparent at distances from the ground less than the length of the mean aerodynamic chord (MAC). For this reason, the ground clearance is usually non-dimensionalised relative to the MAC of the primary lifting surface of the aircraft in question. This description of the relative ground clearance will be denoted as $h_0 = h/c$, where h is the actual ground clearance and c represents the mean aerodynamic chord of the wing (see figure 2.1).

Although there is generally a measurable change in the forces at values of $h_0 = 1$, the effect tends to be most advantageous for the range of relative ground clearances below 25% chord. Rozhdestvensky[2] categorizes very small relative ground clearances of less than 10% chord as *extreme ground effect.* He sites these small relative

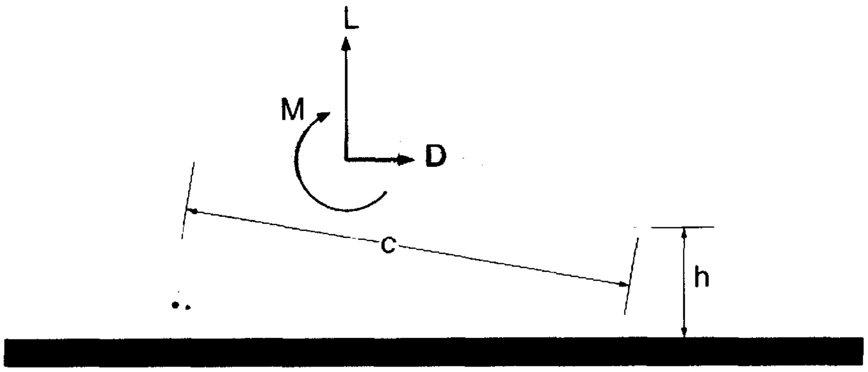

Figure 2.1: Measurement of ground clearance

ground clearances as the expected operational regime for future ground effect craft due to significant increases in wing efficiency.

2.2 The Flow Field in Ground Effect

A wing will normally develop a boundary layer over its upper and lower surfaces. Depending on the ground clearance, the presence of the wing will also induce a boundary layer on the surface of the ground as well as restrict the development of the trailing vortices. Barlow et al.[6] identifies several basic classifications that describe the clearance based on the level of interaction between the trailing vortex wake system and the ground, and, the level of interaction between the boundary layer on the wing and the ground. Together, with characterizations from van Opstal[4] and Rozhdestvensky[2], these classifications are broadly described as follows:

- Very Large Clearance ($h_0 < b, h_0 > c$). The presence of the ground begins to restrict the development of the trailing vortex wake system and push them outward (figure 2.2).
- Large Clearance ($h_0 \approx c$). The presence of the ground has a small influence on the velocity distribution under the wing and the development of the boundary layer on the wing. Induced flow is sufficiently small so that no significant boundary layer develops on the ground (figure 2.3).
- Medium Clearance ($h_0 \approx 0.5c$). The presence of the ground has a considerable influence on the wing and the wing induces a significant boundary layer on the ground. However, there still exits a well-defined region of potential flow between the two boundary layers (figure 2.4).

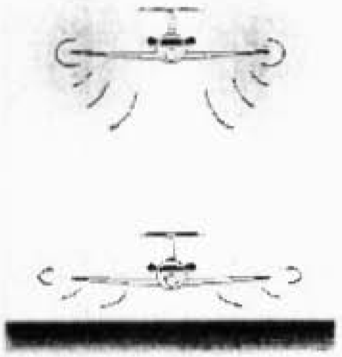

Figure 2.2: Flow field at very large ground clearances[4]

Figure 2.3: Flow filed at large ground clearances[6]

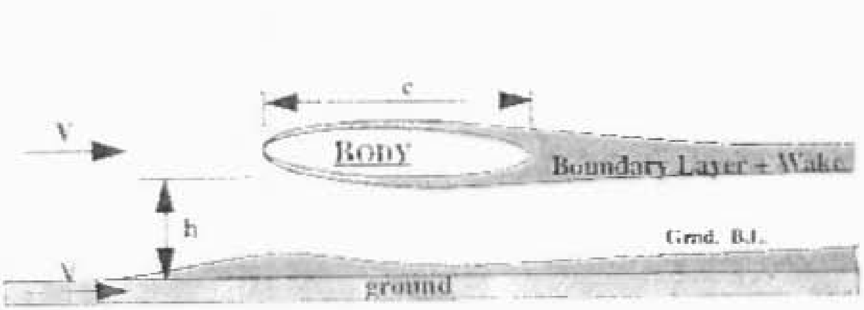

Figure 2.4: Flow filed at medium ground clearances[6]

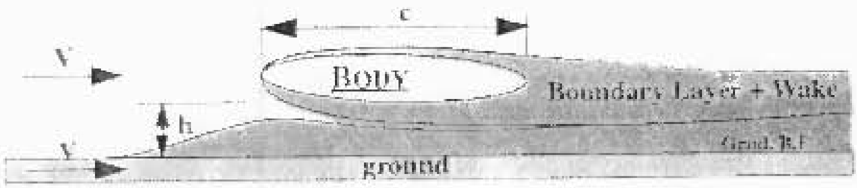

Figure 2.5: Flow filed at small ground clearances[6]

Figure 2.6: Flow filed at very small ground clearances[6]

- Small Clearance ($h_0 \approx 0.25c$). The two boundary layers are strongly interactive, but with little mixing within the streamwise extent of the wing. There is no potential flow separating the two boundary layers over much of the wing length (figure 2.5).
- Very Small Clearance ($h_0 < 0.1c$). Also known as extreme ground effect as $h_0 \rightarrow 0$. This is the limiting case where the airflow can stagnate below the wing. Viscous forces dominate the motion of the flow between the wing and the ground, convective terms in the Navier-Stokes equations become negligible and the flow becomes essentially creeping flow (figure 2.6).

2.3 Longitudinal Stability in ground effect

In 1935, a Finnish engineer, Kaario, designed one of the first craft engineered to take advantage of ground proximity effects[2]. His craft demonstrated a pitch instability, which is now recognised as an inherent characteristic of all ground-effect craft. The static longitudinal stability of lifting surfaces in ground effect is evaluated by an analysis of the derivatives of the lift coefficient, C_L, and the moment coefficient, C_M, with respect to the pitch angle, θ, and the relative ground clearance, h_0(equation 2.1 to 2.4). This analysis aids in understanding the nature of the response of an aircraft to various disturbances. The aforementioned derivatives are written in the following way for convenience;

$$C_{L\theta} = \frac{\partial C_L}{\partial \theta} \tag{2.1}$$

$$C_{M\theta} = \frac{\partial C_M}{\partial \theta} \tag{2.2}$$

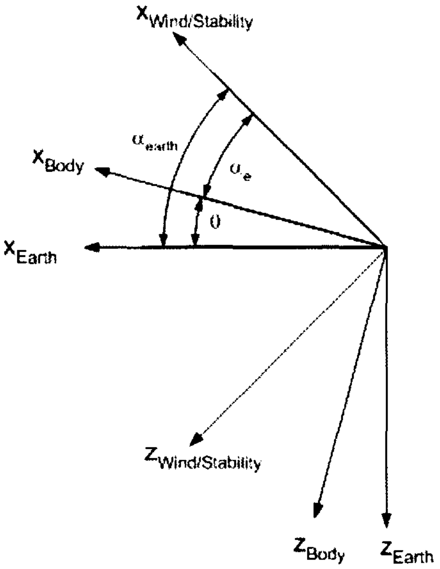

Figure 2.7: Angle of attack relative to earth-fixed co-ordinate system

$$C_{Lh} = \frac{\partial C_L}{\partial h_0} \tag{2.3}$$

$$C_{Mh} = \frac{\partial C_M}{\partial h_0} \tag{2.4}$$

At this point, it is important to recall the relationship between the pitch angle, θ, and the angle of attack, α. The pitch angle, θ, is the Euler angle measured between a reference earth-fixed coordinate system and a body-fixed coordinate system on the aircraft (see figure 2.7 and 2.8). The equilibrium angle of attack, α_e, is measured between the body-fixed axes and the stability axes[7]. Assuming zero sideslip angle, β, the stability axes are then aligned with the relative wind direction. Ignoring the effects of wind/gusts, α_e is then a function of the aircraft's forward and vertical velocity components and is given by;

$$\alpha_e = \arctan\left(\frac{W}{U}\right) \tag{2.5}$$

where the body-axes $[x\ y\ z]$components of the aircraft velocity vector are given by;

$$\mathbf{V} = [U\ V\ W]^T \tag{2.6}$$

The angle of attack, relative to the earth-fixed coordinate system is then given by (see figure 2.7);

$$\alpha_{Earth} = \theta + \arctan\left(\frac{W}{U}\right) \tag{2.7}$$

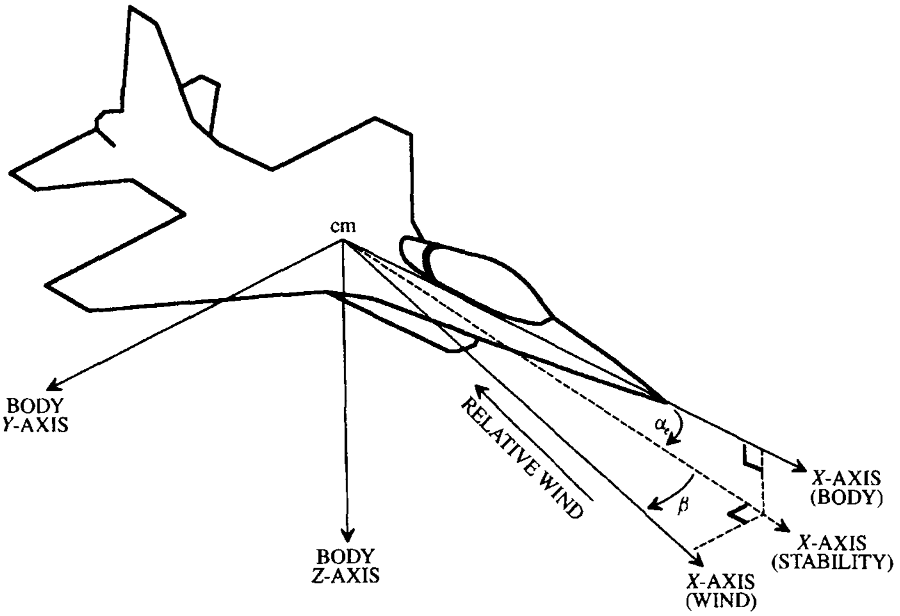

Figure 2.8: Aircraft Axes[7]

For an aircraft operating close to the ground, it is important to know whether α_{Earth} is a result of the pitch angle, θ, or of the vertical velocity component, W. For this reason, θ is the preferred variable for stability studies in ground effect, regarding the derivatives of C_L and C_M in equations 2.1 through 2.4. However, for the wind tunnel study in these experiments, the model is stationary. Therefore $\alpha_{Earth} = \theta$, and, for simplicity, the variable α will be used for the remainder of this report.

Rozhdestvensky[2] identifies, through the works of Irodov[8], Kumar[9], Staufenbiel[10] and Zhukov[11], that the longitudinal static stability of a wing in ground effect depends on the location of the aerodynamic centres in height and pitch, and the location of the centre of gravity. A discussion of these important parameters now follows.

2.3.1 The Aerodynamic Centre in Pitch

The aerodynamic centre in pitch (ACP) is the point where C_M remains constant with changing angle of attack, α. Its definition is:

$$X_\alpha = \frac{C_{M\alpha}}{C_{L\alpha}} \tag{2.8}$$

This expression gives the non-dimensional x-coordinates, relative to the moment axis, of the ACP as a function of α. If body-fixed axes are used, the positive direction of the x-axis is upstream and the values are given as a percentage of the wing chord.

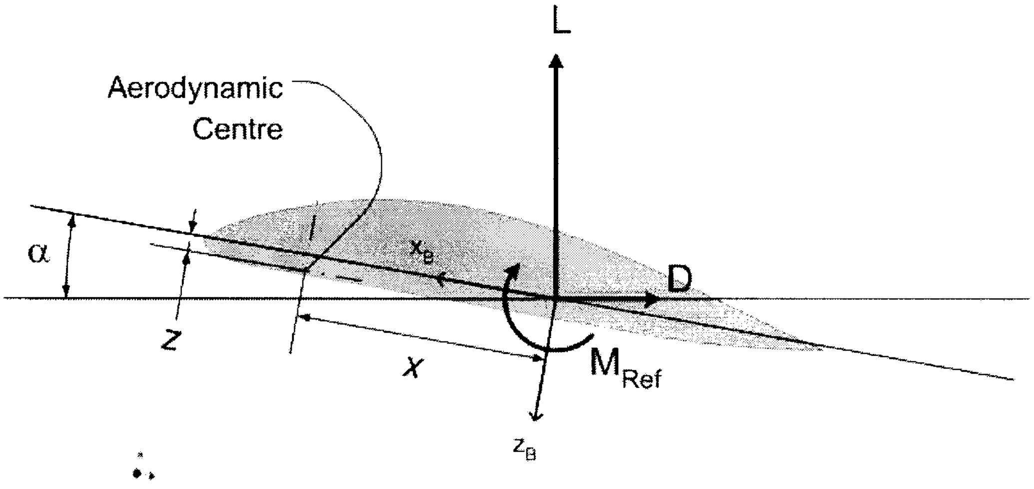

Figure 2.9: Calculation of aerodynamic centre

Since C_M and C_L are functions of h_0 as well, the value of $X_\alpha vs.\alpha$ must be calculated with the data from each value of h_0. The resolution of the ACP by equation 2.8, is limited in that it only defines the movement of ACP along the chordline (assuming the moment axis lies on the chordline). However, the ACP usually lies very close to the chordline. Therefore, the vertical displacement is frequently not calculated. The true location of the ACP can be calculated as follows (see figure2.9). If the distance along the chord from the reference moment axis to the ACP is x, the distance below the chordline is z and the mean wing chord is c, then the moment about the aerodynamic centre in pitch, $M_{ac.\alpha}$, is given by;

$$\begin{aligned} M_{ac.\alpha} &= M_{Ref} - xL\cos\alpha - zL\sin\alpha - xD\sin\alpha + zD\cos\alpha \\ &= M_{Ref} - x(L\cos\alpha + D\sin\alpha) - z(L\sin\alpha - D\cos\alpha) \end{aligned} \tag{2.9}$$

Where M_{Ref} is the reference moment axis. In coefficient form;

$$C_{M.ac.\alpha} = C_{M.Ref} - \frac{x}{c}\left(C_L\cos\alpha + C_D\sin\alpha\right) - \frac{z}{c}\left(C_L\sin\alpha - C_D\cos\alpha\right) \tag{2.10}$$

Differentiating with respect to C_L and applying the condition that the moment remains constant with C_L[1], the equation becomes;

$$\frac{\partial C_{M.ac.\alpha}}{\partial C_L} = 0 = \frac{\partial C_{M.Ref}}{\partial C_L}$$

---

[1] Since C_L is approximately proportional to α at small to medium angles of attack, can differentiate w.r.t. C_L or α.

$$-\frac{x}{c}\left[\left(1+C_D\frac{\partial\alpha}{\partial C_L}\right)\cos\alpha+\left(\frac{\partial C_D}{\partial C_L}-C_L\frac{\partial\alpha}{\partial C_L}\right)\sin\alpha\right]$$
$$-\frac{z}{c}\left[\left(C_L\frac{\partial\alpha}{\partial C_L}-\frac{\partial C_D}{\partial C_L}\right)\cos\alpha+\left(1+C_D\frac{\partial\alpha}{\partial C_L}\right)\sin\alpha\right] \quad (2.11)$$

Equation 2.11 has two unknowns. The substitution of the data, from two points/angles, allows for the simultaneous solution of the equation. However, this assumes the location of the ACP is constant with α[2]. Equation 2.8 should be considered if an analysis by this method indicates the ACP is not constant with α. It is interesting to note that if $C_D \ll C_L$ and α is small, which is normal under most cruise conditions, then equation 2.9 is approximated by;

$$M_{ac.\alpha} = M_{Ref} - xL$$

Differentiating this equation with respect to α and applying the condition that the moment remains constant with α;

$$\frac{\partial C_{M.ac.\alpha}}{\partial\alpha} = 0 = \frac{\partial C_{M.Ref}}{\partial\alpha} - \frac{x}{c}\left[\frac{\partial C_L}{\partial\alpha}\right]$$

$$\therefore \frac{x}{c} = \frac{\left[\frac{\partial C_{M.Ref}}{\partial\alpha}\right]}{\left[\frac{\partial C_L}{\partial\alpha}\right]}$$

therefore;

$$\frac{x}{c} = \frac{C_{M\alpha}}{C_{L\alpha}} = X_\alpha$$

2.3.2 The Aerodynamic Centre in Height

The aerodynamic centre in height (ACH) is the point where C_M remains constant with changing height. Its definition is:

$$X_h = \frac{C_{Mh}}{C_{Lh}} \quad (2.12)$$

This expression gives the non-dimensional x-coordinates, relative to the moment axis, of the ACH as a function of h_0. If body-fixed axes are used, the positive direction of the x-axis is upstream and the values are given as a percentage of the wing chord. Since C_M and C_L are also functions of α, the value of X_h *vs.* h_0 must be calculated with the data from each value of α. The resolution of the ACH using equation 2.12 is limited in that it only defines the movement of ACH along the chordline (assuming the moment axis lies on the chordline). However, the

---

[2] For small to medium angles of attack this is usually a good enough approximation.

ACH usually lies very close to the chordline. Therefore, the vertical displacement is frequently not calculated. The true location of the ACH can be calculated as follows (see figure 2.9). If the distance along the chord from the reference moment axis to the ACH is x, the distance below the chordline is y and the mean wing chord is c, then the moment about the aerodynamic centre in height, $M_{ac.h}$, is given by;

$$\begin{aligned} M_{ac.h} &= M_{Ref} - xL\cos\alpha - zL\sin\alpha - xD\sin\alpha + zD\cos\alpha \\ &= M_{Ref} - x(L\cos\alpha + D\sin\alpha) - z(L\sin\alpha - D\cos\alpha) \qquad (2.13) \end{aligned}$$

In coefficient form;

$$C_{M.ac.h} = C_{M.Ref} - \frac{x}{c}\left(C_L\cos\alpha + C_D\sin\alpha\right) - \frac{z}{c}\left(C_L\sin\alpha - C_D\cos\alpha\right) \qquad (2.14)$$

Differentiating with respect to h_0 and applying the condition that C_M remains constant with h_0, equation 2.14 becomes;

$$\begin{aligned} \frac{\partial C_{M.ac.h}}{\partial h_0} &= 0 = \frac{\partial C_{M.Ref}}{\partial h_0} \\ &\quad -\frac{x}{c}\left[\left(1 + C_D\frac{\partial\alpha}{\partial C_L}\right)\cos\alpha + \left(\frac{\partial C_D}{\partial C_L} - C_L\frac{\partial\alpha}{\partial C_L}\right)\sin\alpha\right] \\ &\quad -\frac{z}{c}\left[\left(C_L\frac{\partial\alpha}{\partial C_L} - \frac{\partial C_D}{\partial C_L}\right)\cos\alpha + \left(1 + C_D\frac{\partial\alpha}{\partial C_L}\right)\sin\alpha\right] \qquad (2.15) \end{aligned}$$

Equation 2.15 has two unknowns, and substitution of the data, from two values of h_0, allows for the simultaneous solution of the equation. However, this assumes the ACH is constant with h_0, but this is frequently not the case. Thus, equation 2.12 is preferred for resolving the ACH. It is interesting to note that if $C_D \ll C_L$ and α is small, which is normal under most cruise conditions, then equation 2.13 is approximated by;

$$M_{ac.h} = M_{Ref} - xL$$

Differentiating with respect to h_0 and applying the condition that C_M remains constant with h_0;

$$\frac{\partial C_{M.ac.h}}{\partial h_0} = 0 = \frac{\partial C_{M.Ref}}{\partial h_0} - \frac{x}{c}\left[\frac{\partial C_L}{\partial h_0}\right]$$

$$\therefore \frac{x}{c} = \frac{\left[\frac{\partial C_{M.Ref}}{\partial h_0}\right]}{\left[\frac{\partial C_L}{\partial h_0}\right]}$$

therefore;

$$\frac{x}{c} = \frac{C_{Mh}}{C_{Lh}} = X_h$$

2.3.3 The Stability Criterion

A ground-effect craft must be stable in both height and pitch. A disturbance in pitch angle or in height above the surface, must be compensated for by a restoring moment or force. This tendency to restore equilibrium is known as positive stiffness. Static pitch stability or positive pitch stiffness is associated with a negative slope of the C_M *vs.* α curve and is represented by;

$$C_{M\alpha} < 0 \tag{2.16}$$

For a trimmed aircraft, this provides a negative pitching moment for an increase in angle of attack. Static height stability is also associated with a negative slope of the C_L *vs.* h_o curves and this is represented by;

$$C_{Lh} < 0 \tag{2.17}$$

An increase in height would thus result in a decrease in lift. However, the above condition is only valid when C_M is held constant (held at zero for a trimmed aircraft). The moment coefficient usually changes with height, and this change must be taken into account. The condition for static height stability in longitudinal motion, given by Staufenbiel and Kleineidam[10] and Zhukov[11], representing the combined pitch and height stability criteria is;

$$C_{Lh} - \frac{C_{L\alpha}C_{Mh}}{C_{M\alpha}} > 0 \tag{2.18}$$

By assuming height stability, $C_{Lh} < 0$, the expression can be simplified to;

$$\frac{X_h - X_\alpha}{X_\alpha} > 0 \tag{2.19}$$

Irodov[8] effectively came to the same expression, indicating that static height stability is ensured if the aerodynamic centre in height is located upstream of the aerodynamic centre in pitch. It is important to note that equations 2.18 and 2.19 were derived with the coordinate system located at the trailing edge of the wing, and with the x-axis directed upstream. Therefore, the sign of X_h and X_α, and hence the inequalities, could be affected if the reference axis is located upstream of the trailing edge. However, Irodov's criterion for static height stability holds regardless of the reference point, specifically;

$$X_h - X_\alpha > 0 \tag{2.20}$$

The distance between the aerodynamic centres is referred to as the Static Stability Margin, $SSM = X_h - X_\alpha$, and is required to be positive for static height stability. The magnitude of the SSM also aids in predicting the nature of the response of the wing to a disturbance.

2.4 Ground Effect in Wind Tunnels

Rozhdestvensky[2] identifies two principal mathematical techniques for studying ground effect, namely, numerical methods and asymptotic approaches. Wieselsberger[1] was one of the first to apply asymptotic methods to ground effect by employing Prandtl's lifting line theory and the method of images. Rozhdestvensky uses the method of matched asymptotic expansions, first proposed by Widnall and Barrows[12], for the treatment of lifting surfaces in ground effect.

Numerical-based studies have made a significant contribution to the field of ground effect aerodynamics. Huminic and Lutz[13] used CFD methods to study ground simulation techniques. Chun and Park[14, 15] used potential based panel methods to predict the influence of waves on a wing, while Pienaar[16] used Vortex Lattice Methods (VLM) for his treatment of the aerodynamic forces and moments.

Experimental methods, usually carried out in wind tunnels, form an integral part of all aerodynamic studies. The treatment of the ground effect phenomenon in wind tunnels is very important. The complex flow field generated when a wing operates close to the ground, increases the need for reliable experimental data. Barlow et al.[6] identify several systems used for simulating the ground in wind tunnels, and are discussed below.

2.4.1 Fixed-Floor Wind Tunnel

A basic fixed-floor, closed test-section wind tunnel will have a developed boundary layer on the floor. The ratio of the relative wing ground clearance to the relative floor boundary layer thickness is critical. When the incoming floor boundary layer is thick, relative to the wing ground clearance, the flow about the wing can be significantly modified. Thus, measurements made with fixed-floor tunnels must be interpreted very carefully. Currently this is not a recommended practice.

2.4.2 Symmetry/Method of Images

The method is based on modelling the ground as a streamline (Euler wall). Two identical models are constructed. One is inverted relative to the other to form a plane of geometric symmetry. The plane then represents the ground. For model geometries and Reynolds numbers that result in a steady flow over larger ground clearances, the method of images is suitable for simulating a moving ground plane. However, symmetric geometry does not always produce a symmetric flow pattern, and the mean airflow is not always steady. Furthermore, this method does not simulate an induced ground boundary layer as expected at smaller clearances. Model costs are also doubled for each experiment. Barlow et al.[6] suggest the ratio of the model frontal area to test-section cross-sectional area should not exceed 7.5% unless errors of several percent are tolerable. Since two models are required, this guideline restricts the size of the model. Serebrisky and Biachuev[17] examine a Clark Y-H airfoil with AR 5 using this method. Fink and Lastinger[18] use this method to examine a rectangular wing of several aspect ratios.

2.4.3 Elevated Ground Plane

The elevated ground plane is a thin plate mounted parallel to the tunnel floor. It is usually positioned above the tunnel floor boundary layer. A new, thinner boundary layer then begins to form on the elevated plate. This technique is simple to implement, but the problem of the boundary layer still exits. Flow perturbations may arise due to the presence of the plate and hence cause changes in the flow field. The arrangement also causes a split flow on either side of the plate that is influenced by the model, which in turn makes accurate determination of the effective airspeed difficult. Support of the model can also be troublesome. This method was widely used until the 1970's but is rarely used today. Furlong and Bollech[19] analyse a sweptback wing using this method.

2.4.4 Raised Floor: Suction at Leading Edge

This method uses a blower/fan, mounted at the leading edge of a raised floor in the test-section, to remove the low energy air from the tunnel floor boundary layer. The air is re-injected back into the airstream at the downstream end of the test-section. The result is similar to that of the elevated ground plane; however, there are two main advantages. The floor and ceiling pressures can be made equal at the entrance to the test-section through control of the blower setting. This aids in improving the flow uniformity (i.e. reducing flow angularity). The raised floor need not be raised as much as the elevated ground plane, therefore having little impact on the effective area available in the test-section.

2.4.5 Suction through a Perforated Floor

There are two variations in the way the perforated floor is used. The first uses suction applied under a perforated floor segment upstream of the model. Depending on the amount of suction applied, the boundary layer thickness is reduced over the perforated segment. However, the boundary layer begins to grow again after the perforated segment. The result is similar to that of the raised floor with suction at the leading edge; however, there is a delicate balance between induced flow angularity and boundary layer thickness. Usually small amounts of suction are used in conjunction with other methods. The second variation utilises distributed perforations throughout the test-section. This system can remove the boundary layer altogether, but cannot simulate the moving ground plane with precision. Again, a compromise between induced flow angularity and boundary layer thickness must be made.

2.4.6 Tangential Blowing

With tangential blowing, air is injected parallel to the airstream, through a thin slot along the tunnel floor upstream of the model. The floor jet energises the boundary layer by replacing the lost momentum due to viscous effects. The boundary layer grows normally downstream of the jet. Tangential blowing has been found to produce drag results close to that of a moving ground, but other measurements can differ considerably.

2.4.7 Moving Ground Plane

This method uses a moving belt as the effective floor of the tunnel. In general, it is desired that the belt speed matches the air speed in the test-section. Operating conditions are simulated best; however, there are several disadvantages. Currently, there are few belt systems capable of approaching $100\,m/s$ due to the complexity and cost of such systems. The other disadvantage is that the model generally needs to be supported from the top or sides of the test section. Tests involving a low pressure difference between the model and the belt have a tendency to lift the belt off the floor. This must be counteracted by suction on the underside of the belt. Kim and Geropp[20] used a moving ground plane, in conjunction with a leading edge perforated floor, to examine the flow over two-dimensional bluff bodies. Turner[21] analysed the flow over two high lift models using a moving-belt ground plane in conjunction with a leading edge suction device, and, assisted by a perforated floor. Furthermore, he determined a physical limit, based on the lift to ground clearance ratio, for testing high lift models with an elevated ground plane. He found an elevated ground plane produced satisfactory results for $C_L < 10h_0$. For $C_L > 10h_0$, a moving-belt ground plane was recommended.

2.5 Concluding Remarks

The moving ground plane best simulates the flow conditions in ground effect. It is expected that the tests will be conducted at $h_0 < 0.1$ and $C_L > 1$. Thus, based on the recommendations of Turner[21], a moving ground plane should be used. As will be identified in the next chapter, the wind tunnel available for this experiment is relatively small and has a maximum airspeed of approximately $30\,m/s$. Thus, the demands on the ground plane are not as severe as larger, faster wind tunnels.

Chapter 3

Treatment of Flow Interference in the Test-section

3.1 Introduction

Flow conditions in a wind tunnel are never exactly the same as those that would be experienced by the same model in an open unrestricted environment. Two important factors that influence the flow conditions are;

1. the effects of the wing support system.
2. the effects of the test-section boundaries.

The tunnel airstream is usually not perfectly parallel and uniform throughout the test-section. There is usually some induced flow angularities due to the presence of the wing support system, windshields and the model itself, however, flow angularities may also exist in an empty test-section. The flow angularities can occur in any streamwise direction; that occurring in the vertical direction is collectively referred to as *upflow*, and that occurring in the horizontal direction is referred to as *cross-flow*. However, upflow is considered more important as it affects the accuracy of the drag. The existing "empty test-section" upflow and that induced by the presence of the model, is evaluated and corrected for in section 3.2. The interference caused by the interaction of the airflow with the wing support system, the windshields, *and* the model, is evaluated in section 3.3. It is important to note that in both cases the model configuration, the model attitude and dynamic pressure also influence the airflow; hence, each unique test requires a unique correction.

The presence of test-section boundaries, whether solid plus a boundary layer, or still air plus shear layers, produce several effects that would not be experienced in

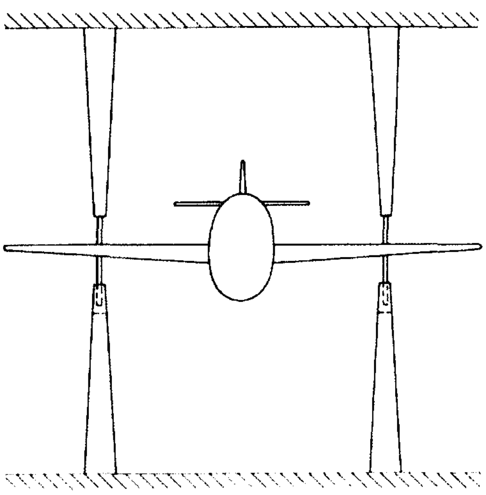

Figure 3.1: Model with image support system in place[6]

conventional flight environments. This could include the presence of a longitudinal static pressure gradient in the test-section, changes in dynamic pressure and alteration of the flow field around the wing. These effects are evaluated in section 3.4.

3.2 Aerodynamic Balance Alignment

Since upflow is influenced by the model configuration, the usual procedure is to align the balance so that the lift is perpendicular to the tunnel floor or ceiling, and the drag is parallel to it. The model is tested in the normal and inverted position, from zero lift to stall. To ensure equal support strut interference, a full mirror image of the support system and windshields is installed for both the normal and inverted test runs (figure 3.1).

The total angle correction made to the indicated angle is found from a plot of the normal and inverted C_L *vs.* α curves. The angular variation between the curves indicates twice the error in the recorded angle of attack (figure 3.2). The angular variation is only considered over the linear region of the C_L *vs.* α curves, usually $0.2 < C_L < 0.9$. The average angle correction derived from this region is called $\alpha_{up.total}$ and yields the true angle of zero lift when applied to the indicated angle of attack, α_{ind}.

The aerodynamic balance alignment is evaluated by considering a plot of the normal and inverted C_L *vs.* C_D curves. A rotation of the curves indicates the lift is not perpendicular and the drag not parallel to the local airflow (assuming the lift and drag are perpendicular). Considering the drag polar and force diagram of figure 3.3,

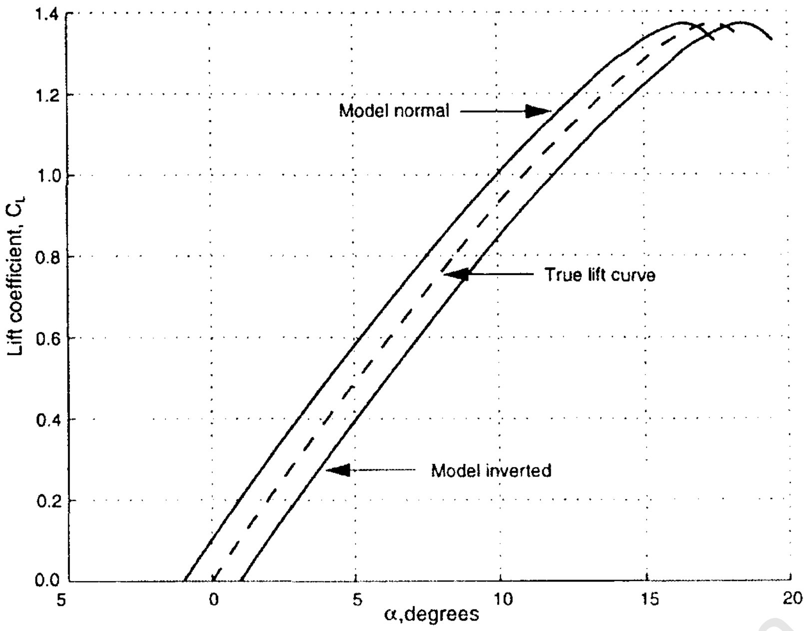

Figure 3.2: Angular displacement of lift curve[6]

part of the lift is appearing as drag; with the lift decreasing the drag when it is positive and increasing it when it is negative. The true drag value is related to the indicated value (wing normal) by the following expression (see figure 3.4):

$$\begin{aligned} C_{D.true} &= C_{D.ind} + C_{L.true}\sin\alpha_{up} \\ &= C_{D.ind} + C_{L.ind}\tan\alpha_{up} \end{aligned} \tag{3.1}$$

Therefore, α_{up} is found as follows;

$$\begin{aligned} \tan\alpha_{up} &= \frac{C_{D.true} - C_{D.ind}}{C_{L.ind}} \\ &= \frac{0.5\,(C_{D.inv} - C_{D.ind})}{C_{L.ind}} \\ &= \frac{0.5\Delta C_D}{C_{L.ind}} \end{aligned} \tag{3.2}$$

The correction to the indicated drag is given by:

$$D_{true} = D_{ind} + \Delta D \tag{3.3}$$

where;

$$\Delta D = L_{ind}\tan\alpha_{up} \tag{3.4}$$

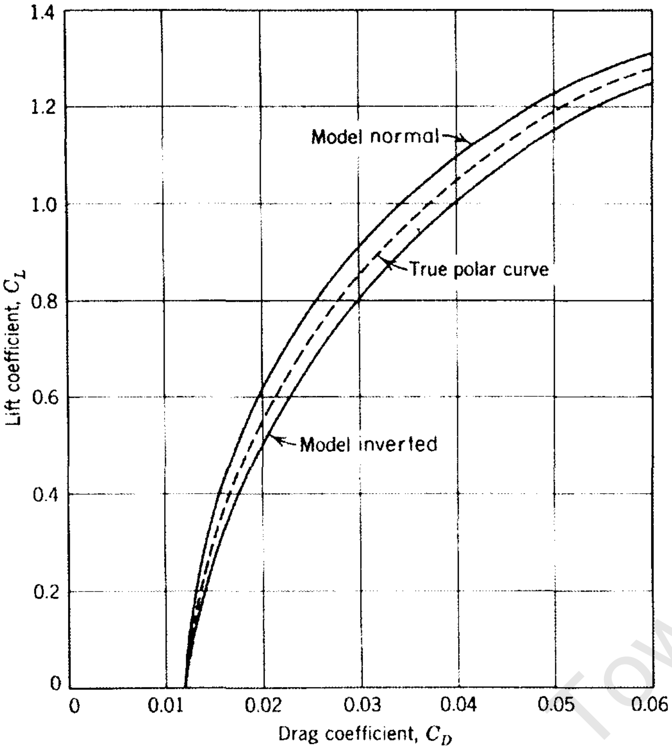

Figure 3.3: Angular rotation of polar curve[6]

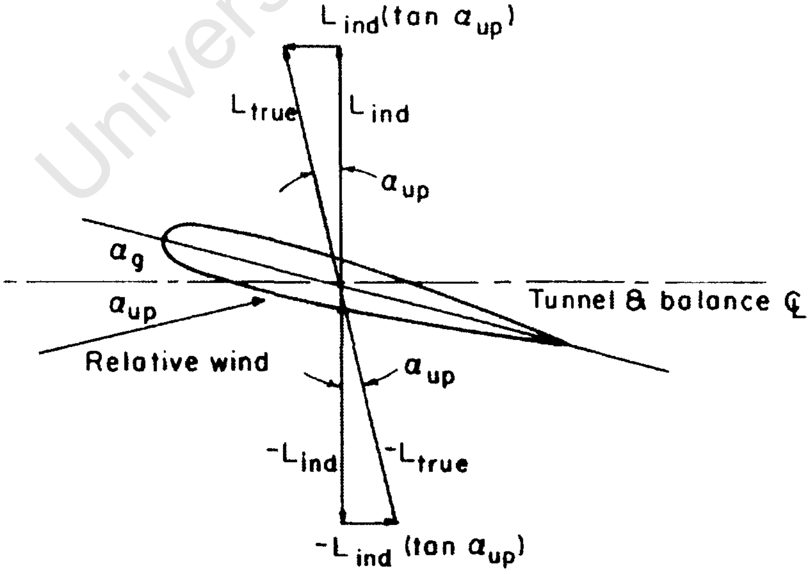

Figure 3.4: Force diagram depicting α_{up}.[6]

The true lift value is given by the expression:

$$L_{true} = \frac{L_{ind}}{\cos \alpha_{up}} \tag{3.5}$$

However, α_{up} is usually small enough such that $L_{true} = L_{ind}$ and no correction is applied. If the indicated angle of attack on the balance is correctly aligned with the incidence arm, the wing, and the tunnel floor, then $\alpha_{up.total} = \alpha_{up}$. This implies the angular correction is due to local flow angularities only. If they are not equal, an error exists between the alignment of the indicated angle, the pitching mechanism and the tunnel floor. The source of such errors should be assessed to determine its impact on the data. Nevertheless, the angular correction $\alpha_{up.total}$ includes α_{up}, and is the only correction applied to the indicated angle of attack.

$$\alpha = \alpha_{ind} + \alpha_{up.total} \tag{3.6}$$

3.3 Tare and Interference

The airflow around any model supported in a wind tunnel will be exposed to some level of interference due to the presence of the wing support system and any other devices in the airstream (such as strut windshields). The interference or modification to the airflow will affect the forces and moments on the model and must be properly accounted for. However, since different models and dynamic pressures also produce different flows, which interact with the wing support system, the level of interference on the forces and moments will be unique for different test conditions and model configurations. When the airstream is influenced by the wing support system, the effect is called interference, while the direct drag on the support structure is referred to as tare. The two effects are collectively referred to as, tare and interference ($T\&I$). For a particular model and dynamic pressure, the $T\&I$ effects can be found for the combined influence of the main and tail support struts (including windshields). This method required three tests with the wing in three different configurations, namely;

1. the wing supported in the normal configuration.
2. the wing supported in an inverted configuration.
3. the wing supported in an inverted configuration with a mirror image of the full support system in place.

The support system and windshields of a normal test run will influence the lift, drag and pitching moment as follows (figure 3.5):

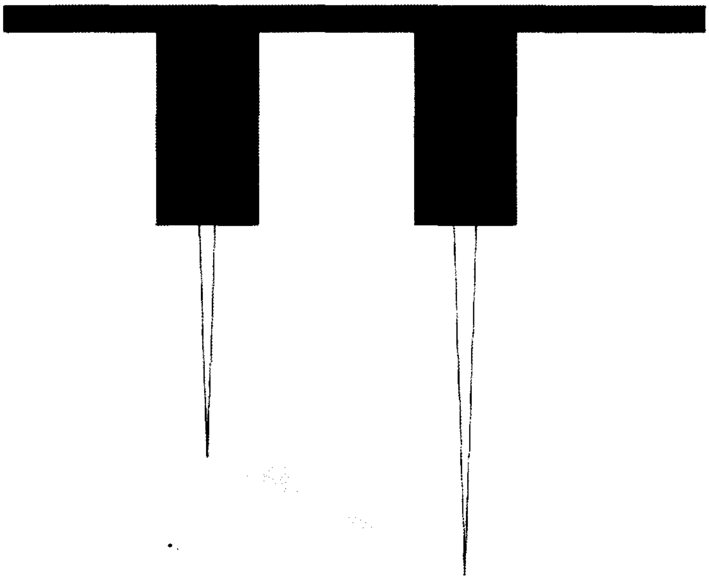

Figure 3.5: Wing in normal configuration

$$
\begin{aligned}
L_{ind} &= L_{norm} + [T\&I]_{up.L} \\
D_{ind} &= D_{norm} + [T\&I]_{up.D} \\
M_{ind} &= M_{norm} + [T\&I]_{up.M}
\end{aligned} \tag{3.7}
$$

where $[T\&I]_{up}$ represents the tare and interference for each component (L, D, M), due to the support and windshield system on the side of the *upper* surface of the wing. The inverted model will yield the following (figure 3.6):

$$
\begin{aligned}
L_{ind} &= L_{inv} + [T\&I]_{low.L} \\
D_{ind} &= D_{inv} + [T\&I]_{low.D} \\
M_{ind} &= M_{inv} + [T\&I]_{low.M}
\end{aligned} \tag{3.8}
$$

where $[T\&I]_{low}$ represents the tare and interference due to the support and windshield system on the side of the *lower* surface of the wing. The inverted model with the image support system and windshields gives the combination of the two effects, namely (figure 3.7):

$$
\begin{aligned}
L_{ind} &= L_{inv} + [T\&I]_{low.L} + [T\&I]_{up.L} \\
D_{ind} &= D_{inv} + [T\&I]_{low.D} + [T\&I]_{up.D} \\
M_{ind} &= M_{inv} + [T\&I]_{low.M} + [T\&I]_{up.M}
\end{aligned} \tag{3.9}
$$

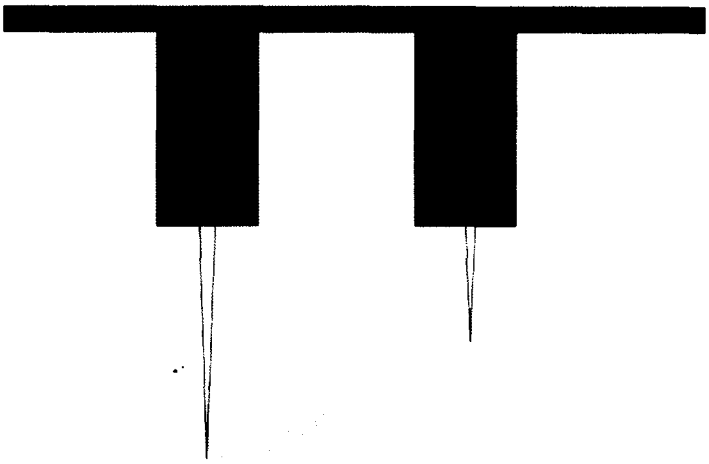

Figure 3.6: Wing in inverted configuration

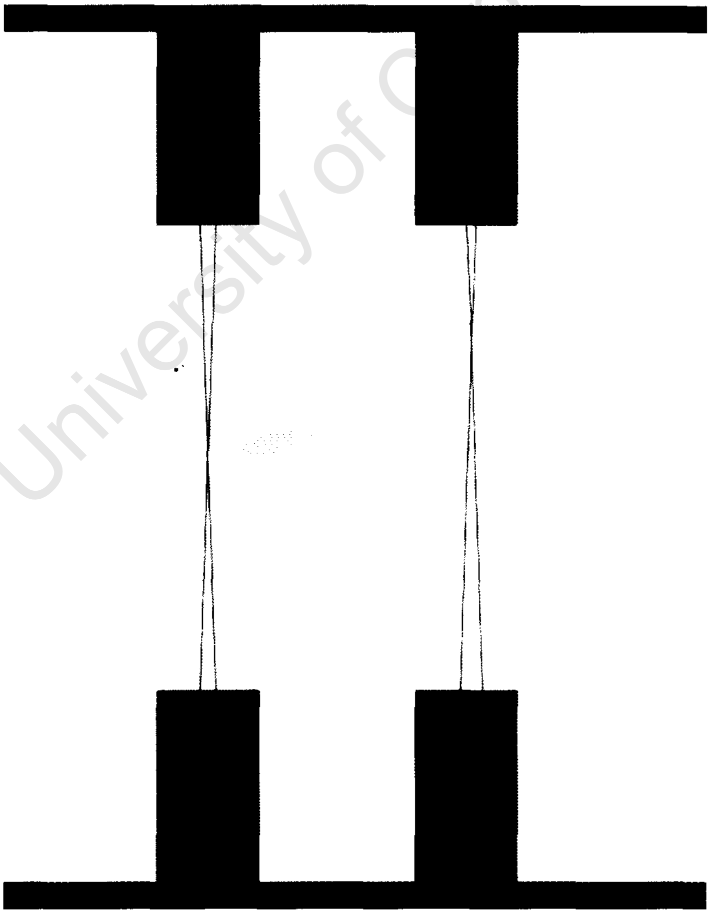

Figure 3.7: Wing inverted with full image support system

The difference between equations 3.9 and 3.8 yields $[T\&I]_{up}$, for each component, experienced by the wing supported in the normal configuration. The values of $[T\&I]_{up}$, which change with angle of attack, are simply subtracted from the wing-normal data represented by equation 3.7. It is required that all the above corrections are applied before boundary corrections are evaluated.

3.4 Boundary Corrections

The existence of the test-section boundaries produces several effects not experienced in conventional aircraft environments. Since these effects are a consequence of the finite size of a wind tunnel test-section, many of these effects are minimised by reducing the model size to tunnel size ratio. The relevant boundary corrections are evaluated as listed below[6];

1. horizontal buoyancy
2. solid blockage
3. wake blockage
4. normal downwash correction
5. tail downwash correction
6. streamline curvature
7. spanwise downwash distortion

The experiments described in this thesis are conducted in an open test-section wind tunnel, with a moving belt installed to simulate the effect of the ground. For ground effect studies, the force and moment data is usually only corrected for solid and wake blockage and, if required, horizontal buoyancy[6]. The remainder of the boundary corrections are usually not applied since the model is close to the tunnel floor. Thus, the remaining boundary effects due to the side walls and ceiling are considered negligible in comparison to the ground effects. Many open test-section tunnels have approximately zero horizontal buoyancy. As will be identified later, the static pressure gradient, and hence the horizontal buoyancy, are approximately zero for the tunnel used in these experiments. Horizontal buoyancy is also usually considered insignificant for wing only experiments. For these reasons, the horizontal buoyancy correction term is also neglected.

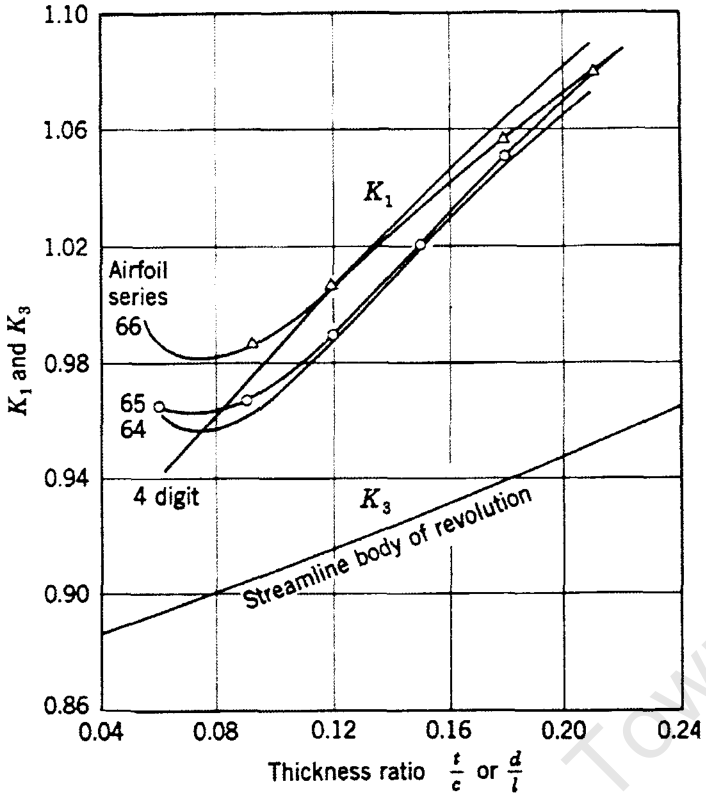

Figure 3.8: Body Shape Factor[6]

3.4.1 Solid Blockage

Solid blockage refers to the ratio of the model frontal area to test-section area. The ratio is effectively zero in free-air; however, in a wind tunnel it is advisable to limit the ratio to less than 7.5%[6]. Relative to the free-air condition, solid blockage causes an increase in the surface shear stresses in a closed test-section, and a reduction in surface shear stresses in an open test-section. The effect is more pronounced in closed test-section tunnels and is compensated for by considering the effect to produce a change in the dynamic pressure, q, at the wing. Thus, the correction for this effect is made to the dynamic pressure before the forces and moments are reduced to coefficient form. For a wing in a closed test-section:

$$\epsilon_{sb.closed} = \frac{K_1 \tau_1 Vol_{wing}}{C^{1.5}} \tag{3.10}$$

Where;

- K_1 – body shape factor (figure 3.8)
- τ_1 = tunnel-model shape factor (figure 3.9)
- Vol_{wing}– volume of the wing

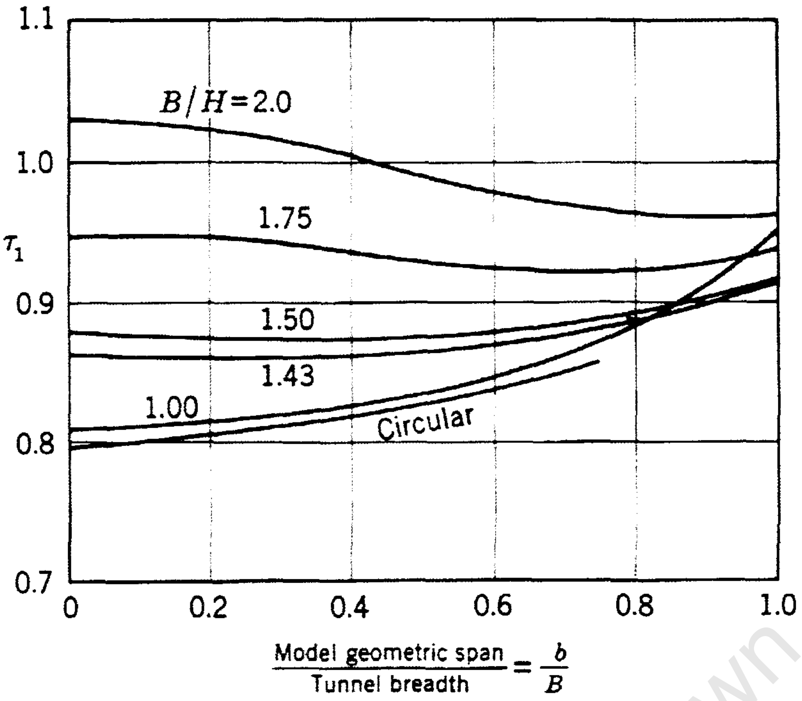

Figure 3.9: Tunnel-Model Shape Factor[6]

- C = frontal area of test-section
- $\frac{t}{c}$= max wing thickness to chord ratio
- $\frac{d}{l}$ = streamlined body diameter to length ratio

For an open test-section:

$$\epsilon_{sb.open} = -0.25\epsilon_{sb.closed} \tag{3.11}$$

If the airfoil volume is not known, the following estimate is considered acceptable[6];

$$Vol_{wing} = 0.7(t)(MAC)(b) \tag{3.12}$$

Where;

- t = maximum wing thickness
- MAC = mean aerodynamic chord
- b = wing span

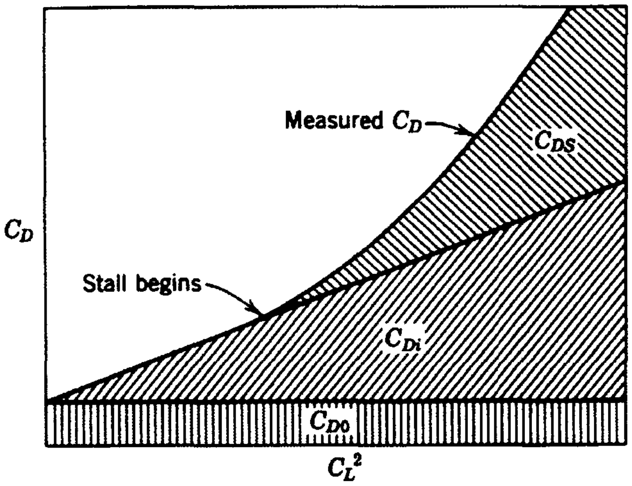

Figure 3.10: Drag components given by Maskell[6]

3.4.2 Wake Blockage

Wake blockage describes an increase in drag due to a wake-induced pressure gradient in the streamwise direction. The magnitude of this effect is a function of the wake size, which in turn, is a function of the model shape and the ratio of the wake area to test-section area. For a given model and dynamic pressure, the wake blockage will then be a function of the angle of attack. Since the flow field around the wing is strongly influenced in ground effect, the size and nature of the wake will vary. Consequently, the wake blockage will also be a function of ground clearance.

In a closed test-section the wake blockage increases the drag. In an open test-section it decreases the drag, but is frequently considered negligible because the airstream is free to expand. A decrease in drag results because the tunnel airstream essentially expands more than it would in an infinite stream. Depending on the method used, the correction is applied to the drag and the dynamic pressure, or, just the dynamic pressure. Maskell's[22] method for wings and streamlined bodies, for both separated and unseparated flows, applies the correction to the dynamic pressure only. Therefore, this correction is also made before the forces and moments are reduced to coefficient form.

Maskell[22] determines the wake blockage correction term by provisionally reducing the lift and drag to coefficient form with the uncorrected dynamic pressure, q. Dividing the total drag coefficient into a constant part, C_{D0}, a part proportional to C_L^2, and a part due to separated flow, C_{DS} (figure 3.10), the total wake blockage correction term for a closed test-section is given by;

$$\epsilon_{wb.closed} = \frac{S}{4C}C_{D0} + \frac{5S}{4C}C_{DS} \tag{3.13}$$

Where;

- S = wing planform area
- $C_{DS} = C_D - C_{Di} - C_{D0}$

C_{Di} is the induced drag which arises from the wing-tip vortices formed by a finite, lift producing wing. C_{Di} is proportional to C_L^2. C_{D0} is the profile drag and defined as that component of the total drag due to viscous effects, consisting of skin friction and form drag. For angles of attack below the stall angle, the term C_{DS} is usually zero. For an open test-section, the correction is negative and smaller, and, the following relation is used.

$$\epsilon_{wb.open} = -0.25\epsilon_{wb.closed} \tag{3.14}$$

3.4.3 Application of Solid and Wake Blockage Correction Terms

The final blockage correction is given by:

$$\epsilon_{total} = \epsilon_{sb} + \epsilon_{wb} \tag{3.15}$$

The corrected tunnel velocity is given by:

$$V_c = V_u(1 + \epsilon_{total}) \tag{3.16}$$

The corrected dynamic pressure is given by:

$$q_c = q_u(1 + \epsilon_{total})^2 \tag{3.17}$$

Chapter 4

UCT McMillan Laboratory Wind Tunnel

4.1 Tunnel Parameters and Flow Conditions

The UCT McMillan Laboratory wind tunnel is a closed return wind tunnel. The test-section has an octagonal profile jet and can operate in an open or closed test-section configuration. Some of the key features of the tunnel are listed in table 4.1. The values indicated for the static pressure gradient and the turbulence intensity are for open test-section operation.

For the experiments described in this thesis, the tunnel operated in an open test-section configuration. This allowed easy access for model changes and positioning of the instrumentation.

Table 4.1: Tunnel Parameters and Flow Conditions

Height, H	0.580	m
Breadth, B	0.876	m
Length, L	1.600	m
Fillet Height	0.146	m
Section Area, C	0.453	m^2
Tunnel Aspect Ratio, B/H	1.51	-
Maximum Test Velocity	≈ 30	m/s
Static Pressure Gradient, dp/dl	≈ 0	Pa/m
Turbulence Intensity	0.4	%

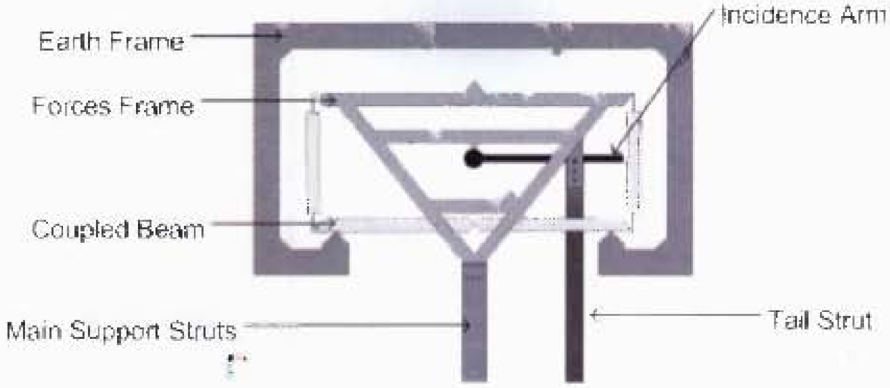

Figure 4.1: Schematic of TEM Balance

4.2 The Force Balance Specifications and Calibration

The force balance is a 1976 TEM Engineering model 528, 3-component, parallel motion type balance (figure 4.1). It can operate in an under or over-tunnel configuration. The model support system is mounted on a forces frame, which is suspended by a coupled beam assembly. The lift and drag forces act through the forces frame, which transfers the loads to two strain gauge transducers. The pitching moment acts, via a tail strut, on an incidence arm mounted on the forces frame. The incidence arm transfers the load to another transducer and is also used to set the angle of attack. The balance moment centre (the point about which the moment is measured) acts about the pivot point of the main model support struts. It is important that the main struts are perpendicular to the forces frame and that the tail strut remains parallel to the main struts. Furthermore, the incidence arm must remain parallel to the line between the pivots of the main and the tail struts, thus forming a parallelogram.

The balance calibration was checked using the supplied calibration equipment. This consisted of:

1. a calibration frame, which was attached to the model supports to simulate the model under test.
2. a pulley for the application of drag loads.
3. a set of accurate weights and two scale pans to support the individual weights.

A lift force was applied to the balance by the addition of weights to the calibration frame. Drag was applied via a horizontal wire attached to the rear of the calibration

Table 4.2: Balance Specifications and Calibration Constants

Component	Load Range	Accuracy	Calibration Constant
Lift	$0 - 90\ N$	$0.222\ N$	$111.489\ N/V$
Drag	$0 - 36\ N$	$0.0890\ N$	$39.555\ N/V$
Pitching Moment	$0 - 1.70\ N.m$	$0.0170\ N.m$	$2.2249\ N.m/V$

Incidence Range	$-10^\circ\ to\ +40^\circ$

frame and passing over the calibration pulley where the weights were hung. A pitching moment was applied by shifting the positions of the scale pans $50\,mm$ off the moment axis. Weights were applied and the calibration checked. The load range, transducer accuracy and recalculated calibration constants are given in table 4.2.

The lift/drag and lift/moment interaction was checked. Interaction in both cases was less than 0.1% and well within the transducer accuracy. Therefore, it was considered negligible. Oil dashpots were provided to dampen turbulence-induced oscillations in the mechanical linkages. Due to the high turbulence levels experienced at high angles of attack during pre-tests, the oil was replaced with $80W90$ weight oil to increase the damping.

4.3 Data Acquisition

The original display of the body forces was made using a digital volt-meter. However, the pre-tests indicated insufficient damping of the mechanical linkages due to highly separated flows at high angles of attack. This resulted in rapidly changing data values on the digital display, making accurate recording of the data difficult. It was decided to capture the signals over a period of time and calculate the statistical mean. The signals from the lift, drag and pitching moment transducers were sampled at $100\,Hz$ with a PCI-730 high performance data acquisition board. A virtual instrument panel was constructed in LabView to manage all data acquisition. The forces and moments were displayed in real-time to help identify any peculiarities during a test. Each signal was sampled for 30 seconds and processed to find the statistical mean (figure 4.2). The appropriate scale factors were then applied. The repeatability of the data was checked and found to be within the specified accuracy of the balance. The data was then saved to an Excel spreadsheet for post processing.

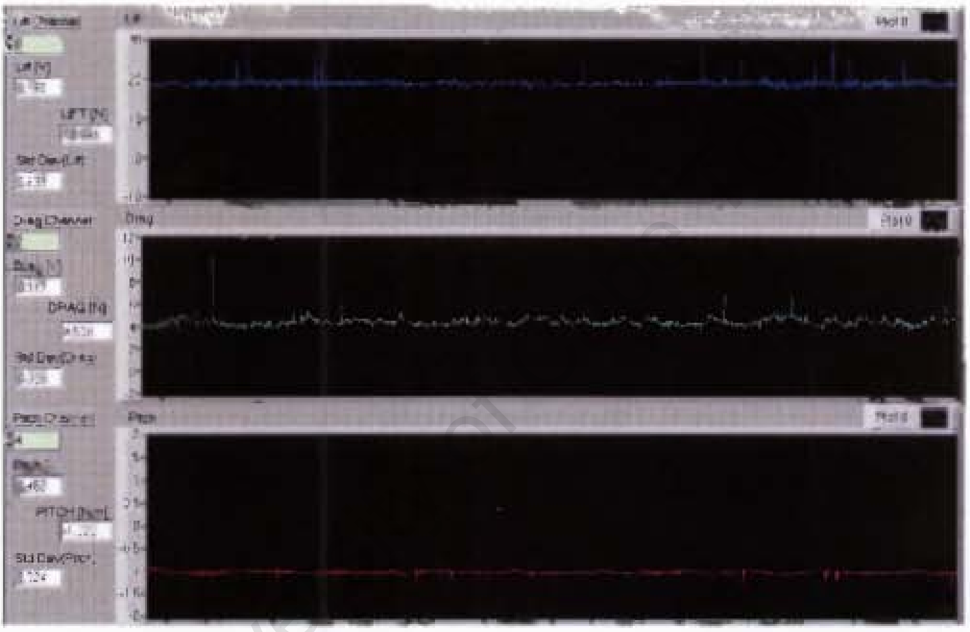

Figure 4.2: LabView Display Panel

Chapter 5

Experimental Apparatus Design Procedure

The principle design task was to develop a moving-belt ground plane for use in the UCT McMillan Laboratory wind tunnel. Furthermore, this involved the design of several additional features to allow positioning of the ground simulation system and the required instrumentation. A discussion of the design process of each element of the final design now follows.

The TEM 3-component balance was previously operated in the under-tunnel configuration. Therefore, the balance would have to be converted to the over-tunnel configuration and repositioned above the test-section for all subsequent tests. The next design decision depended on the method used for adjusting the ground clearance. For cost and complexity reasons, it was decided not to utilise any system using suction or blowing devices at this stage. This ruled out the possibility for changing the ground clearance through the vertical displacement of the moving-belt system. This method, like the 'raised floor: suction at leading edge' method, requires a fan or blower to remove the flow from the leading edge of the exposed belt and the re-injection of it at a downstream location. There was also insufficient room below the test-section to accommodate the moving-belt system and an elevation system by any simple means. An alternative method, such as that used by Turner[21], involved the use of a telescoping model support strut. This was a favoured method. However, the TEM balance consists of two leading edge struts and a tail support strut. Synchronisation of all three struts was thought to be too complicated, and led to the decision to fix the strut lengths and elevate the balance as a complete unit. Based on this design methodology, each component of the test apparatus is discussed below and the final configuration is shown in figure 5.6 and 5.7.

5.1 TEM Balance Elevator

5.1.1 Design Criteria and Concept

Listed below are several design criteria that were considered important.

- The balance-elevator system must maintain alignment under aerodynamic loading and changes in elevation.
- The change in elevation should exceed the half height of the tunnel. This will allow testing at the centreline and at the ground.
- The change in elevation should ideally occur in the vertical direction only, unlike a scissor jack which moves horizontally as it moves vertically.

Several designs were considered utilising various elevation-changing methods. However, the primary concern was whether or not the elevation system could maintain adequate alignment under the load of the aerodynamic forces and during an elevation change.

5.1.2 Final Assembly

The final design consisted of two frames (figure 5.1). An outer framework supported the four solid bar legs, while an inner framework was guided by the four legs. The design incorporated a $300\,mm$ elevation change. This was sufficient to move a wing from the tunnel centreline to the tunnel floor. It was concluded that a design incorporating four $30\,mm$ diameter, bright mild steel solid bar legs, with phosphor-bronze bearing shells, would give adequate support and alignment. The advantage of this system was that the balance would only move in the vertical direction. The design was also very simple and a single overhead jacking system could be used. The main disadvantage with the use of bearing shells was that perfect alignment of the four solid bar legs and bearings was required to prevent them from binding or pinching. A greater tolerance in the fit of the bearing shells could be used, however, this would lead to greater misalignment under aerodynamic loads. The design required that the entire frame be bolted together since heat induced in a welded frame would have caused the bearing shells to distort. The assembly drawing is included in Appendix C.

Figure 5.1: TEM Balance Elevator

5.2 Elevator Support Frame

5.2.1 Design Criteria and Concept

Once the design of the balance elevator was finalised, a supporting framework was needed to position the balance-elevator system appropriately. Several design criteria that were considered important are listed below.

- The framework would have to allow the balance to be shifted forward and backward. This will allow for different test locations in the stream-wise direction.
- The framework must position the balance outside of the shear layer of the test-section jet. This will prevent possible turbulence-induced oscillation in the supporting framework that may upset balance alignment or data quality.
- The framework must not be excessively far away from the test-section. Further away will require longer wing support struts which may bend under aerodynamic loading.
- The framework must allow complete access to the wind tunnel test-section for positioning of the moving-belt system and easy model configuration changes.

Figure 5.2: Elevator Support Frame

5.2.2 Final Assembly

The final design assembly is shown in figure 5.2 and consisted of a two-rail track that would allow the balance to be shifted. No diagonal members were used as they would obstruct either the airstream or access to the test-section. Thus, adequate structural rigidity of the supporting framework was achieved from high-weight channel and I-beam sections. The framework was bolted to existing points on the tunnel structure.

5.3 Moving-Belt Ground System

5.3.1 Design Criteria and Concept

Once the dimensions of the elevator support frame had been proposed, the design of the moving-belt ground system could begin. The following design criteria were considered essential to the design.

- Easy installation and removal from the tunnel.
- Maximum belt speed should equal maximum tunnel jet velocity ($\approx 30\,m/s$).

Based on these criteria, the design of the rolling cylinders, the support structure and belt are discussed below.

5.3.2 Rolling Cylinders

The rolling cylinders were central to the design of the moving-belt ground plane. For a given belt speed, increasing the diameter of the rolling cylinders would lower the rotational rate of the rolling cylinders. A lower rotational rate would make dynamic balancing of the cylinders easier. This aspect of the design was observed in the moving-belt ground systems used by Turner[21], and, Kim and Geropp[20]. Turner used a 190 mm diameter cylinder. Kim and Geropp used a 350 mm diameter cylinder. Due to workshop machine constraints, 300 mm was the largest diameter section that could be machined. A 275 mm diameter pipe of suitable length and wall thickness was obtained. No bevel or surface profiling was made across the cylinders; however, the surface of the cylinders was knurled to improve belt-cylinder contact. End-plates and axles were machined from several solid billet steel components; press-fitted, welded and then re-machined for perfect alignment. These were then press-fitted and bolted into the rolling cylinders. The axle diameters were matched to a set of 35 mm self-aligning bearings. Dynamic balancing was performed at approximately 1500 rpm.

5.3.3 Supporting Structure

The mass of the two cylinders was approximately 140 kg. Due to the large mass of the cylinders, a large flat platform was constructed from 155 mm and 180 mm I-beam. This formed the base of the moving-belt ground system. Bolted to this were two sets of cross-members which supported a set of pillars. The pillars supported the cylinders and could be shifted forward and backward to allow tracking control of the belt. The clearance between the belt and the supporting frame was set at approximately 100 mm. A Formica guide plate was aligned beneath the belt to ensure it maintained level movement. A separate frame, which also provided mounting points for the belt-tracking screws, supported the guide plate.

5.3.4 Belt Design

The conveyor transmission company, NTI, recommended a PVC two-ply reinforced belt. The dimensions of the belt were 2920 mm long by 890 mm wide. The belt was hot-welded to ensure smooth running over the cylinders at high speed. The recommended belt tension was $3 - 5\,N/mm$ of belt width.

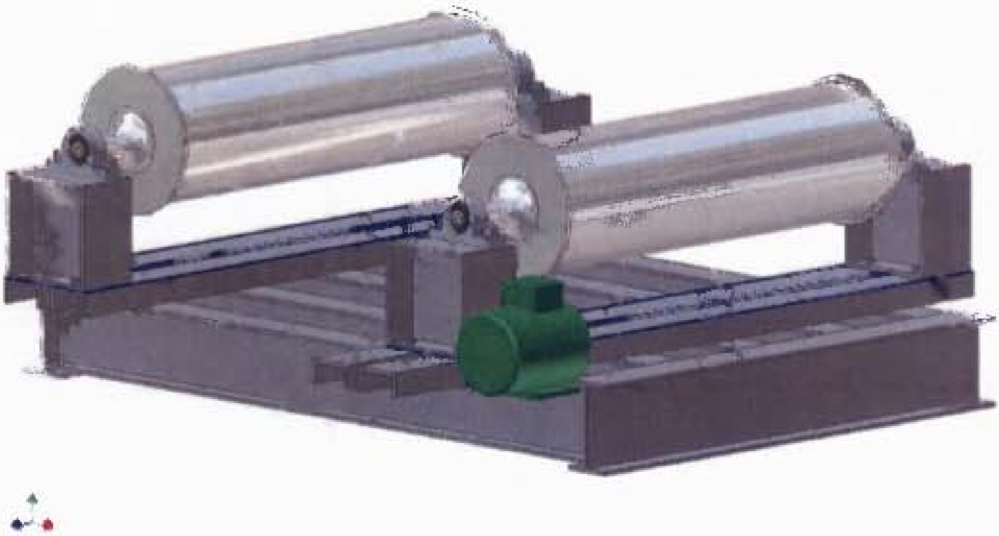

Figure 5.3: Moving-Belt Ground System

5.3.5 Final Assembly

The final assembly of the moving-belt ground plane is shown in figure 5.3 and consists of three main components; a lower platform that formed the base of the structure, a pair of supporting pillars for the cylinders, and a pair of cylinders. The total mass of the system was approximately 400 kg. The cylinders were driven by a 3-phase induction motor. Speed control was made with a single to 3-phase frequency converter. The belt reached a controller-restricted top speed of 22 m/s, but could reach speeds closer to 30 m/s if unrestricted. Belt speed was evaluated with an optical tachometer. The belt spanned 890 mm, beyond the full width of the tunnel, and 1060 mm (66%) across the length of the tunnel. The belt was aligned at 15 mm above the tunnel floor and a boundary layer splitter plate positioned at the leading edge of the belt. The assembly drawing is included in Appendix C.

5.4 Wing Support System

5.4.1 Design Criteria

Once the design of the moving-belt system, the balance elevation system and supporting structure was finalised, the design of the wing support system was addressed. This support system needed to be sufficiently rigid to prevent bending under aerodynamic loading. However, a small cross-section was preferred to reduce tare and interference effects in the data. A tapered strut would be ideal; therefore, it was decided to manufacture composite struts, where any taper requirements could be addressed. The final assembly of the wing support system is shown in figure 5.4 and the assembly drawing is included in Appendix C.

5.4.2 Main and Tail Struts

An un-tapered steel compression mould was used to manufacture the struts. The profile of the struts was laser cut into 5 mm sheet steel and supported on either side by 10 mm backing plates. The three pieces were bolted together to form a compression mould. Each 5 mm thick strut was approximately 1300 mm long and manufactured from unidirectional solid carbon. Three solid carbon sections symmetrically staggered and laminated would form the final part, 15 mm wide at the base. A steel insert was bonded at the end where the wing would attach, and, mounting holes were drilled at appropriate locations using the CNC machine.

5.4.3 Strut Windshields

Primarily because of the highly turbulent shear-layer associated with all open test-sections, each strut was shrouded from the shear-layer by a windshield. The windshield formed a narrow pyramidal structure that surrounded the strut. The epoxy-fibreglass windshields were made from a two-part mould that was formed from a clay mock-up of the windshield. The sulphur-free hard styling clay called Y2-Clay, which is widely used by the automotive and aeronautical industries, was used for the mock-up[23]. The clay is a hard, dry substance that can be machined at room temperature. At 60°C the clay becomes soft and is easily worked.

5.4.4 Strut Mounting Brackets

The two main struts were each mounted on a steel support bracket which was designed to fit the existing balance components. The tail strut was mounted on the incidence arm, which formed part of the pitching moment measurement system. A high degree of accuracy was required in machining these parts to ensure the main struts remained perpendicular to the forces frame and that no play existed in the pivot of the tail strut mounting bracket.

Figure 5.4: Wing Support System

5.4.5 Wing Mounting-spar

A mounting-spar was used to correctly align the wing on the wing support system. This component also required a high degree of precision in its manufacture. The pivot points needed coplanar alignment to ensure the strut, incidence arm and mounting-spar formed a perfect parallelogram as required for accurate pitching moment measurement. The spar was aligned in the plane of the chord of the wing during its construction, with the main pivot points located at the leading edge of the wing and the tail strut pivot at the trailing edge.

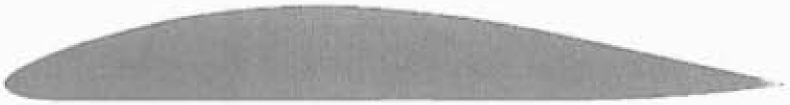

Figure 5.5: $DHMTU\ 10-40-2-10-2-60-21-5$ Wing

5.5 Wing Profile

5.5.1 Design Concept

The tunnel breadth limited the span of the wing. Barlow et al.[6] indicated that a maximum wing span to tunnel breadth ratio of 0.8 was advisable for 3-dimensional wings. The tunnel breadth at ground level was $584mm$. Based on this guideline, a span of $465mm$ was used. A wing of aspect ratio, $AR = 3$, was chosen. This gave a chord length of $c = 155mm$. A $DHMTU\ 10-40-2-10-2-60-21-5$ wing profile was arbitrarily chosen for these experiments and is shown in figure 5.5. This wing was relatively slender with a 10% maximum thickness at 40% chord. The wing had a flat section on the lower surface from 10% to 60% chord and a nose radius parameter of 5. The coordinates for the wing were calculated using a profile generator[5]. A description of the $DHMTU$ parameters and the drawings of this wing are included in Appendix B.

5.5.2 Construction Technique

The wing was constructed in a two-part injection mould. Divided by the chord-line, the mould was separated into a top and bottom half. Several profiles of each half were cut on an automatic CNC machine. These were used to shape each half using Y2-Clay[23]. An epoxy mould of the upper and lower half of the wing was made. These were bolted together to form the final injection mould. Two guide slots in the leading edge, and one in the trailing edge, were machined on the chord-line of the mould where the pivot points of the wing mounting-spar were located. The construction of the wing was made by first laying up an epoxy-fibreglass skin on each half of the mould. The wing mounting-spar was aligned in the guide slots and the mould bolted together. A polyurethane liquid-compound was injected into the mould and allowed to cure. The compound expanded into the enclosed volume to form a rigid closed cell foam with a density of approximately $80\,kg/m^3$. The wing was de-moulded, primed and wet sanded to form the final part.

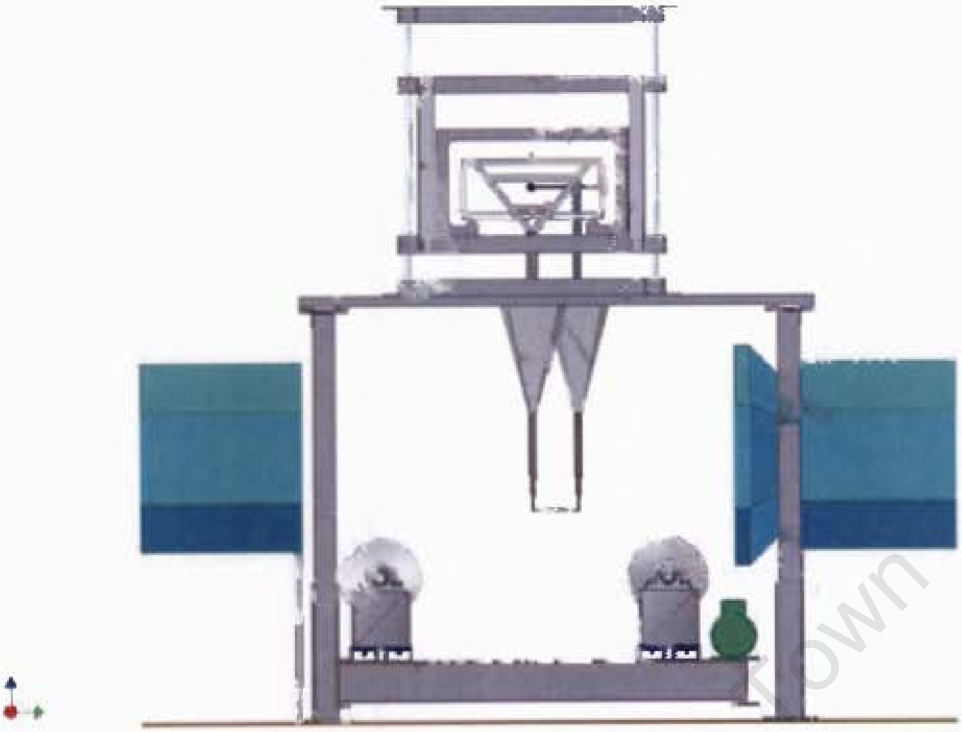

(a)

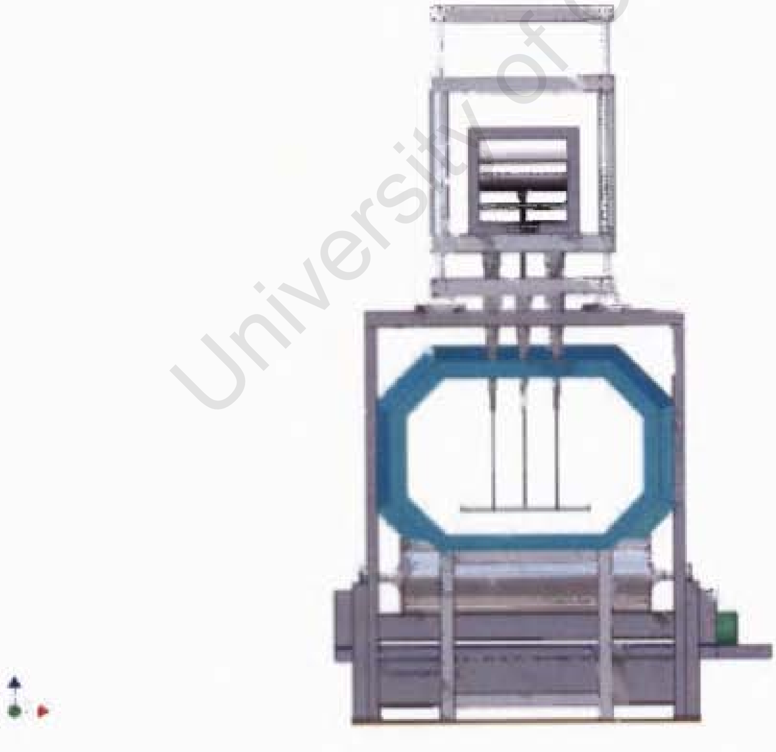

(b)

Figure 5.6: Final Configuration of Test Apparatus

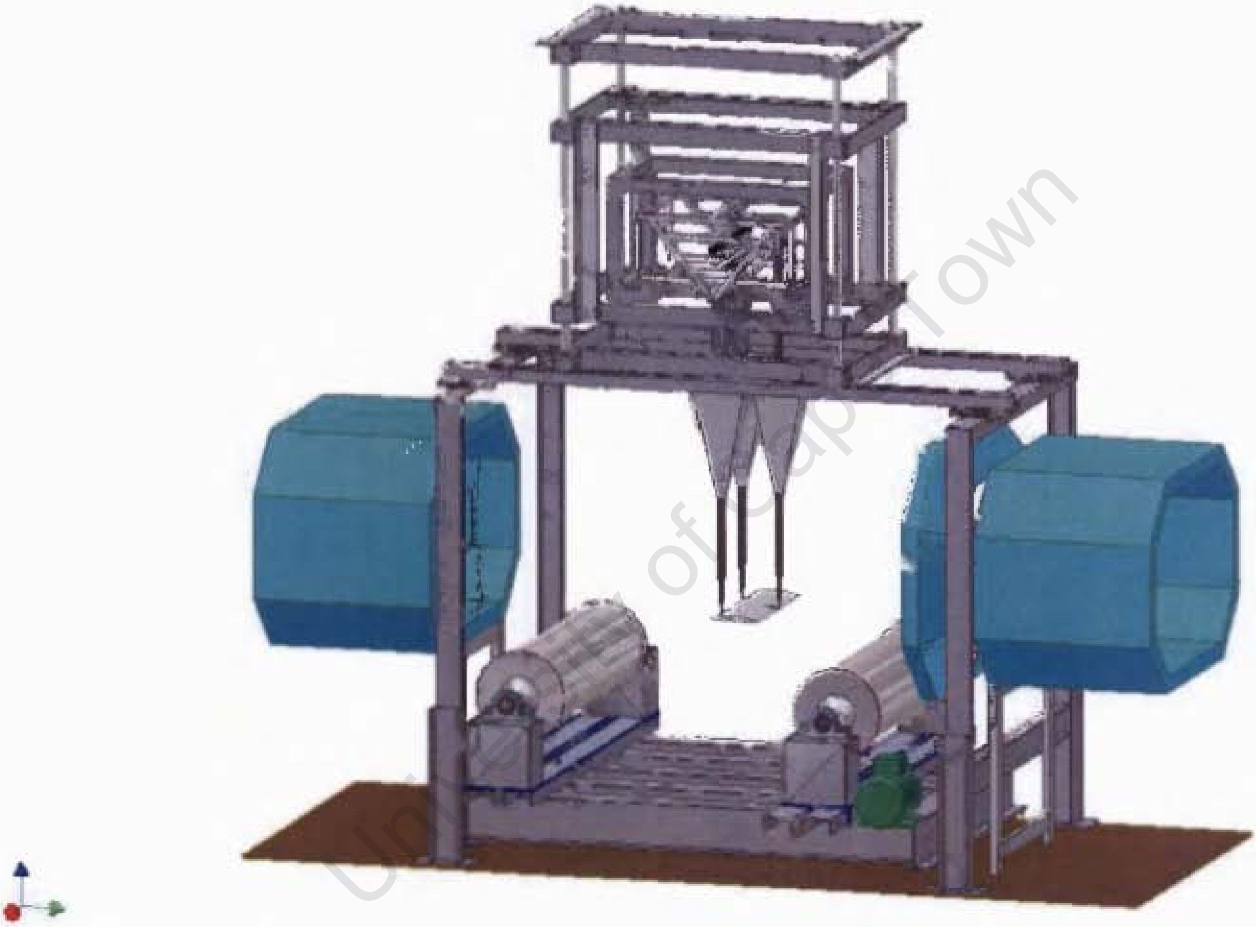

Figure 5.7: Final Configuration of Test Apparatus

Chapter 6

Test Methodology

6.1 Introduction

The procedure used to gather the required information and data necessary for correct analysis of all subsequent test data is presented in this chapter. The techniques, the formulae used, and, the assumptions made were identified and discussed. The pre-test procedure begins with the calibration of the test-section and balance, followed by a sequence of data correction procedures. The test procedure follows with a discussion of the details of how the force and moment data was captured as a function of angle of attack and ground clearance. The post-test procedure discusses the application of corrections and the final form of the data.

6.2 Pre-Test Procedure

The test-section airstream was considered to be adequately defined for the purposes of these experiments in terms of the distribution of the temperature, static pressure, dynamic pressure, and turbulence level (section 4.1). However, the test-section airstream ideally required a re-evaluation following the installation of the ground simulation device. The attitude of the balance, the moving-belt, the wing support system, and the wing, also required an evaluation to ensure proper alignment with the mean flow. This was achieved by aligning the various components relative to the tunnel floor and then correcting for any flow angularities and balance misalignment in the data reduction process.

6.2.1 Test-section and Mechanical Balance Calibration

The moving-belt ground plane was installed with the belt raised 15 mm above the tunnel floor. A boundary layer splitter-plate was co-aligned 15 mm above the tunnel floor at the leading edge of the belt. This removed the incoming tunnel floor boundary layer prior to it intersecting the belt. The centreline of the belt was then aligned with tuft threads, at the tunnel test velocity, to ensure that the belt was aligned with the mean airflow. The balance was levelled in the longitudinal and transverse directions. This was achieved through the forces frame upon which the main support struts were mounted. The main struts of the wing support system were installed and aligned perpendicular to the forces frame. The wing and tail strut were then installed, and the transducer readings set to zero by offsetting the mass of the wing and wing support system with the counterbalance weights. The incidence arm and wing were then levelled, while simultaneously checking that the tail strut remained parallel to the main struts. All struts, beams and surfaces were aligned using a digital inclinometer to an accuracy of 0.1°. The trunnion points (strut/wing pivots) were then checked for a firm, but frictionless rotation, to minimise hysteresis or poor repeatability in the moment readings. Finally, the main and tail strut windshields were installed. They were aligned to penetrate the shear layer and approximately 25% of the tunnel height/airstream. A typical experiment involving the moving-belt ground plane is illustrated in figure 6.1.

It was noted that with the wing/incidence arm in the level position, the indicated angle of attack was at the -1° position. Since the balance had been properly levelled, this suggested the error lay in the alignment of the angle of attack gauge. It was decided to continue to record all angles of attack as indicated by the gauge, and correct the error in the data reduction process.

6.2.2 Weight Tare Correction

A weight tare correction was required as a result of the model centre-of-gravity, CG, not existing at the balance moment centre. The moment generated was usually counteracted, at $\alpha = 0$, by the moment counterbalance weight. However, the moment due to the counterbalance weight remains constant with angle of attack, while the model moment changes with angle of attack (see figure 6.2). This error was accounted for in the data reduction process as follows. With the wind off, the pitching moment was recorded over the range of angles to be measured. The data was zeroed relative to an angle of attack of zero and applied to the raw moment data as it was captured. The procedure was repeated for each change in the model configuration which affected the location and magnitude of the CG. The weight tare correction

Figure 6.1: Typical ground experiment in the UCT McMillan Laboratory wind tunnel

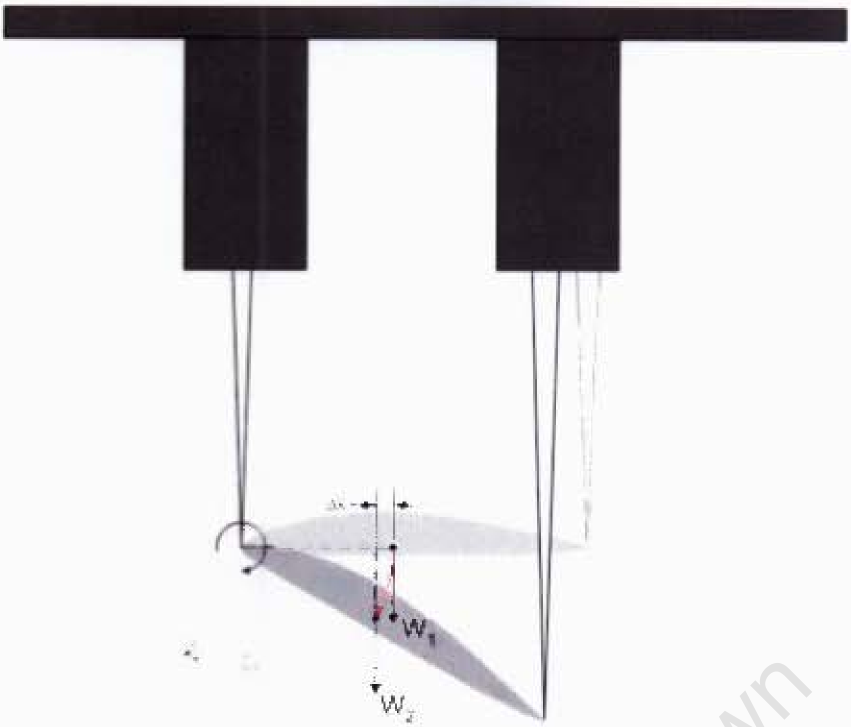

Figure 6.2: Change of model-weight moment with α

(M_{wt}) for each model configuration was applied to the appropriate moment data as follows (see figure A.1 on page 85):

$$M_{corrected} = M_{uncorrected} + M_{wt}$$

The weight tare correction tables, for each model configuration, are included in Appendix E.

6.2.3 Aerodynamic Balance Alignment

The aerodynamic balance alignment was determined by testing the wing with the full image support system in both the normal and inverted configuration (figure 6.3). The wing was pitched from -10 to $36°$ from a position on the tunnel centreline. The lift, drag and pitching moments were recorded.

The total angle correction made to the indicated angle was found from a plot of the normal and inverted C_L vs. α curves (figure 6.4). The angular variation between the curves indicated twice the error in the recorded angle of attack. The angle correction, $\alpha_{up,total}$, was calculated by averaging the error over the region of

Figure 6.3: DHMTU wing with full image support system

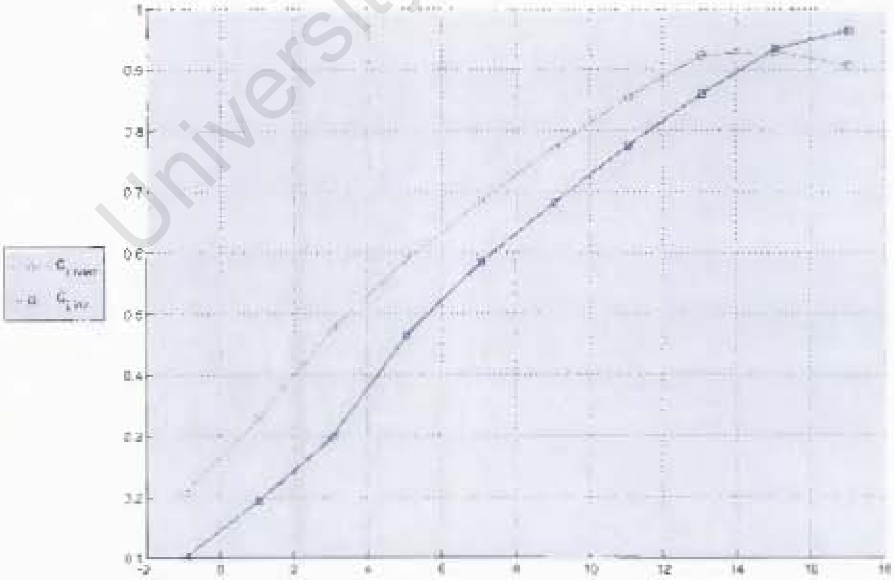

Figure 6.4: Normal and inverted C_L vs. α curves

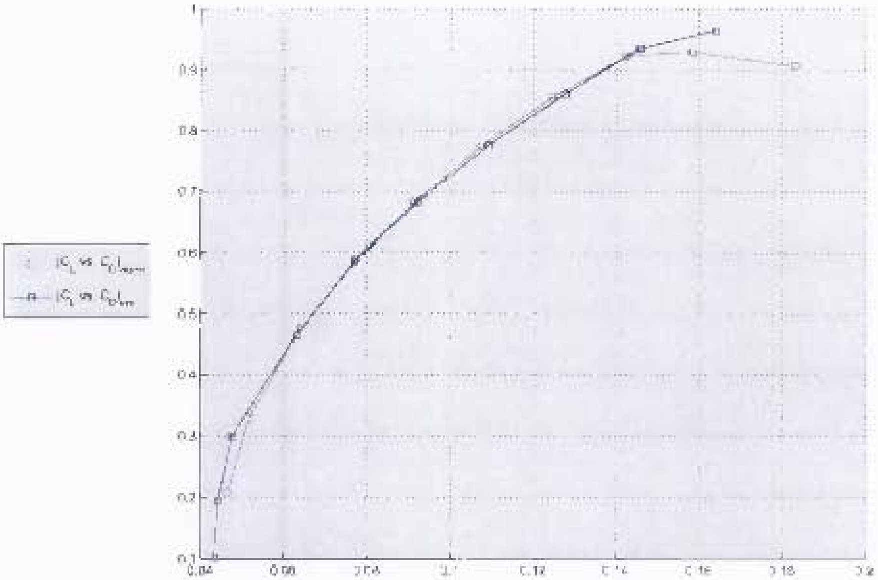

Figure 6.5: Normal and inverted polar curves

the lift curve that was approximately linear. This corresponded to $0.2 < C_L < 0.9$. The Matlab program that calculated $\alpha_{up,total}$ is included in Appendix D.

The aerodynamic balance alignment was checked by considering a plot of the normal and inverted C_L *vs.* C_D curves (figure 6.5). A slight rotation of the curves suggested that the lift was not perpendicular and the drag not parallel to the local airflow, however, the rotation appeared essentially zero. Nevertheless, the error in the angle of attack to the local airflow was estimated by averaging the local upflow angle, α_{up}, over a range of C_L values. By writing equation 3.2 in the form;

$$0.5\Delta C_D = (\tan \alpha_{up}) C_L \tag{6.1}$$

the calculated values of $0.5\Delta C_D$ *vs.* C_L were plotted in figure A.2 on page 86. The gradient of the curve gave the value of $\tan \alpha_{up}$. The Matlab program that calculated α_{up} is included in Appendix D and the results are discussed in the following chapter.

6.2.4 Tare and Interference Analysis

The support tare and interference (*T&I*) was evaluated by determining its influence at two ground clearances. Its magnitude and the change in magnitude were then evaluated.

The lift, drag and pitching moment data for the inverted wing with the full image support system had already been captured for the flow angularity analysis. The data

Figure 6.6: DHMTU wing in normal configuration

for the wing normal and inverted was then captured (see figure 6.6 and 6.7). All tests were conducted with the wing located at the tunnel centreline and the ground plane installed. A second test of the three configurations was conducted at a ground clearance of $h = 220mm$ ($h_0 = 1.4$) relative to the leading edge of the wing. In all tests, the belt was stationary to allow positioning of the image support system. However, in accordance with Turner[21] (section 2.4.7 on page 18), a stationary belt was not considered to be a problem, since $C_L \ll 10h_0$.

The tail support strut posed a problem for the test involving the image tail support. A windshield sheltered part of the tail strut from the airstream. As the angle of attack was changed, the length of the image strut needed to change to maintain an equal length of exposed strut. A compensation method proposed by Barlow et al[6] was used in the tests. This involved setting the length of the image tail strut equal to the minimum length of the exposed tail strut (see figure 6.8). For each angle of attack, the drag and moment generated by the missing image tail section was estimated and applied to the data.

The additional tail support drag was evaluated by plotting the drag against the exposed length of the main struts (since all struts were identical). Since drag is

Figure 6.7: DHMTU wing in inverted configuration

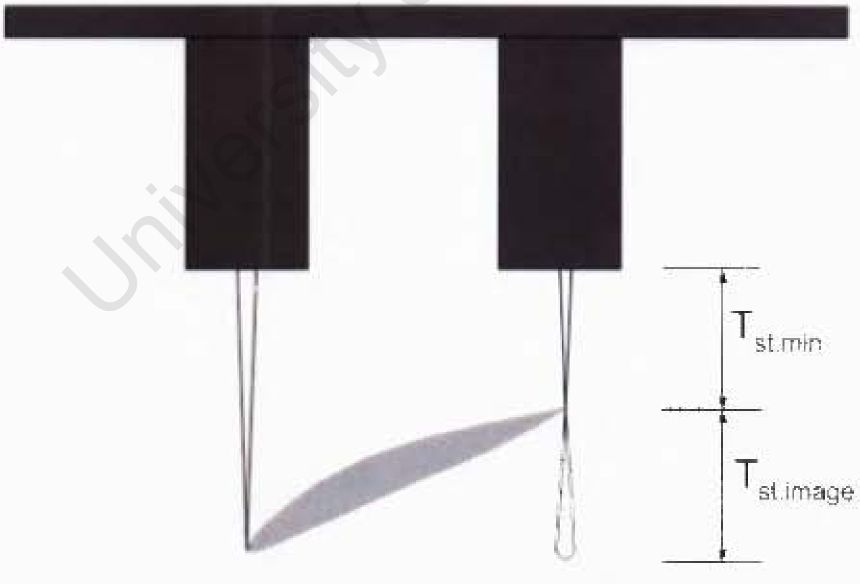

Figure 6.8. Length of image tail strut

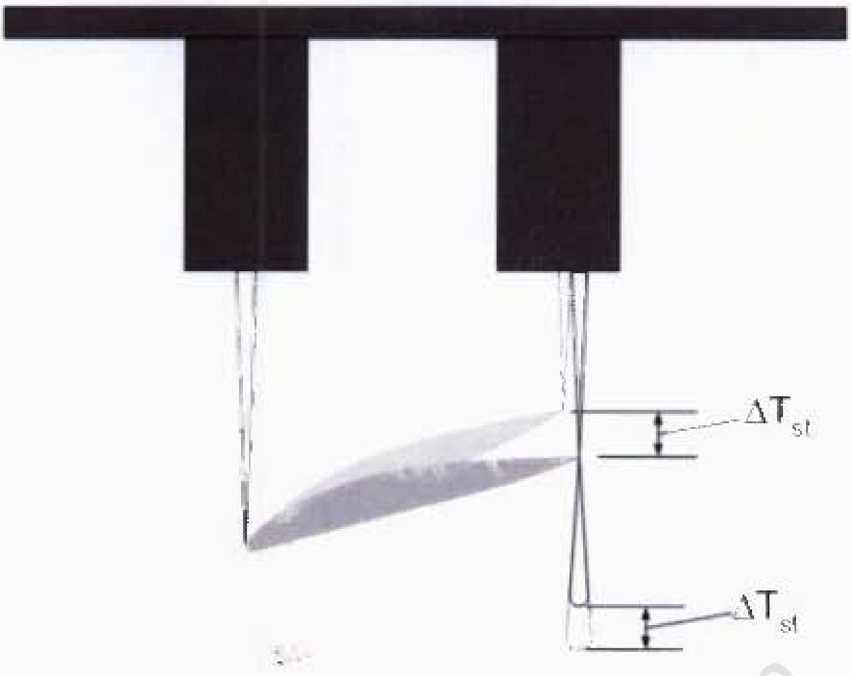

Figure 6.9: Additional length added to image tail strut

proportional to area, a linear curve was expected. The length of the missing section on the image strut was calculated as a function of angle of attack (see figure 6.9). The additional drag component was then calculated as a function of α. The moment generated by the additional drag component was estimated by applying the force at the centre of the absent section (see figure 6.10). This moment was calculated for each value of α. All image tail strut compensation was applied to the data from the inverted test with the full image support system. The additional tail support drag and moment tables are included in Appendix E.

Before the $T\&I$ correction terms for each angle of attack could be solved for, the data from all three tests was first corrected for the variation in weight tare. Once accounted for, the correction terms were determined by subtracting the wing inverted data from the wing inverted with full image support system. This was given by:

$$\begin{aligned}
L_{inv+image} - L_{inv} &= [L_{inv} + [T\&I]_{up,L} + [T\&I]_{low,L}] - [L_{inv} + [T\&I]_{low,L}] \\
&= [T\&I]_{up,L} \\
D_{inv+image} - D_{inv} &= [D_{inv} + [T\&I]_{up,D} + [T\&I]_{low,D}] - [D_{inv} + [T\&I]_{low,D}] \\
&= [T\&I]_{up,D} \\
M_{inv+image} - M_{inv} &= [M_{inv} + [T\&I]_{up,M} + [T\&I]_{low,M}] - [M_{inv} + [T\&I]_{low,M}] \\
&= [T\&I]_{up,M}
\end{aligned}$$

The correction terms are included in Appendix E, which includes the correction terms calculated at the tunnel centreline, at a ground clearance of $h = 220\,mm$

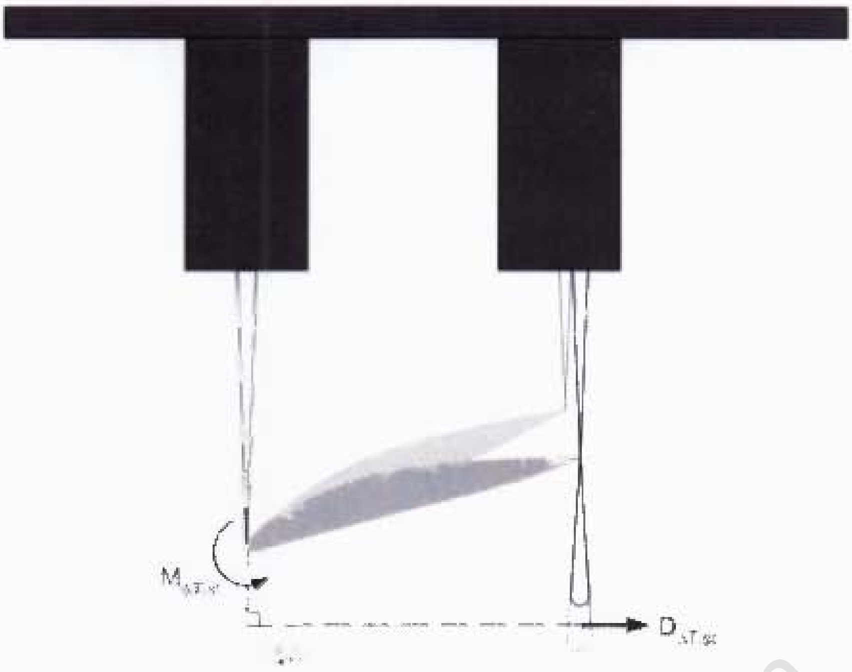

Figure 6.10: Drag and moment from additional tail strut length

($h_0 = 1.4$) and the mean values of the two. The results of the *T&I* analysis are discussed in the following chapter.

6.3 Test Procedure

6.3.1 Preparation

Once the *T&I* and weight tare tests were completed, the wing was positioned in the normal configuration. The transducers readings were zeroed and repeatability checked once again. For each component of lift, drag and pitching moment, a 2-D matrix was constructed in Excel. The horizontal axis (columns) represented the angle of attack and the vertical axis (rows) represented the ground clearance. The angle of attack was varied from -10 to $36°$, in $2°$ increments. Thus, 24 separate angles were tested. The ground clearance was varied from $290\,mm$ ($h_0 = 1.80$) down to $10\,mm$ ($h_0 = 0.06$). The increments in ground clearance varied, but below $161\,mm$ ($h_0 = 1$) the ground clearance was changed in $10\,mm$ increments. Tests were carried out at a total of 20 separate ground clearances. Thus, each 20×24 matrix consisted of 480 unique test configurations based on angle of attack and ground clearance.

Table 6.1: Test Conditions

Inclined Manometer Reading	120.0	mm
Dynamic Pressure, q	242.4	Pa
Velocity	20.1	m/s
Velocity	72.5	km/h
Mach Number	0.06	-
Effective Reynolds Number, Re_{eff}	2.21×10^5	-
Cylinder Rotational Rate, N	1373	rpm

6.3.2 Testing

The ground clearance was measured vertically from the trailing edge of the wing to the surface of the belt (figure 2.1 on page 7). For each angle of attack, a marker on the balance elevator system indicated the ground clearance on a scale rule. The angle of attack was set and the data captured at each specified ground clearance. When all ground clearances had been tested, the angle of attack was changed and the procedure repeated. The uncorrected data for the lift, drag and pitching moment is included in Appendix E. However, sixty one combinations of ground clearance and angle of attack were impossible to test at due to physical limitations of the wing support system and balance elevator system. These included; negative angles of attack at very low ground clearances, high angles of attack at very low ground clearances, and, medium to high angles of attack at high ground clearances.

For all test runs, the velocity of the airstream was maintained at $20\,m/s$. This corresponded to a dynamic pressure, $q = 242\,Pa$, which was measured using an inclined manometer and a pitot-static tube. From the airstream velocity, the required rotational speed of the rolling cylinders was calculated. This matched the belt velocity to the airstream velocity. Table 6.1 indicates these and several other variables relating to the test conditions.

6.4 Post-Test Procedure

6.4.1 Initial Corrections

The data was then corrected as previously specified. An overview of these corrections details the following adjustments to the recorded lift, drag and pitching moment;

1. Lift
    (a) T&I correction

    (b) Correction to angle of attack

2. Drag
    (a) T&I correction
    (b) Drag increment due to aerodynamic balance misalignment
    (c) Correction to angle of attack
3. Pitching Moment
    (a) T&I correction
    (b) Weight tare correction

The individual corrections and the corrected data are included in Appendix E.

6.4.2 Final Corrections

The final correction was made to the dynamic pressure, q. This was achieved through the solid and wake blockage correction terms. Blockage normally applies to everything in the test-section. This includes the wing support system, the windshields or any other items required in the test-section during the test. However, since the image method was used to evaluate the $T\&I$, the blockage due to the wing support system and windshields was accounted for. The solid and wake blockage was accounted for as follows.

Solid Blockage

The solid blockage correction factor was constant with angle of attack and ground clearance. The solid blockage was calculated using figure 3.8 on page 28 and figure 3.9 on page 29. The required parameters are listed below.

Table 6.2: Solid Blockage Calculation Parameters

Wing Thickness Ratio, t/c	0.143	-
Span-to-Tunnel Breadth Ratio, b/B	0.53	-
Tunnel Aspect Ratio, B/H	1.55	-
Estimated Wing Volume, Vol_{wing}	0.0012	m^3
Test-Section Area, C	0.453	m^2

The wing volume was estimated using equation 3.12. From figure 3.8, the body shape factor, K_1, was estimated using the curve of the 4-digit $NACA$ profile. The tunnel-model shape factor, τ_1, was estimated from figure 3.9. Both values are listed below.

Table 6.3: Estimated Values of K_1 and τ_1

Body Shape Factor, K_1	1.03	-
Tunnel Shape Factor, τ_1	0.875	-

The open test-section solid blockage was given by:

$$\begin{aligned} \epsilon_{sb.open} &= \frac{-0.25 K_1 \tau_1 Vol_{wing}}{C^{1.5}} \\ &= -0.00089 \end{aligned} \tag{6.2}$$

Wake Blockage

The wake blockage correction factor varied with angle of attack and ground clearance. The wake blockage terms, C_{D0} and C_{DS}, were determined using the following method. For angles of attack below the stall angle, the total drag coefficient was divided into parasite and induced parts;

$$\begin{aligned} C_D &= C_{D.Pe} + \frac{C_L^2}{\pi.e.AR} \\ &= C_{D.Pe} + K.C_L^2 \\ &= C_{D.Pe} + C_{Di} \end{aligned} \tag{6.3}$$

Where;

- $C_{D.Pe}$ – equivalent parasite drag coefficient
- $K = 1/\pi.e.AR$
- e – span efficiency factor
- AR – aspect ratio

Parasite drag ($C_{D.P}$) is assumed constant with angle of attack; and includes skin friction drag, pressure drag and drag due to interference, excrescences and roughness. For a wing, C_{D0} is essentially the same as the $C_{D.P}$. The product of the span efficiency factor and the aspect ratio, $e.AR$, represents the effective aspect ratio of an equivalent wing having an elliptical lift distribution. The value of e is usually close to, but less than, one. The value of e usually decreases with decreasing AR, but in ground effect e can increase to values greater than one.

A value for K and $C_{D.Pe}$ were required for each value of h_0. The value of K and $C_{D.Pe}$ were determined from a plot of C_D *vs.* C_L^2 from the data at each ground clearance[6]. For $0.2 < C_L < 0.9$, each curve was approximated as linear. The gradient of the linear curve was set equal to K. Finding K meant e could be calculated as well. $C_{D.Pe}$, an approximation to the true parasite drag, $C_{D.P}$, was given by the intercept of the linear curve with the C_D axis. For each value of h_0, C_{D0} was set equal to $C_{D.Pe}$. C_{DS} was then calculated over the full range of h_0 and α values, given by;

$$\begin{aligned} C_{DS} &= C_D - C_{Di} - C_{D0} \\ &= C_D - K.C_L^2 - C_{D.Pe} \end{aligned}$$

In calculating C_{DS}, if the value became negative, the flow was considered unseparated, and the value of C_{DS} set to zero. The values of e, the wake blockage correction factor and the final corrected dynamic pressure are included in Appendix E and discussed in the following chapter. No further corrections were required. All that remained was to transfer the moment data to a desired centre-of-gravity location and reduce the force and moment data to coefficient form with the corrected dynamic pressure data.

6.4.3 Moment Transfer

The pitching moment was measured about the trunnion of the main support struts. This represented the balance moment centre. However, the moment is usually transferred to a desired centre-of-gravity location on the model, usually the 1/4MAC. With reference to figure 6.11, this was achieved as follows:

$$\begin{aligned} \varepsilon &= \arctan\left(\frac{Y}{X}\right) \\ R &= \sqrt{Y^2 + X^2} \\ \varphi &= \varepsilon + \alpha \\ M_{1/4MAC} &= M_{tr} + L.R.\cos\varphi + D.R\sin\varphi \end{aligned}$$

M_{tr} represents the moment measured about the balance moment centre (the trunnion). The values of X and Y were known from the model (wing) making process. Thus, φ, and hence $M_{1/4MAC}$, was calculated as a function of α. The process was repeated for each data set corresponding to a different value of h_0. It was important that all corrections, weight tares etc, were applied before the moments were trans-

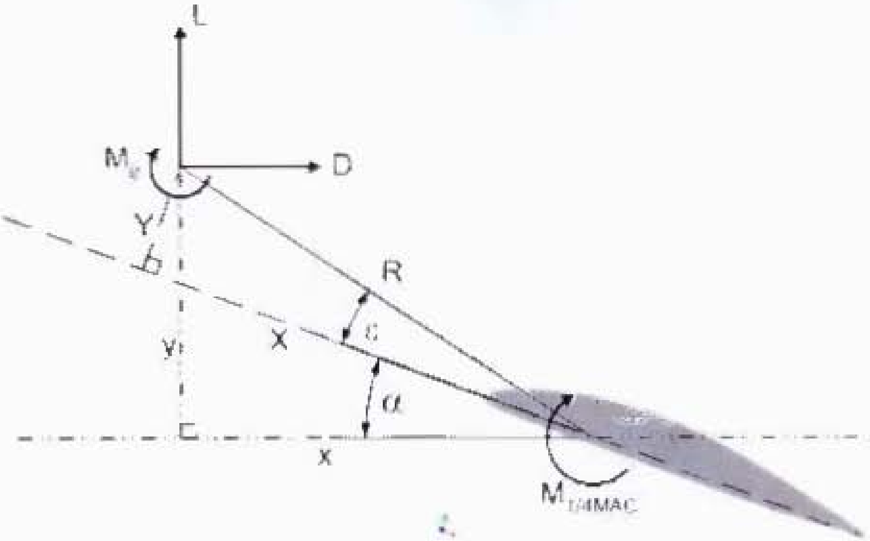

Figure 6.11: Moment Transfer Diagram

ferred. The force and moment data was then reduced to coefficient form and are included in Appendix E.

6.4.4 Resolution of the Aerodynamic Centre in Pitch

The resolution of the position of the aerodynamic centre in pitch (ACP), for constant values of h_0, was evaluated next. The C_M *vs.* C_L data was plotted as a function of α. The C_M data was given relative to the 1/4MAC. Body-fixed axes were defined relative to this point, and were aligned forward, starboard, and down (see figure 2.8). From equation 2.8, the ACP was defined by;

$$\begin{aligned} X_\alpha &= \frac{C_{M\alpha}}{C_{L\alpha}} \\ &= \frac{\left(\frac{\partial C_M}{\partial \alpha}\right)}{\left(\frac{\partial C_L}{\partial \alpha}\right)} \\ &= \left(\frac{\partial C_M}{\partial C_L}\right)_{\alpha} \end{aligned}$$

Therefore, the slope of the C_M *vs.* C_L data gave the distance to the ACP, X_α, as a function of α. However, it was decided to track the ACP as the wing entered ground effect, by resolving the forces and moments as given by equation 2.11, re-written here for convenience.

$$\begin{aligned}\frac{\partial C_{M.ac.\alpha}}{\partial C_L} &= 0 = \frac{\partial C_{M.Ref}}{\partial C_L} \\ &\quad -\frac{x}{c}\left[\left(1 + C_D\frac{\partial \alpha}{\partial C_L}\right)\cos\alpha + \left(\frac{\partial C_D}{\partial C_L} - C_L\frac{\partial \alpha}{\partial C_L}\right)\sin\alpha\right] \\ &\quad -\frac{z}{c}\left[\left(C_L\frac{\partial \alpha}{\partial C_L} - \frac{\partial C_D}{\partial C_L}\right)\cos\alpha + \left(1 + C_D\frac{\partial \alpha}{\partial C_L}\right)\sin\alpha\right]\end{aligned}$$

Solving this equation would allow the movement of the ACP along the chordline and above/below the chordline to be tracked as the wing entered ground effect. The data was used to find C_L, C_D and α, and, linearised over the region $0.45 < C_L < 0.9$ to find the slopes of $\partial C_M/\partial C_L$ and $\partial\alpha/\partial C_L$. The data was linearised over this region since it corresponded to $3 < \alpha < 11$, which were the expected cruise angles for normal flight. Since the value of the span efficiency factor, e, had already been calculated, the value of $\partial C_D/\partial C_L$ was found from the derivative of equation 6.3;

$$\begin{aligned}C_D &= C_{D0} + \frac{C_L^2}{\pi.e.AR} \\ \therefore \frac{\partial C_D}{\partial C_L} &= \left(\frac{2}{\pi.e.AR}\right)C_L\end{aligned}$$

The substitution of the data, from two points/angles in the linearised region, allowed the simultaneous solution of equation 2.11. The program that performs each of these tasks was included in Appendix D and the results are discussed in the following chapter.

6.4.5 Resolution of the Aerodynamic Centre in Height

The resolution of the position of the aerodynamic centre in height (ACH), for constant values of α, was evaluated as follows. The C_M *vs.* C_L data was plotted as a function of h_0. Once again, the C_M data was given relative to the 1/4MAC. Body-fixed axes were defined relative to this point, and were aligned forward, starboard, and down. The calculation of the ACH was made utilising equation 2.12, namely;

$$\begin{aligned}X_h &= \frac{C_{Mh}}{C_{Lh}} \\ &= \frac{\left(\frac{\partial C_M}{\partial h_0}\right)}{\left(\frac{\partial C_L}{\partial h_0}\right)} \\ &= \left[\left(\frac{\partial C_M}{\partial C_L}\right)\right]_{h_0}\end{aligned}$$

Therefore, the slope of the curves gave the distance, in percentage chord, to the location of the ACH, as a function of h_0 (α – constant). However, the resolution of the ACH by equation 2.12 was limited in that it only defined the movement of ACH along the chordline (assuming the moment axis lay on the chordline). A curve fit of the C_L *vs.* h_0 and C_M *vs.* h_0 data was made using a Matlab smoothing spline for $\alpha = [3, 5, 7, 9, 11]$. The smoothing spline from the Matlab Curve Fitting Toolbox was found to give the best fit of the curves. Furthermore, the toolbox allowed immediate computation of the derivatives of each curve. From this data, the ACH was calculated. The results are discussed in the following chapter.

Chapter 7

Test Results

The force and moment data from the experiments is presented in Appendix E, and the various plots of the data included in Appendix A. This includes data from the pre-test procedures. Based on this data, the observations, interpretation and discussion of the results is made in this chapter. The test correction data is analysed first. This is the data used to correct the lift, drag and pitching moment. The corrected lift, drag and pitching moment data is then analysed, followed by the resolution of the aerodynamic centres in pitch and height for an analysis of the static pitch stability.

7.1 Test Correction Data

7.1.1 Aerodynamic Balance Alignment

The aerodynamic balance alignment was determined by running the wing with the full image support system (figure 6.3), in both the normal and inverted configuration . The wing was positioned at the tunnel centreline and pitched from -10 to 36°.

The normal and inverted curves of C_L *vs.* α (figure 6.4 on page 52) suggested $\alpha_{up.total}$ was large. The analysis yielded a total angle correction of $\alpha_{up.total} = 1.05°$. Therefore, the indicated angle of attack was 1.05° too low.

The normal and inverted curves of C_L *vs.* C_D (figure 6.5 on page 53) illustrate good alignment of the lift and drag vectors relative to the mean airstream. The analysis yielded a local upflow angle, $\alpha_{up} = 0.12°$. Therefore, the flow angularity was up, increasing the angle of attack by 0.12°. This error was of the order of the error in aligning the balance, wing support structure, etc. Upflow was therefore considered negligible, as suggested by the curves.

7.1.2 Tare and Interference

The support tare and interference ($T\&I$) was evaluated by determining its influence at two ground clearances. This included the tunnel centreline ($h = 275\,mm$) and $h = 220\,mm$. From the lift and pitching moment $T\&I$ curves; the magnitude of the $T\&I$ corrections were of the order of the accuracy of the balance transducers at low to medium angles of attack (figure A.3 on page 87). At high angles of attack, the curves illustrate more significant corrections are required. The lift and pitching moment corrections changed in sign several times with increasing angle of attack. The drag $T\&I$ curves indicate the correction was more significant, with the correction an order of magnitude higher than the accuracy of the transducers. The drag correction remained positive, except at very high angles of attack, where it became negative. Figure A.3 clearly illustrates regions in the $T\&I$ curves in which the correction varied with ground clearance.

Although the $T\&I$ corrections had changed with varying ground clearance, since the $T\&I$ analysis was only conducted at two elevation levels, the mean $T\&I$ correction values were applied to all subsequent test data.

7.1.3 Boundary Corrections

The results of the boundary corrections are given in figure A.4 on page 88. This figure shows the total blockage correction factor, ϵ_{total}, as a function of angle of attack, at different values of h_0. The curves indicate that the error in the airstream velocity due to solid and wake blockage was less than 0.5% below the stall angle (approximately 19°). Furthermore, for $-5 < \alpha < 11$ degrees, ϵ_{total} remained approximately constant with α and h_0. The error in the airstream velocity, above the stall angle, increased almost linearly with angle of attack, from 0.5% at stall to approximately 3% at 37°. The maximum error in the airstream velocity was estimated to be 3.4%, which corresponded to an angle of attack of 37° and a ground clearance of $h_0 = 0.12$. Furthermore, the curves suggest the blockage increases with decreasing ground clearance. A plot of the span efficiency factor, e, indicated a significant increase in the effective aspect ratio ($e.AR$) as the wing approached the ground (figure A.5 on page 89).

7.2 Force and Moment Data

7.2.1 Lift Coefficient, $\mathbf{C_L}$

The C_L data is plotted in figure A.6 on page 90 as a function of α and h_0. The following observations are made.

- The data indicates that a reduction in h_0 causes an increase in C_L for $\alpha > 0°$. The C_L at $\alpha = 0°$ is approximately the same for all values of h_0. Negative angles of attack show a decrease in C_L for a reduction in h_0. The lift curve slope, $(\partial C_L / \partial \alpha)_{\alpha=0}$, increases as the ground is approached. The angle of zero lift, α_{L0}, increases from $\alpha = -4.2°$ to $\alpha = -1.6°$, however, this change is small for $h_0 > 0.43$.

- The $C_{L.max}$ increases with decreasing ground clearance, coupled with an increase in the stall angle. The C_L at stall and $h_0 = 0.06$ is approximately 21% higher than that at $h_0 = 1.8$. The average stall angle occurs at $\alpha = 19°$. The maximum stall angle occurs at $\alpha = 23°$ for $0.12 < h_0 < 0.19$. However, for $h_0 = 0.06$ the stall angle is not reached.

- The minimum loss in lift at stall is 4% at $h_0 = 0.12$. The maximum loss in lift at stall is 18% at $h_0 = 1.18$.

- For angles of attack greater than the stall angle, the C_L increases significantly as the ground is approached. The highest recorded increase in C_L is 38% at $h_0 = 0.06$, $\alpha = 23°$. Furthermore, for $0.12 < h_0 < 0.5$ the $C_{L.max}$ does not occur at the stall angle, but at the maximum measured value of α ($= 37°$).

- For positive angles of attack below the stall angle, the data indicates the slopes of the C_L *vs.* h_0 curves change from negative to approximately zero (some positive) over the region $0.25 < h_0 < 0.5$. At approximately $h_0 = 0.25$, a further reduction in h_0 causes as significant increase in C_L and the slope becomes negative again.

Discussion: The data indicates that a reduction in height causes a loss in lift at negative angles of attack, little or no change at zero angle of attack, and an increase in lift at positive angles of attack. The increase in α_{L0} is as a result of the increase in the lift curve slope, $(\partial C_L / \partial \alpha)_{\alpha=0}$. These results correlate well with the results of Fink and Lastinger[18], and, Serebrisky and Biachuev[17]. Furthermore, the highest recorded increase in the C_L is 38% at $h_0 = 0.06$, $\alpha = 23°$. This compares well with figures quoted in the literature[4]. At $h_0 = 1.06$, the curve representing $\alpha = 21°$ indicates an abrupt lowering in the C_L as a result of the lower stall angle.

The $C_{L.max}$ at stall remains approximately constant as the ground is approached. However, for $h_0 < 0.43$ the maximum lift coefficient increases significantly with decreasing ground clearance. For $h_0 < 0.37$, there is a significant increase in the stall angle. In contrast, Serebrisky and Biachuev[17] found a reduction in the stall angle as the ground was approached. However, the decreasing severity of the stall agrees well with the results of Serebrisky and Biachuev. There is insufficient data to examine the stall pattern below $h_0 = 0.12$, however, it appears the wing may eventually cease to stall at these high angles of attack and very low ground clearances. Rozhdestvensky[2] classifies ground clearances of $h_0 < 0.1$ as extreme ground effect. Under these conditions the airflow can stagnate. Since the airflow over the upper surface of the wing is fully separated at these high angles of attack, the source of the additional lift, which prevents the wing from stalling, is thought to be due to a large stagnation pressure on the lower surface of the wing.

For several positive angles of attack, there is a small loss in lift for $0.25 < h_0 < 0.5$. Serebrisky and Biachuev[17] describe this trend of the C_L as a result of a simultaneous increase in the pressure on the lower surface of the wing, and, a decrease in pressure on the upper surface, near the leading edge, as the ground is approached. This produces an increase in the unfavourable pressure gradient on the upper surface, which results in early flow separation. At larger ground clearances, the increase in pressure on the lower surface can be insufficient to compensate for the loss in lift due to early flow separation. This can result in a lower C_L relative to that when the wing is in free air. The plot of C_L *vs.* h_0 clearly shows this loss if C_L at $h_0 = 0.5$ for $-1 < \alpha < 7$. At smaller ground clearances, the increase in pressure on the lower surface is increasingly more than the increase in pressure on the upper surface due to early flow separation. This results in an increase in the lift coefficient, at small ground clearances, above the free air maximum lift coefficient. This is visible in the plot of C_L *vs.* h_0 for $\alpha > 1°$, $h_0 < 0.25$.

The change in the slope of C_L *vs.* h_0 affect the first requirement for the wing to be stable in height. At positive angles of attack, the C_L increases with decreasing h_0. Therefore, the slope of the curve, $\partial C_L/\partial h_0$, is negative and the wing is provisionally stable in height. However, for positive angles of attack below the stall angle, the data indicates a transition of the slope from negative to approximately zero (some positive) over the region $0.25 < h_0 < 0.5$. In these regions the wing becomes marginally stable (or unstable) in height. At negative angles of attack, there is a decrease in the C_L with decreasing h_0. The slope of the curve is positive and the wing is thus unstable in height.

7.2.2 Drag Coefficient, C_D

The C_D data is plotted in figure A.7 on page 91 as a function of α and h_0. The following observations are made.

- The minimum drag coefficient, $C_{D.min}$, occurs at approximately $\alpha = -3°$ for $h_0 > 0.31$. For $h_0 < 0.31$, $C_{D.min}$ occurs at approximately $\alpha = -1°$. $C_{D.min}$ increases from $C_D = 0.023$ at $h_0 = 1.8$, to $C_D = 0.043$ at $h_0 = 0.06$.
- The data indicates a reduction in C_D with decreasing h_0, for $\alpha_{L0} < \alpha < 15$ degrees.
- For $\alpha > 15°$, the C_D increases as the ground is approached.
- The C_D increases by an average of 75% after passing through the stall angle. The smallest increase in drag is approximately 50%, which occurs at $h_0 = 1.06$. The largest increase in C_D is approximately 100%, which occurs at $h_0 = 0.06$.
- Above the stall angle, the C_D increases by up to 46% with decreasing h_0.

Discussion The value of $C_{D.min}$ occurs at low (zero) values of C_L and is usually assumed equal to the profile drag, C_{D0}. C_{D0} is a function of skin friction drag and form drag, which are functions of the profile of the wing, hence the name, profile drag. Furthermore, C_{D0} is ideally independent of AR.

Acknowledging that the tests were conducted at different Reynolds numbers, the values of $C_{D.min}$ are of similar magnitude to the results of Zimmerman[24], and, Fink and Lastinger[18], but greater than those of Serebrisky and Biachuev[17]. Since the wing profile used by Zimmerman is similar to the one used in these experiments, this may explain why the results are similar. However, the profile used by Fink and Lastinger is a substantially thicker (22% thickness ratio) profile. Yet, the values of $C_{D.min}$ are almost identical. The profile used by Serebrisky and Biachuev is a slender 12% thickness ratio wing, but does not have a flat bottom. The $C_{D.min}$ values measured by Serebrisky and Biachuev are approximately half that measured in these experiments. The primary reason for the contrasting $C_{D.min}$ values is thought to be due to a combination of the elevated rear flap on the wing used in these experiments, and, differing test Reynolds numbers. All three wings from references [[17], [18], [24]], are highly streamlined toward the trailing edge and are tested at higher Reynolds numbers.

Below the stall angle, there is a general lowering of the C_D with decreasing h_0. This agrees well with the results of all the references listed above. Serebrisky and

Biachuev ($AR = 5$) and the larger AR wings ($AR > 4$) used by Fink and Lastinger present the most significant reduction in C_D near the stall angle. The larger aspect ratios are thought to be the primary reason for the greater reduction in C_D, at higher angles of attack, through a greater reduction in the C_{Di}. This is in good agreement with general ground effect theory, which predicts a reduction in induced drag[4, 1].

7.2.3 Moment Coefficient, $\mathbf{C_M}$

The C_M data is plotted in figure A.8 on page 92 as a function of α and h_0. The C_M is given relative to the 1/4MAC. The following observations are made.

- For $3 < \alpha < 11$ degrees, the slope of the C_M *vs.* α curves is positive.
- For $-7 < \alpha < 17$ degrees, the slope of the C_M *vs.* h_0 curves is approximately zero for $h_0 > 0.5$. For $h_0 < 0.5$, the slope of the curves becomes negative.
- For $\alpha > 19°$, the CM decreases significantly with decreasing h_0. The large positive slope of the C_M *vs.* h_0 curves is in agreement with this.

Discussion For $3 < \alpha < 11$ degrees, the C_M is not constant with α as identified by the positive slope. Therefore, the ACP cannot be located near the 1/4MAC as stated by ideal aerodynamic theory[25]. Judging by the large positive slope, the ACP is suspected to be forward of the 1/4MAC. However, the C_M is constant with h_0 for $h_0 > 0.5$. This suggests the ACH is located at or near the 1/4MAC.

The nature of the C_M curves agrees well with the data and explanation of the flow field given by Serebrisky and Biachuev[17]. At larger ground clearances, the early flow separation caused by the increased adverse pressure gradient, results in an increase in pressure on the rear half of the upper surface of the wing. This causes an increase in C_M with decreasing h_0, as seen in this experiment for $3 < \alpha < 11$ degrees. Near the stall angle, separation occurs close to the nose of the wing. This causes an increase in pressure in front of the moment axis (1/4 MAC), which results in a net decrease in the pitching moment, as seen in this experiment $\alpha > 13°$.

7.2.4 Polar Diagrams

The C_L *vs.* C_D data is plotted in figure A.9 on page 93 as a function of h_0. The C_L *vs.* C_M data is included at this point for completeness; however, it is re-plotted and discussed in the analysis of the aerodynamic centre in pitch (section 7.3.1). C_M

is given relative to the 1/4MAC. The following observations are made regarding the drag polar data.

- Considering the curves along constant lines of C_L, the following trends are noted. At negative values of C_L there is a reduction in C_D, with decreasing h_0. At approximately $C_L = -0.1$, $C_D = -0.05$, C_L and C_D remain approximately constant for all values of h_0. For $-0.1 < C_L < 0.4$, C_D increases with decreasing h_0. $C_{D.min}$ occurs at approximately $C_L = 0$. At approximately $C_L = 0.4$, $C_D = -0.05$, C_L and C_D remain roughly constant for all values of h_0. For $0.4 < C_L < 1$, a reduction in h_0 results in a reduction in C_D.
- The maximum lift coefficient before stall increases from $C_L = 0.98$ at $h_0 = 1.3$, to $C_L = 1.14$ at $h_0 = 0.12$. However, the drag simultaneously increases from $C_D = 0.2$, to $C_D = 0.44$. There is insufficient data on the stall characteristics at $h_0 = 0.06$.
- The minimum loss in lift at stall is 4% at $h_0 = 0.12$. The maximum loss in lift at stall is 18% at $h_0 = 1.18$. Following stall, there is a marginal increase in C_L at constant values of h_0. However, the C_D increases by an average of 40%.

Discussion The minimum drag coefficient, $C_{D.min}$, occurs at approximately $C_L = 0$. This agrees with basic aerodynamic theory[25] and with the results of Serebrisky and Biachuev[17], and, Fink and Lastinger[18]. Furthermore, for $-0.1 < C_L < 0.4$, C_D increases with decreasing h_0. Over this region, C_D is primarily due to skin friction and form drag, which suggests a net increase in these two effects as the ground is approached. At $C_L = 0.4$, $C_D = -0.05$, C_L and C_D remain approximately constant for all values of h_0. For $C_L > 0.4$, the increased efficiency of ground effect is demonstrated by an increase in the slope of the C_L *vs.* C_D curves as the ground is approached. Furthermore, $C_{L.max}$ at stall clearly increases with decreasing ground clearance. However, the C_D at stall is seen to simultaneously increase under these conditions, and the efficiency of the wing rapidly deteriorates. In contrast with Serebrisky and Biachuev, the $C_{L.max}$ at stall also increased with decreasing ground clearance, however, they found C_D decreased at stall. The plot further illustrates the ability of the wing to maintain high values of C_L after stall. This is particularly so for $h_0 < 0.25$. However, the high values of C_D would make it highly impractical to operate the wing under these conditions.

7.2.5 Lift/Drag Ratio

The L/D ratio data is plotted in figure A.10 on page 94 as a function of C_L and h_0. The following observations are made.

- At $h_0 = 1.55$, the maximum L/D ratio, $L/D_{max} = 9.7$ at $C_L = 0.44$ ($\alpha = 3°$).

- At $h_0 = 0.06$, $L/D_{max} = 13.1$ occurs at $C_L = 0.75$ ($\alpha = 5°$). This is the highest L/D ratio of the test.

- The lowest value of $L/D_{max} = 8.5$ at $C_L = 0.62$, $h_0 = 0.62$.

- For $C_L < 0.4$, L/D decreases with decreasing h_0. The plot of L/D *vs.* h_0, for $\alpha < 3°$, shows a further decrease in L/D with decreasing h_0.

- For $0.8 < C_L < C_{L.max}$ at stall, L/D increases with decreasing h_0. This corresponds to $7 < \alpha < 19$.

- An increase in C_L (α) from L/D_{max} to the $C_{L.max}$ before stall, indicates the L/D ratio drops by approximately 50% at $h_0 = 1.55$ and 80% at $h_0 = 0.06$.

- For $\alpha > 23°$, L/D decreases with α, but remains constant with h_0.

- The lowest value of $L/D = 1.4$ (for $C_L > 0$) occurs at $\alpha = 37°$ for all values of h_0.

Discussion The data indicates a 35% increase in L/D_{max} for a reduction in ground clearance from $h_0 = 1.55$ to $h_0 = 0.06$. The corresponding angle of attack increased from $\alpha = 3°$ to $\alpha = 5°$. However, as the ground clearance was reduced, L/D_{max} first decreased, before increasing again to reach the maximum L/D ratio of the test. The L/D_{max} of the test was 13.1 for a lift coefficient of $C_L = 0.75$. In comparison with the wing of AR 2 used by Fink and Lastinger[18], at the same ground clearance, the $L/D_{max} = 17$ was produced at $C_L = 1.1$. The wing of AR 4 produced a $L/D_{max} = 35$ at $C_L = 1.5$. However, the corresponding L/D_{max} is similar in magnitude when out of ground effect. It is clear from these tests that both an increased AR and a decrease in ground clearance, significantly improve the L/D_{max} of the wing.

7.3 Aerodynamic Centres

7.3.1 Aerodynamic Centre in Pitch

The resolution of the position of the aerodynamic centre in pitch (ACP), for constant values of h_0, is presented in this section. The C_M *vs.* C_L data is plotted in figure A.11 on page 95 as a function of α. C_M is given relative to the 1/4MAC. Body-fixed axes are defined relative to this point, and are aligned forward, starboard, and down (figure 2.8). The region of interest on this curve is that corresponding to

$0 < \alpha < \alpha_{stall}$. This represents the limits of the expected flight cruise angles. The following observations are made.

- For $0.2 < C_L < 0.45$, the slope of the curves is approximately zero, except for $h_0 = 0.06$ and $h_0 > 0.43$. Over these regions the slope is predominantly negative.
- For $0.45 < C_L < 0.9$, the slope of the curves is positive. At $h_0 = 0.06$, the slope of the curve is both positive and negative.

Discussion As specified by equation 2.8, the slope of the curves gives the distance to the location of the ACP as a function of α, for constant values of h_0. The distance is given in percentage chord and is relative to the moment axis. For $0.2 < C_L < 0.45$ and $h_0 < 0.43$, the horizontal slope indicates the C_M is approximately constant with C_L. Therefore, the position of the ACP is approximately at the 1/4MAC at these lower ground clearances. For $h_0 > 0.43$, the slope is negative, therefore, the ACP must lie backward (i.e. toward the trailing edge) of the 1/4MAC. For $0.45 < C_L < 0.9$, with the exception of $h_0 = 0.06$, the slope of the curves is positive. Therefore, the ACP must lie somewhere forward of the 1/4MAC. The slope decreases with decreasing h_0, therefore, the ACP must approach the 1/4MAC with decreasing h_0.

It was decided to track the ACP, as the wing entered ground effect, by resolving the forces and moments as given by equation 2.11. Solving this equation would allow the movement of the ACP along the chord and above/below the chord to be tracked. The data was linearised over the region $0.45 < C_L < 0.9$, corresponding to $3 < \alpha < 11$ degrees, and the results of the determination of the ACP, over this region, are illustrated in figure A.12 on page 96. The x/c position of the ACP is given relative to the leading edge (LE) of the wing with positive being backward. The positive direction of z/c is down. The results indicate that the position of the ACP essentially remains at $x/c = 0.18$ for $h_0 > 0.5$. For $h_0 < 0.5$ the ACP moves toward the trailing edge (TE). At $h_0 = 0.06$ the ACP is located at approximately $x/c = 0.25$. This trend of the ACP moving toward the TE, at low ground clearances, is in good agreement with Rozhdestvensky[2]. The wing used in his analysis is a 2-D $NACA - 0008$ profile with a flat lower surface and a lower trailing edge spoiler. His analysis shows the movement of the ACP as a function of the parameter (θ/h_0). Choosing $\theta = 3°$, several values of X_α are plotted in figure A.12. The results show the ACP is initially close to the chordline and moves down with decreasing h_0. At low ground clearances the ACP moves back toward the chordline. At $h_0 = 1.3$ the ACP is located at $z/c = -0.002$. The greatest deviation below the chordline is $z/c = -0.006$ and occurs at $h_0 = 0.5$. At $h_0 = 0.06$ the ACP is located at $z/c = -0.0003$. This indicates the vertical position of the ACP is essentially uninfluenced by the presence of the ground, and, assuming it to lie on the chordline, is a good approximation for this wing.

The moment data was transferred to the location of the ACP corresponding to each value of h_0. The results in figure A.12 clearly show the pitching moment is approximately constant for $5 < \alpha < 11$ degrees and all values of h_0.

7.3.2 Aerodynamic Centre in Height

The resolution of the position of the aerodynamic centre in height (ACH), for constant values of α, is presented in this section. The C_M *vs.* C_L data is plotted in figure A.13 on page 97 as a function of h_0. C_M is given relative to the 1/4MAC. The region of the curve of interest is that corresponding to $0 < \alpha < \alpha_{stall}$. This represents the limits of the expected flight cruise angles. The following observations are made.

- For $3 < \alpha < 11$ degrees, the data illustrates the curves form an 'S' shape.
- For $11 < \alpha < 19$ degrees, the data illustrates the curves form an inverted 'V' shape.

Discussion As specified by equation 2.12, the slope of the curves gives the distance to the location of the ACH as a function of h_0, for constant values of α. The distance is expressed in percentage chord and relative to the moment axis. For $3 < \alpha < 11$ the S-shape means the curve has positive and negative infinite gradients. Therefore, X_h is expected to take on infinite positive and negative values. This immediately breaks the condition for static stability as defined by equation 2.20. The shape of the curves, for these values of α, come as a direct result of a small loss in lift at $h_0 = 0.5$ (figure A.6). This was identified as a failure of the first condition for static height stability, $\partial C_L/\partial h_0 < 0$ (equation 2.17), and, illustrates how X_h is affected by a failure to meet this condition. For $11 < \alpha < 19$ degrees, the curves illustrate large positive and negative gradients. Therefore, X_h is expected to move forward and backward from the 1/4MAC.

The position of the ACH, as a function of h_0, was calculated as specified by equation 2.12. This tracked the movement of the ACH along the chordline. A curve fit of the C_L *vs.* h_0 and C_M *vs.* h_0 data was made for α = 3, 5, 7, 9, 11 degrees. The derivative of each curve was made in Matlab (figure A.14 on page 98). $\partial C_L/\partial h_0$ clearly takes on positive values for $0.2 < h_0 < 0.5$, thus violating the first condition for static height stability (equation 2.17). From this data, the ACH was calculated. The results are presented in figure A.15 on page 99. The x/c position is given relative to the leading edge (LE) of the wing with positive backward. Included in the figure is the position of the ACP for each corresponding value of h_0. For $h_0 > 0.5$, the figure indicates the position of the ACH is approximately at the 1/4MAC, but changes with α and h_0. The ACH is predominantly behind the ACP, therefore, the second condition for static height stability has failed, namely, $X_h - X_\alpha > 0$ is not true (equation 2.12). For $h_0 < 0.5$, the figure indicates significant movement of the ACH, as expected by the infinite gradients seen in figure A.13. This further illustrates the requirement that $\partial C_L/\partial h_0 < 0$ for all values of h_0 in the normal flight regime. For comparative purposes, the ACH and ACP from Rozhdestvensky's[2] 2-D $NACA - 0008$ profile are included in figure A.15. This wing demonstrates a positive static stability margin ($SSM = X_h - X_\alpha$) and is thus stable in height. However, the SSM is seen to decrease as the ground is approached.

A further examination of the problem was made by considering the curve of $\alpha = 3°$ from figure A.13 (see figure A.16 on page 100). The slope of this curve indicated the position of ACH as a function of h_0 and is estimated along two relatively linear regions. The figure indicates the ground clearance at various points along the curve. The estimated slopes of the linearised regions and corresponding ground clearance are given below:

$$m_1 = X_{h1} = 0 \qquad (0.5 < h_0 < 1.55)$$

$$m_2 = X_{h2} = -0.9 \; (0.25 < h_0 < 0.5)$$

For $0.5 < h_0 < 1.55$, the slope is approximately zero. Therefore, X_{h1} is approximately zero and the ACH is located at the moment axis (1/4MAC). A closer examination of the C_M *vs.* h_0 at $\alpha = 3°$ (figure A.17 on page 101) indicates the C_M is approximately constant for $0.5 < h_0 < 1.55$, as expected. Outside this region the C_M is seen to increase with decreasing h_0. For $0.25 < h_0 < 0.5$, the slope is approximately $m_2 = -0.9$ (figure A.16). Transferring the C_M data to a point $x/c = 0.9$ behind the 1/4MAC ($x/c = 1.15$ behind the LE), the corresponding data is re-plotted in figure A.18 on page 102. The corresponding range of h_0 values is indicated in the figure. The slope of C_M *vs.* C_L in this range is approximately zero, indicating the new moment axis location as the ACH for these values of h_0. The plot of C_M *vs.* h_0 indicates the moment is constant over these h_0 values. Outside this region, the moment varies with h_0 as indicated by the non-zero slope of C_M *vs.* h_0.

Chapter 8

Conclusions

8.1 Test Apparatus

8.1.1 TEM Balance Elevator

The design criteria originally specified for the balance elevator were;

1. The balance-elevator system must maintain adequate alignment under aerodynamic loading and changes in elevation.
2. The change in elevation should exceed the half height of the tunnel.
3. The change in elevation should occur in the vertical direction only.

Based on the results of the aerodynamic balance alignment, the balance-elevator system performed well in maintaining alignment. The upflow angle was determined to be $\alpha_{up} = 0.12^{\circ}$. Any misalignment in the balance elevator system would have contributed to a larger α_{up} value. The elevation range was adequate for the experiments carried out. This range allowed testing of the wing at both the centreline of the tunnel and at ground clearances down to $10\,mm$. Finally, the change in elevation does occur in the vertical direction only. Therefore the model does not move in the streamwise direction with a change in elevation. Based on the foregoing discussion, it can be concluded that the balance-elevator system performed well.

8.1.2 The TEM Balance and the Wing Support System

The TEM balance and the wing support system both performed well for the duration of the test. However, the design of the trunnion points posed a minor restriction in the range of test configurations. This became evident at very low ground clearances and very high angles of attack, but still functioned well within the scope of this investigation.

8.1.3 Moving-Belt Ground System

The design criteria originally specified for the moving-belt ground system were;

1. Easy installation and removal from the tunnel.
2. Maximum belt speed should equal maximum tunnel jet velocity ($\approx 30\,m/s$).

The basic geometry of the ground simulation system allowed for easy installation and removal from the tunnel. The maximum belt speed was tested to the maximum test-section velocity ($\approx 30\,m/s$). Thus, it was concluded that the moving-belt ground plane performed as required.

8.2 Data Corrections: Aerodynamic Balance Alignment

The analysis indicated that $\alpha_{up.total}(= 1.05°)$ did not equal $\alpha_{up}(= 0.12°)$. The total angle correction indicated the angle of attack was too low. The upflow was considered negligible; this suggested an error of approximately 1° lay between the indicated angle of attack and the pitching mechanism. This was supported by the discovery of an error in the angle of attack gauge during the pre-test calibration of the balance. The angle of attack gauge was found to under read the angle by approximately 1°. It was concluded that this was the source of the large $\alpha_{up,total}$ value.

8.3 Test Results

The results indicate that as the ground is approached the wing experiences an increase in lift-curve slope and a reduction in induced drag, which results in an increase in lift-drag ratio. The results indicate the position of the ACP essentially remains at $x/c = 0.18$ for $h_0 > 0.5$. For $h_0 < 0.5$ the data indicates a rearward shift of the ACP. Furthermore, the vertical position of the ACP is essentially uninfluenced by the presence of the ground, and, assuming it to lie on the chordline, is a good approximation for this wing. For $h_0 > 0.5$, the data indicates the position of the ACH is approximately at the 1/4MAC, but changes with α and h_0. At lower ground clearances, the data indicates significant movement in the position of the ACH. It is concluded that this is a result of a temporary loss in lift as the ground is approached. Therefore, the first condition for static height stability, namely $\partial C_L / \partial h_0$, is not negative for all values of h_0. The data from this analysis indicates that the ACH is predominantly behind the ACP, therefore the static stability margin, SSM, is predominantly negative. Based on these findings, the wing was concluded to be unstable in ground effect.

Chapter 9

Recommendations

Based on the results and conclusions of this experiment, the following recommendations are made for improvement of the test apparatus and the experimental methods.

9.1 Extend the range of test combinations of angle and ground clearance

Sixty one combinations of angle of attack and ground clearance were not physically possible, primarily due to design of the trunnion points. Although the impact on this investigation was minor, it is recommended that the trunnion points be redesigned to allow a greater range of movement should it be required. Furthermore, the full range of the elevator system is not being utilised. It is proposed that the method for changing elevation be re-evaluated and redesigned to make full use of the available range. A remotely operated elevator is strongly recommended for the safety and convenience issues.

9.2 Recommended correction for the error in indicated pitch angle

The error in the angle of attack reading discovered during the alignment and flow angularity analysis is considered significant. However, it is recommended that no attempt be made to remove the error due to the delicate nature of the balance. The error is known, and is a simple correction to apply to the data.

9.3 Improve flow angularity for evaluation of bodies in ground effect

The test-section currently makes no use of any flow correction devices. This requires flow angularity to be evaluated for each model configuration. It is recommended that a uniform parallel flow field be established close to the moving belt using the necessary flow correction devices. For tests conducted close to the ground, no flow angularity correction need be applied. Models tested out of ground effect must occur with the moving-belt ground system removed from the test-section, with flow angularity analysed as normal.

References

[1] Wieselsberger, C., "Wing Resistance Near the Ground," Technical Memorandum TM 77, NACA, April 1922.

[2] Rozhdestvensky, K. V., *Aerodynamics of a Lifting System in Extreme Ground Effect*, Springer, 2000.

[3] Losi, P. C., "The Wingship's Potential For Strategic Lift," Tech. rep., The Industrial College of the Armed Forces, 1995.

[4] van Opstal, E., "Introduction to WIG Technology," *Proceedings of the EuroAvia Ground Effect Symposium*, edited by S. Aubin, Euroavia Toulouse, SUPAERO, Toulouse, June 12-15 2001, pp. 13–44.

[5] van Opstal, E., The WIG Page, http://www.se-technology.com/wig, January 2004.

[6] Barlow, J. B., Rae, W. H., and Pope, A., *Low-Speed Wind Tunnel Testing*, John Wiley & Sons, Inc., 3rd ed., 1999.

[7] Stevens, B. L. and Lewis, F. L., *Aircraft Control and Simulation*, John Wiley & Sons, Inc., 2nd ed., 2003.

[8] Irodov, R. D., "Criteria of Longitudinal Stability of Ekranoplan," *Ucheniye Zapiski TSAGI*, Vol. 1, No. 4, 1970, pp. 63–74.

[9] Kumar, P. E., "On the Longitudinal Stability of a Ground Effect Wing," Tech. Rep. Aero 202, College of Aeronautics Report, 1968.

[10] Staufenbiel, R. and Kleineidam, G., "Longitudinal Motion of Low-Flying Vehicles in Nonlinear Flowfields," *Proceedings of the Congress of the International Council of the Aeronautical Sciences*, FRG, Munich, 1980, pp. 293–308.

[11] Zhukov, V. I., "Some Matters of Longitudinal Stability of Ekranoplans," *Trudy TSAGI*, 1974.

[12] Widnall, S. E. and Barrows, T. M., "An Analytic Solution for Two and Three-Dimensional Wings in Ground Effect," *Journal of Fluid Mechanics*, Vol. 41, No. 4, 1970, pp. 769–792.

[13] Huminic, A. and Lutz, T., "CFD Study of Ground Simulation Techiniques," *4th International Conference on Heat Transfer, Fluid Mechanics and Thermodynamics*, HEFAT2005, Cairo, Egypt, 2005.

[14] Chun, H. H. and Park, I. R., "Analysis of Steady and Unsteady Performances for 3-D Airwings in the Vicinity of the Free Surface," *Proc. International Workshop "Ekranoplans - Flying Ships of the 21st Century"*, The University of New South Wales, November 7-9 1995, pp. 23–46.

[15] Park, I. R. and Chun, H. H., "Numerical Simulation of Unsteady Performance of 2-D Surface Effect Airfoils," *Journal of Ships and Ocean Engineering*, Vol. 10, No. 1, November 1995.

[16] van V Pienaar, D., *Longitudinal Stability and Control Analysis and Parameter Sensitivity Investigation of Fixed Wing Aircraft in Ground Proximity Using Various Aerodynamic Approaches*, Ph.D. thesis, University of Cape Town, 2000.

[17] Serebrisky, Y. M. and Biachuev, S. A., "Wind-Tunnel Investigation of the Horizontal Motion of a Wing Near the Ground," Technical Memorandum TM 1095, NACA, September 1946.

[18] Fink, M. P. and Lastinger, J. L., "Aerodynamic Characteristics of Low-Aspect-Ratio Wings in Close Proximity to the Ground," Technical Note TN D-926, NASA, 1961.

[19] Furlong, G. C. and Bollech, T. V., "Effect of Ground Interference on the Aerodynamic Characteristics of a 42deg Sweptback Wing," Technical Note TN 2487, NACA, October 1951.

[20] Kim, M. S. and Geropp, D., "Experimental Investigation of the Ground Effect on the Flow Around some Two-Dimensional Bluff Bodies with Moving-Belt Technique," *Journal of Wind Engineering and Industrial Aerodynamics*, Vol. 74-76, 1998, pp. 511–519.

[21] Turner, T. R., "A Moving-Belt Ground Plane for Wind-Tunnel Ground Simulation and Results for Two Jet-Flat Configurations," Technical Note TN D-4228, NASA, November 1967.

[22] Maskell, E. C., "A Theory of the Blockage Effects on Bluff Bodies and Stalled Wings in a Closed Wind Tunnel," Tech. rep., ARC R&M 3400, 1965.

[23] North, J., *Clay Pattern Styling and Rigid Surface Casting In Today's Composite Industry*, Chavant Inc., http://www.chavant.com, January 1999.

[24] Zimmerman, C. H., "Characteristics of Clark Y Airfoils of Small Aspect Ratios," Tech. Rep. 431, NACA, May 1932.

[25] Kuethe, A. M. and Chow, C.-Y., *Foundations of Aerodynamics*, John Wiley & Sons, Inc., 5th ed., 1998.

[26] Belinskiy, V. G., "Maximum and Average Magnitudes of Hydrodynamic Characteristics of the Wing, Moving above Nonplanar Ground," *Gidromekhanika*, Vol. 11, No. 9, 1974, pp. 528–536.

[27] Grebeshov, E. P., Shakarvene, E. P., and Tsvetkova, G. I., "Aerodynamic Characteristics of a Wing in Proximity of Flat and Wavy Ground," *Trudy TSAGI*, Vol. 1725, 1976, pp. 3–28.

Appendix A

Data Plots

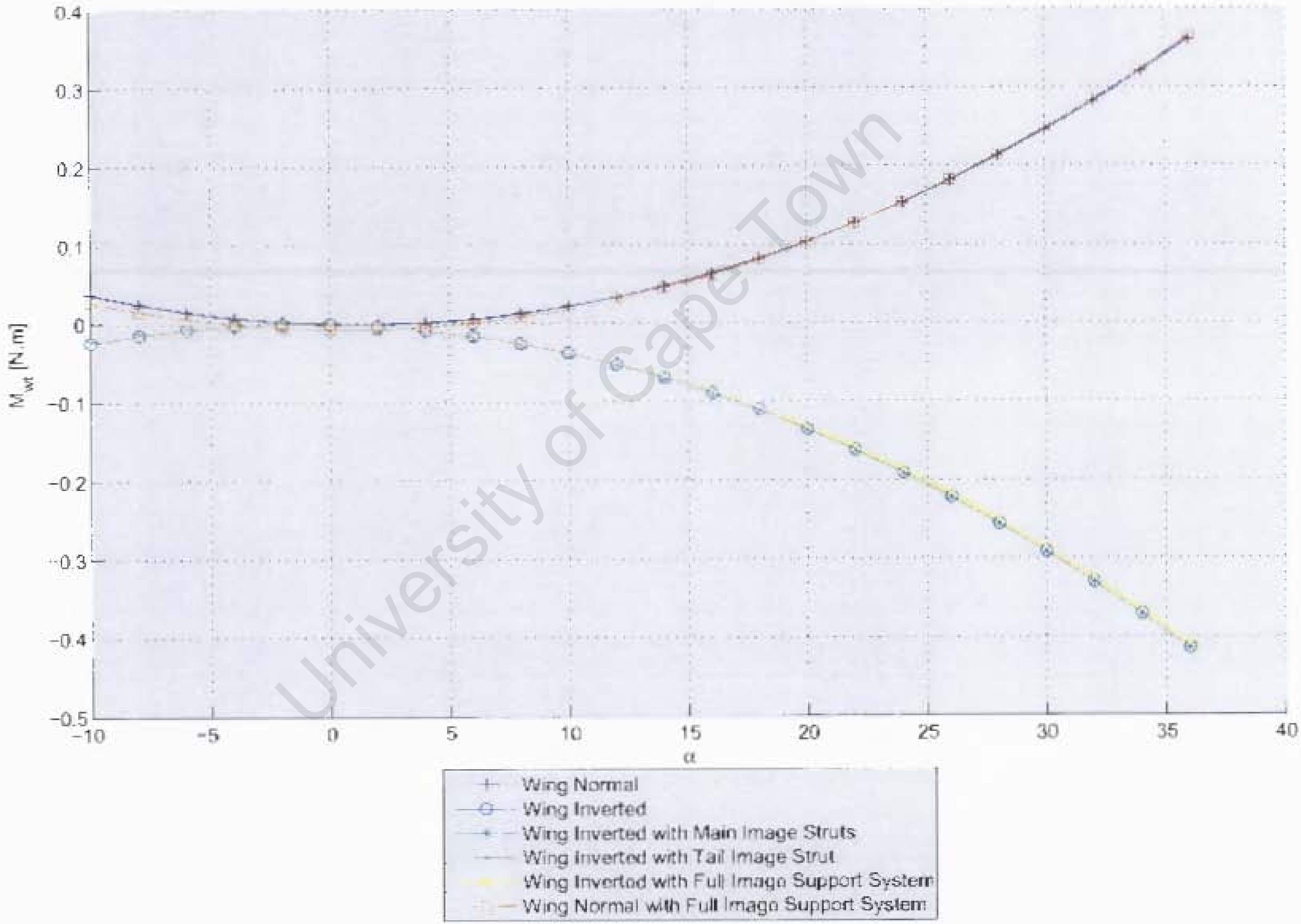

Figure A.1: Weight tare correction as function of α

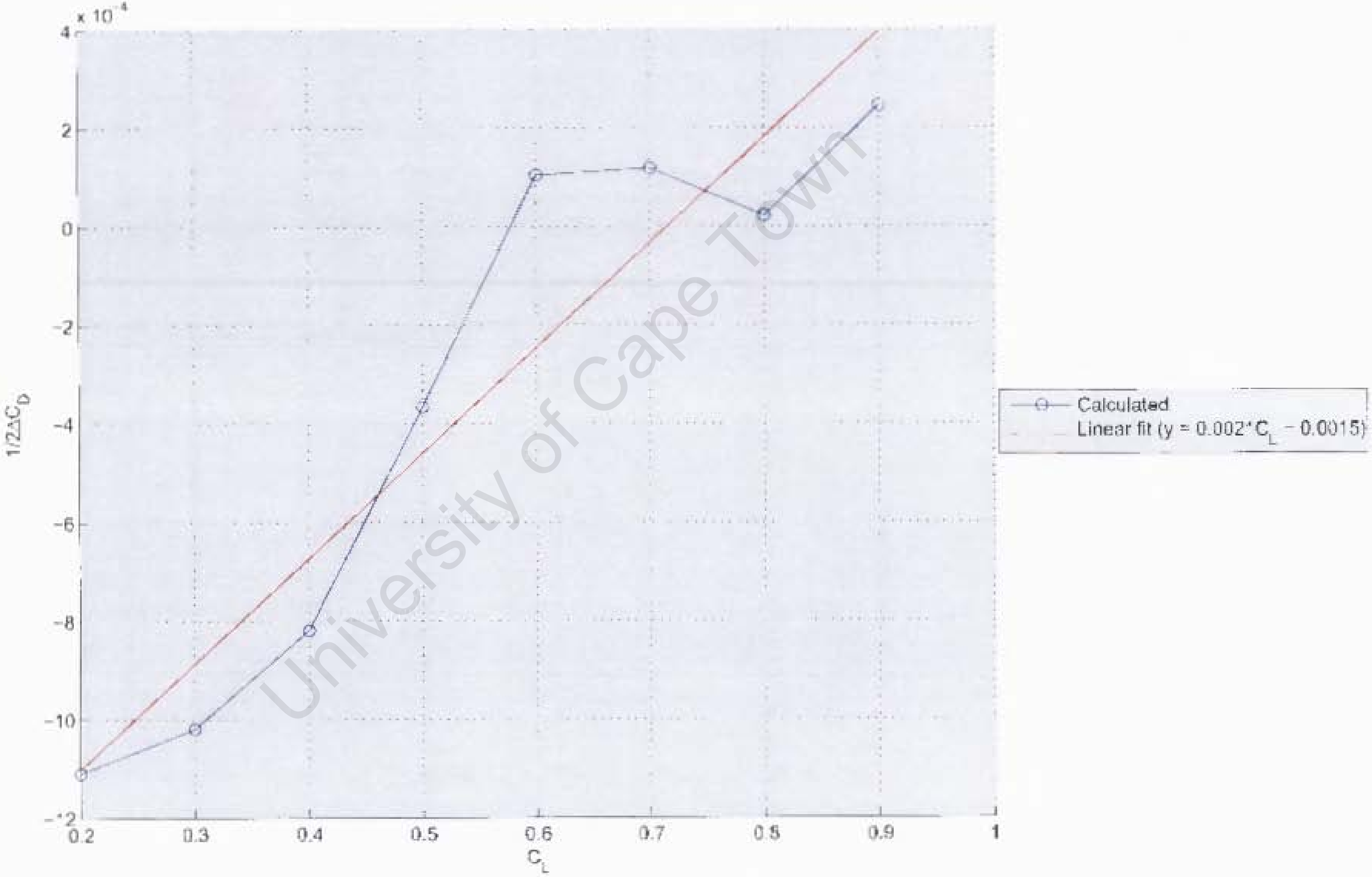

Figure A.2: Calculation of tan α_{wp}

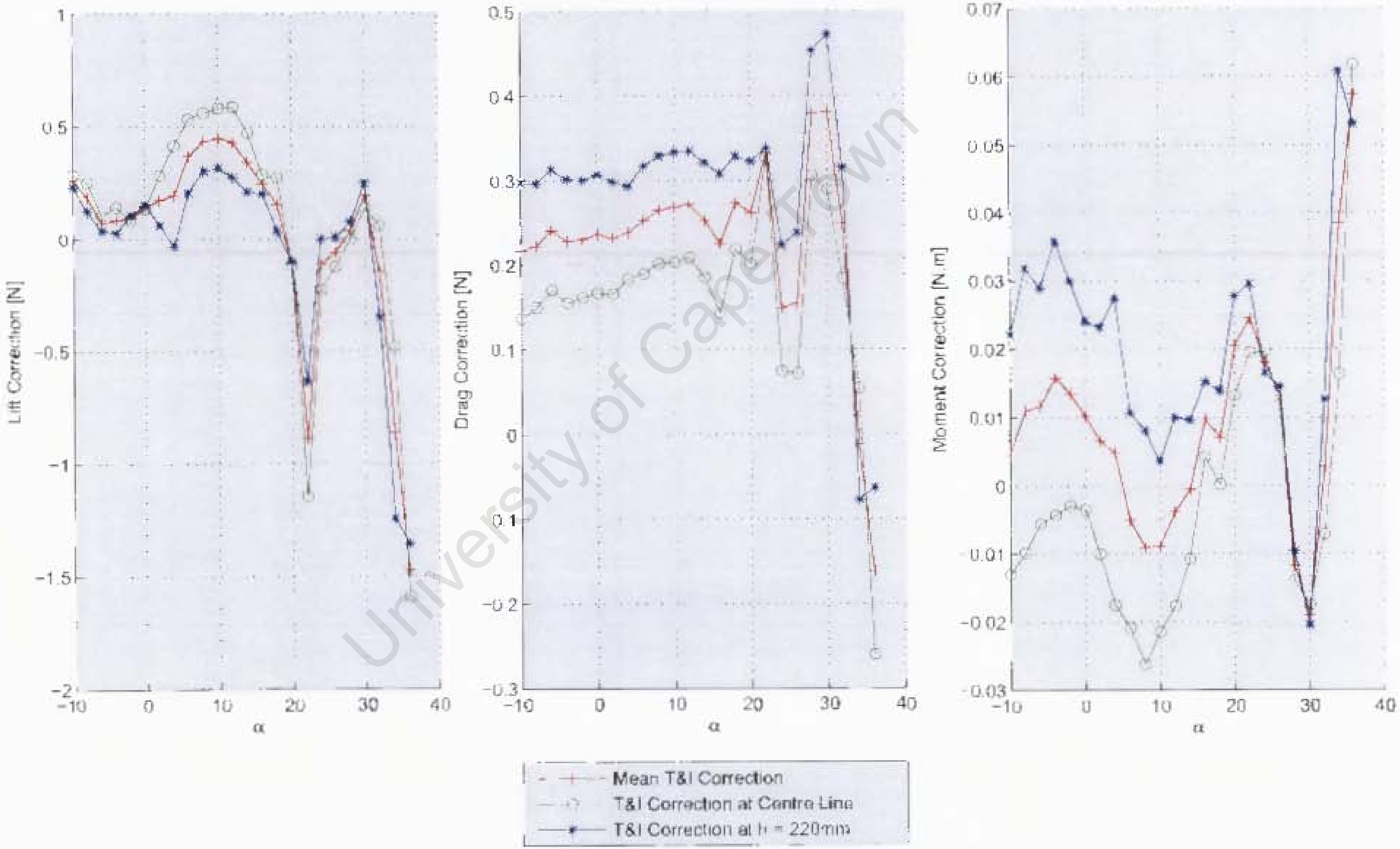

Figure A.3: Tare and Interference Data

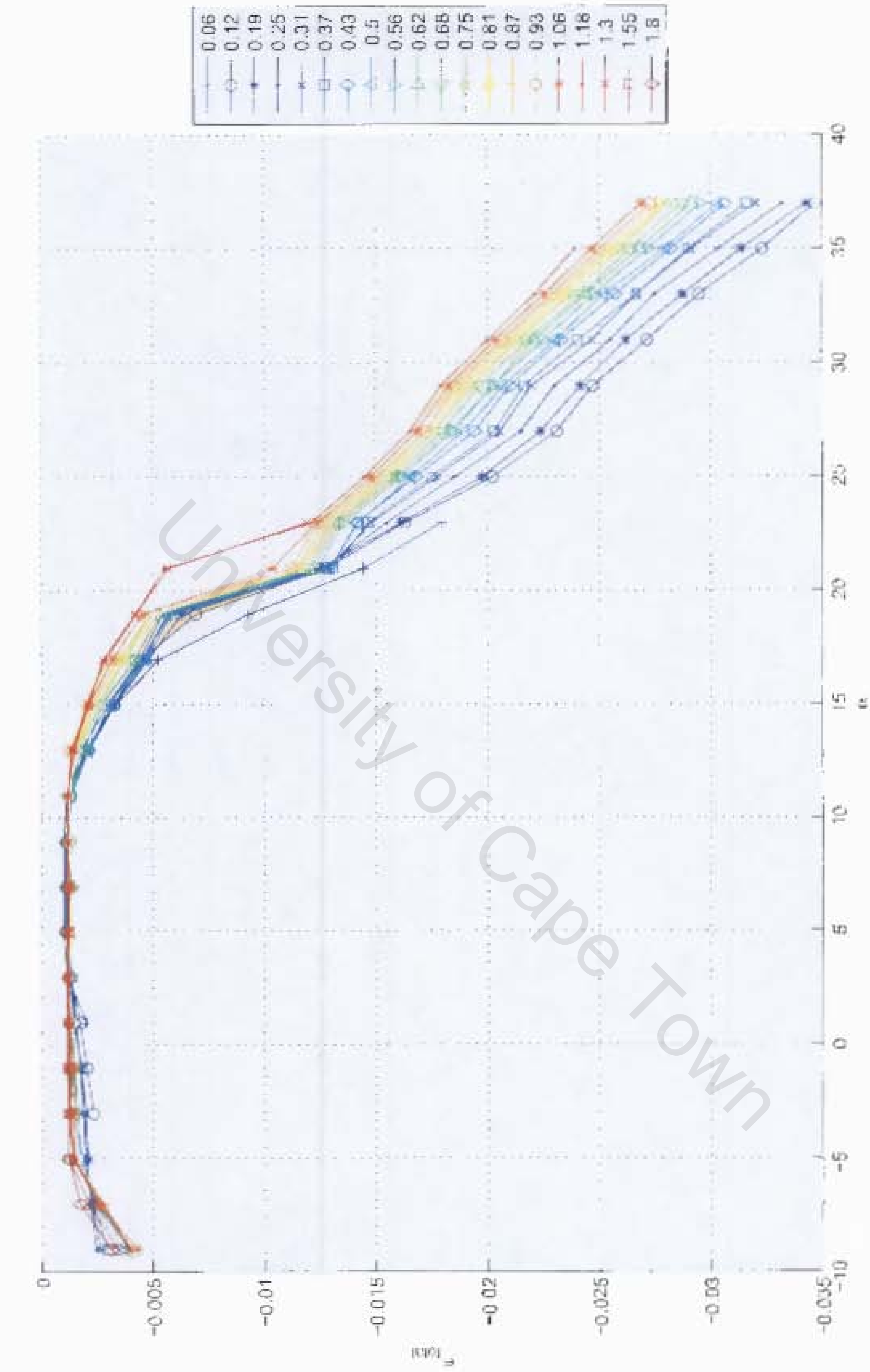

Figure A.4: Total blockage correction factor, ϵ_{total}

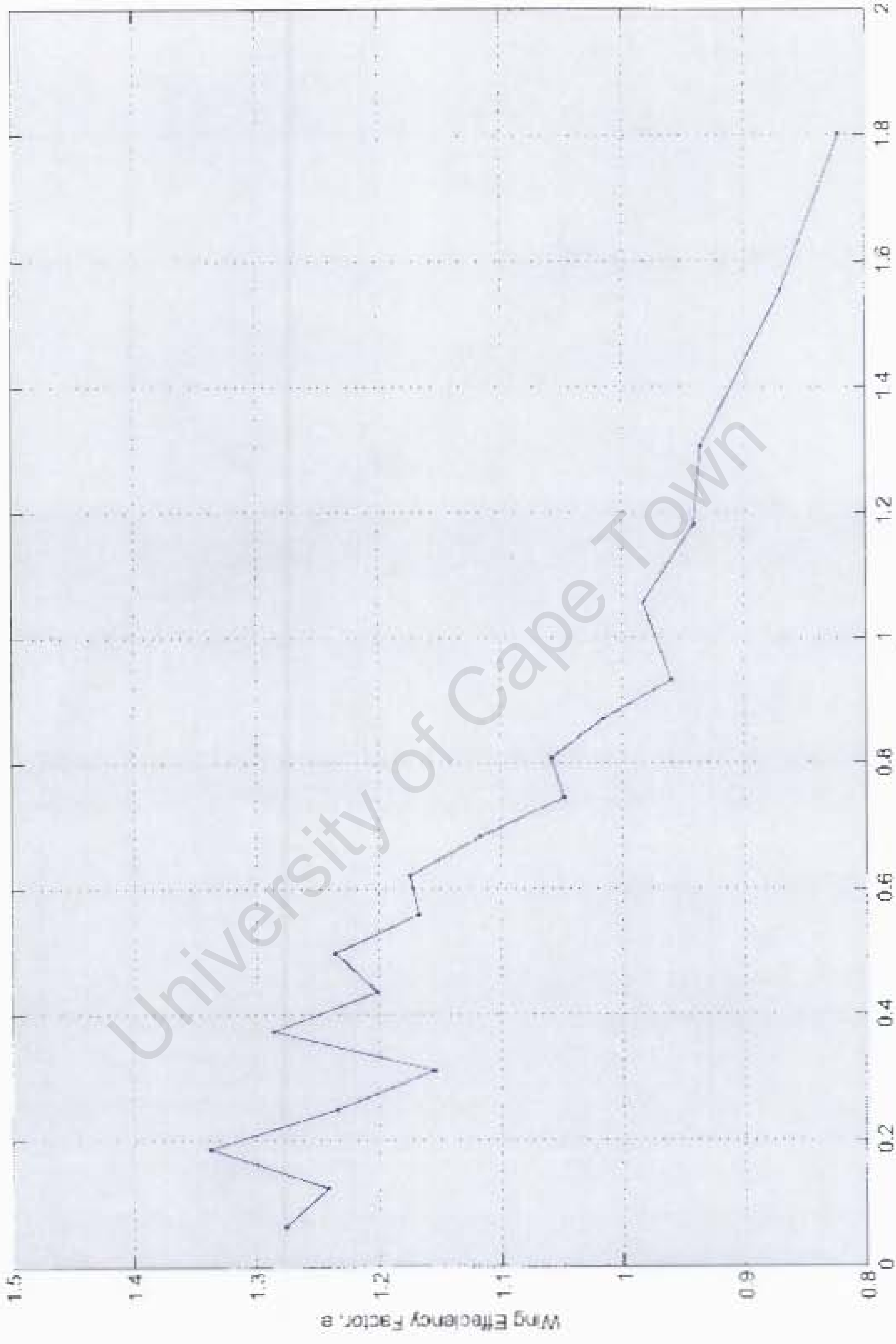

Figure A.5: Variation of span efficiency factor, e, with h_0

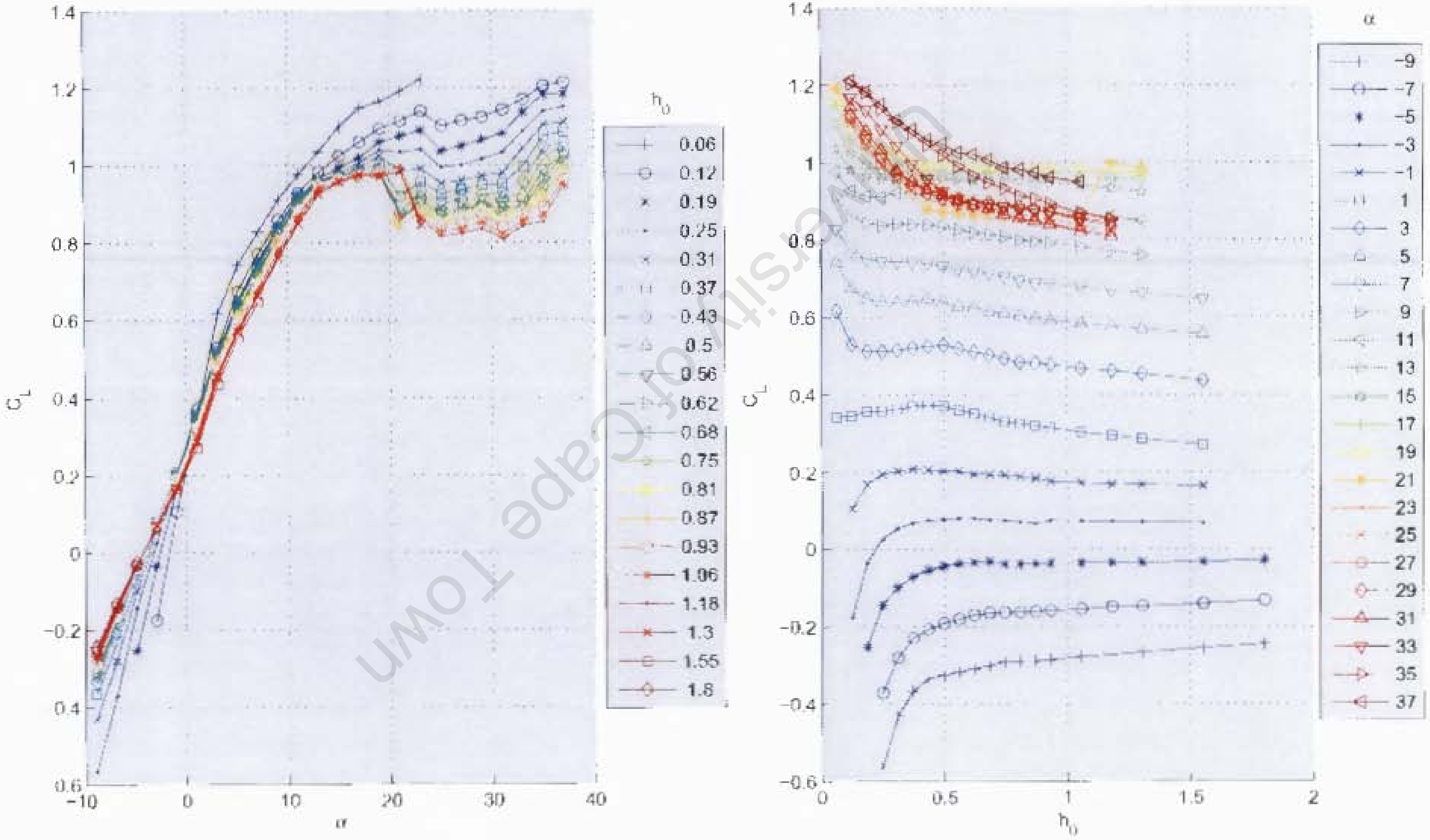

Figure A.6: C_L vs. α and h_0

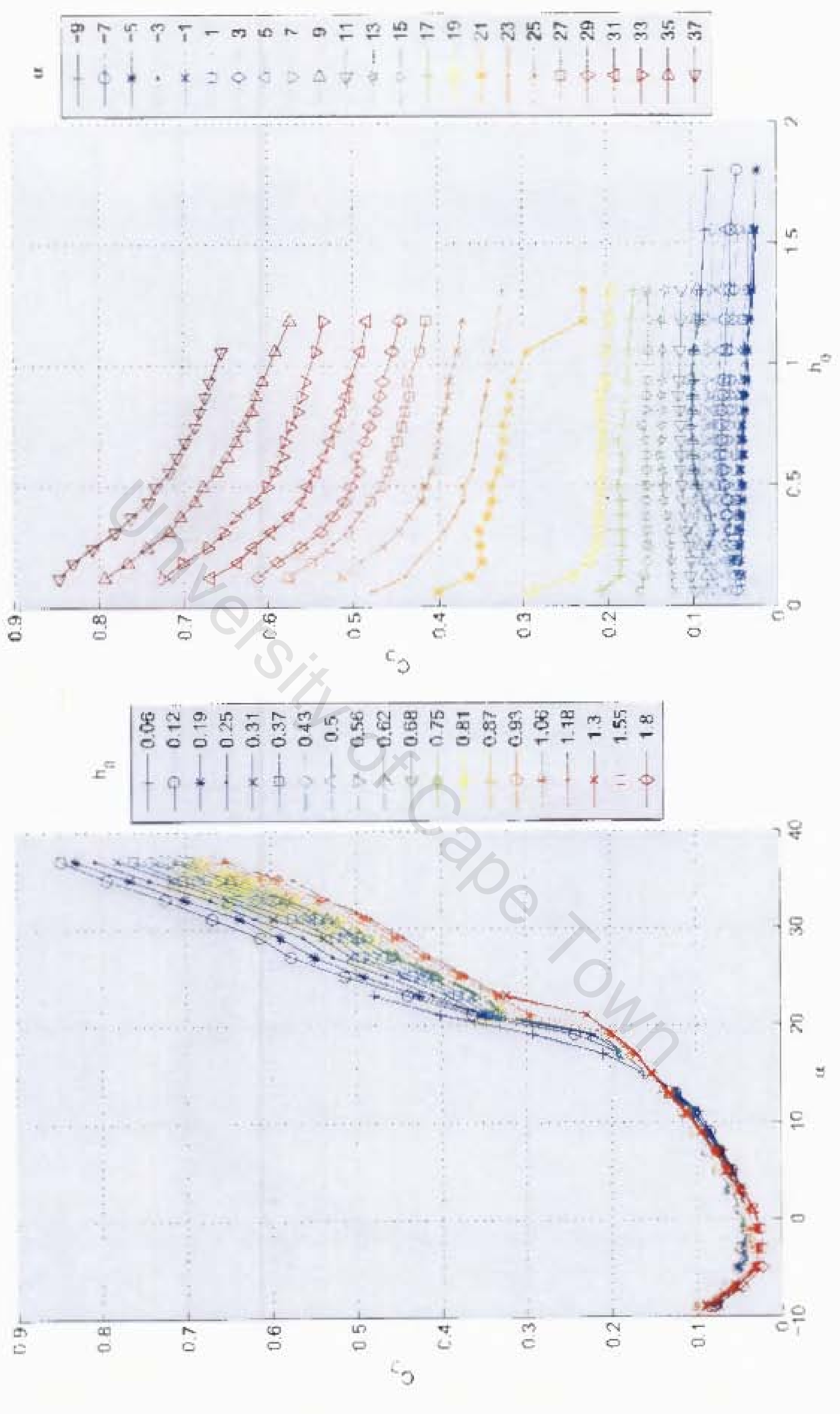

Figure A.7: C_D *vs.* α and h_0

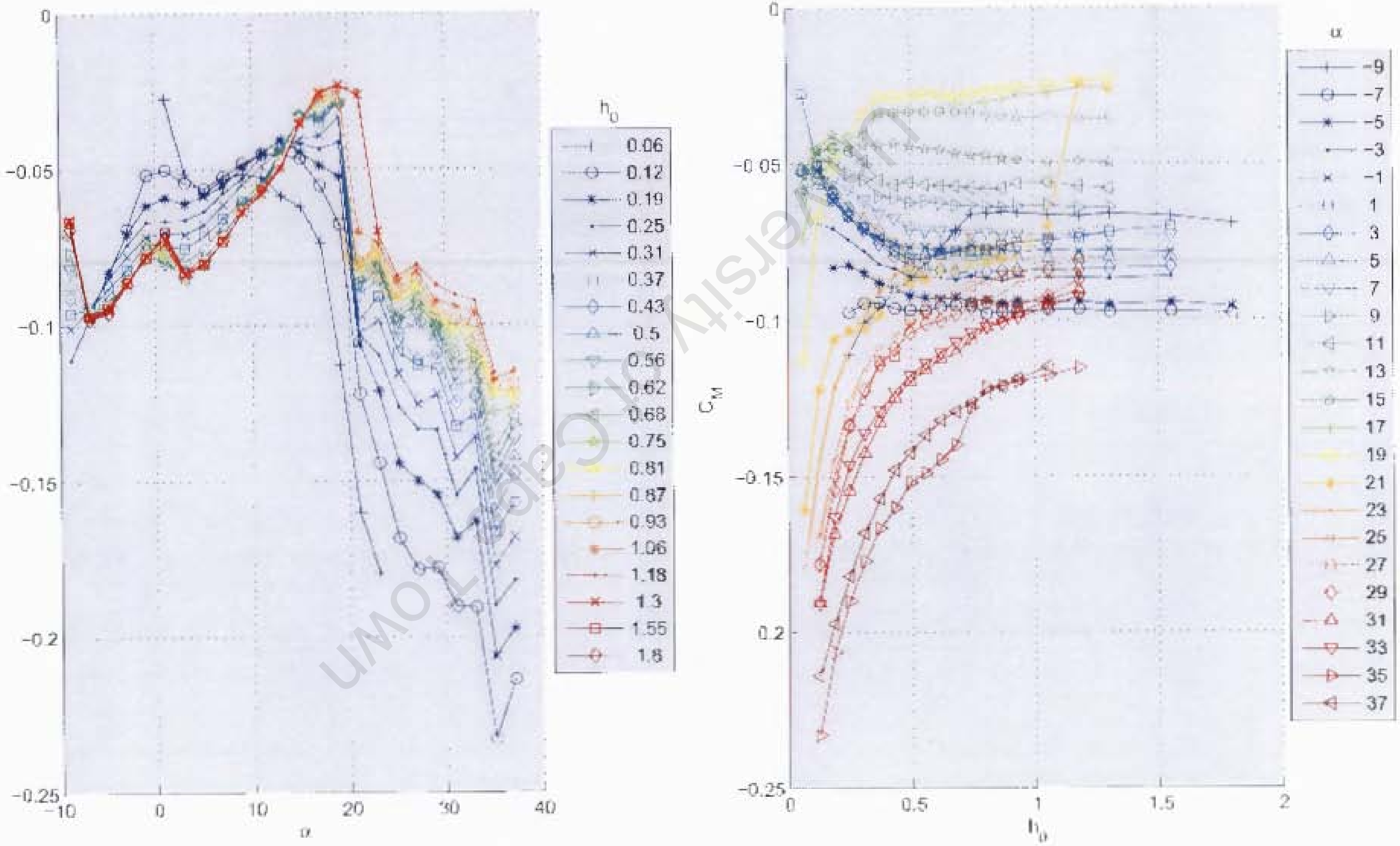

Figure A.8: C_M vs. α and h_0

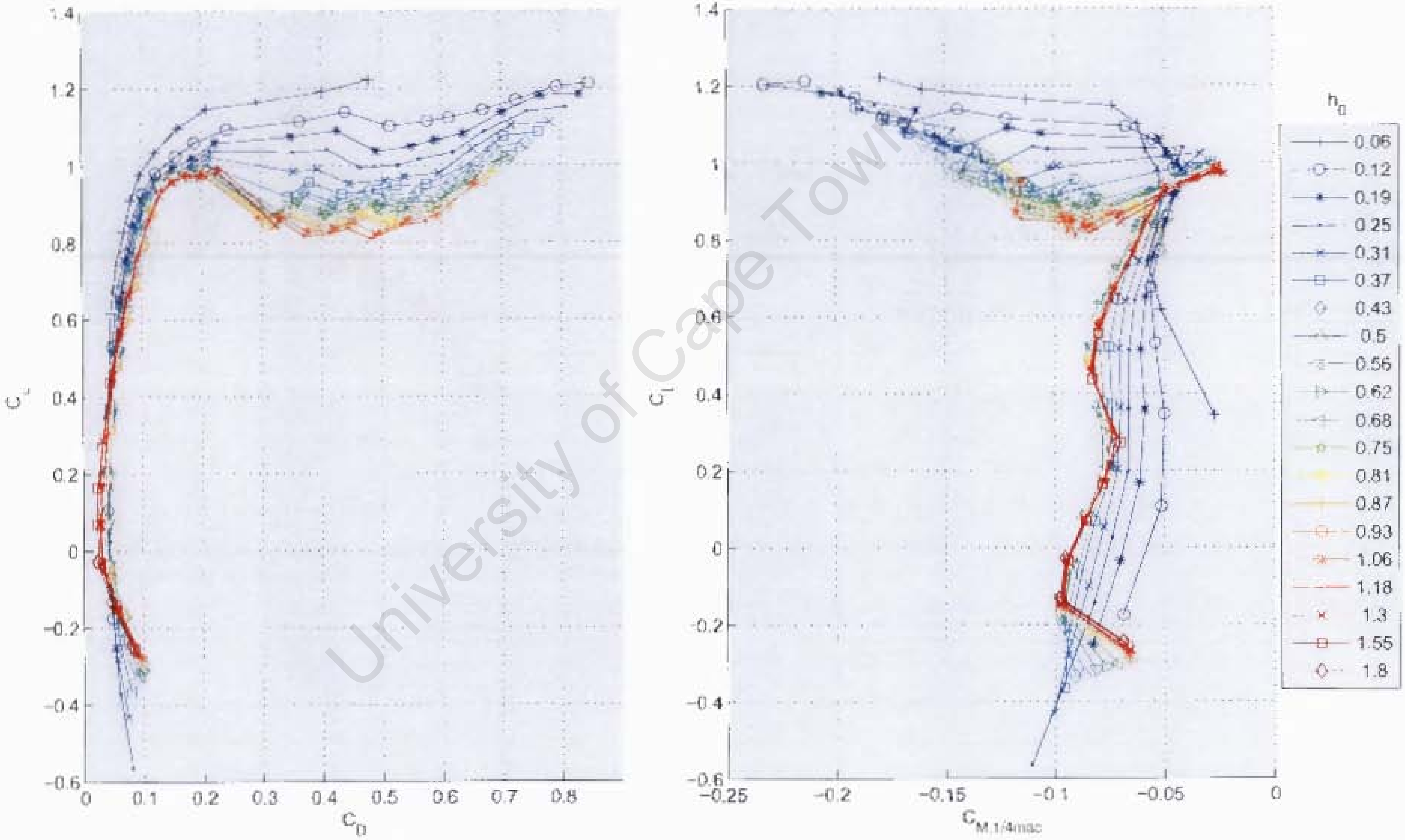

Figure A.9: Polar Diagrams

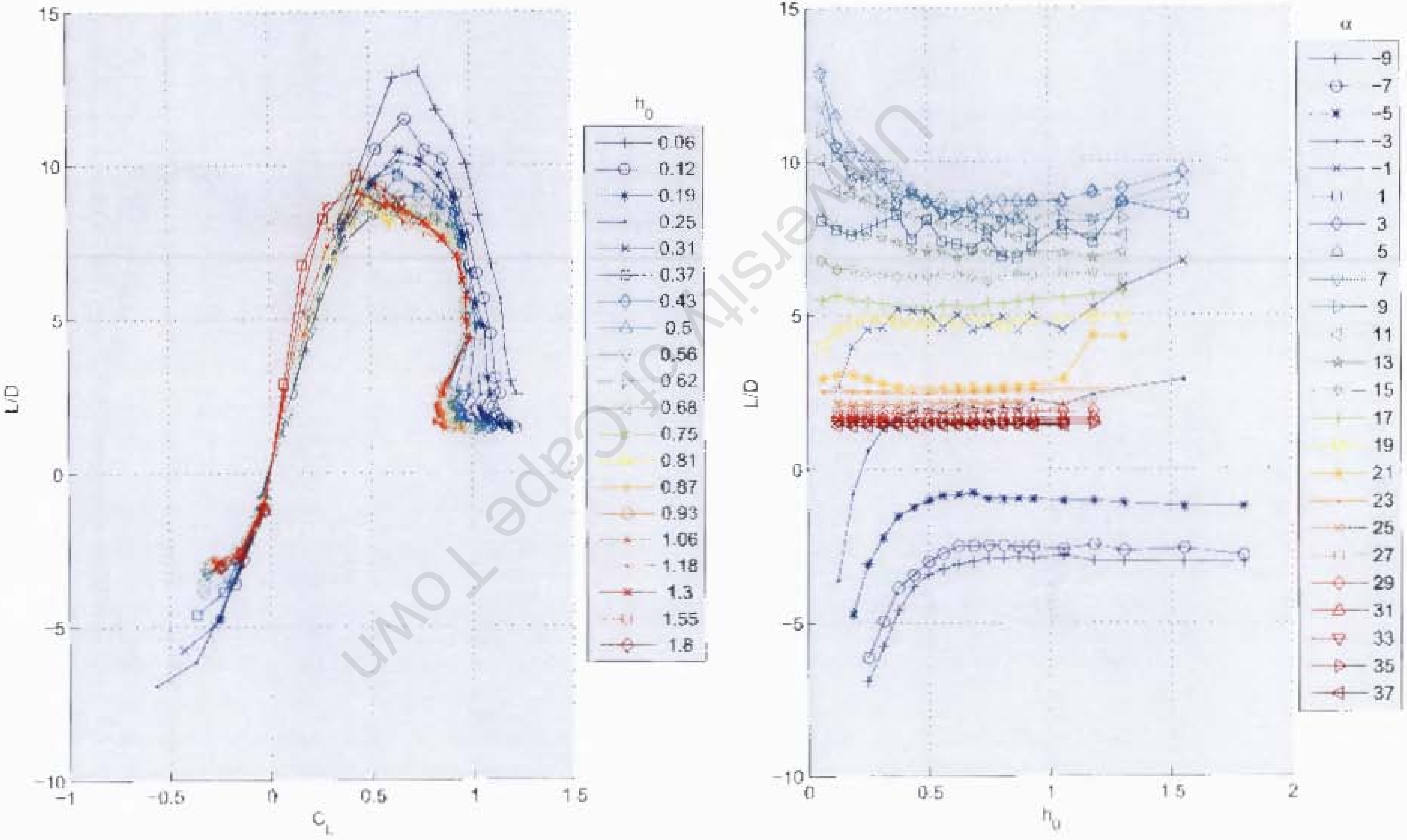

Figure A.10: L/D vs. C_l and h_0

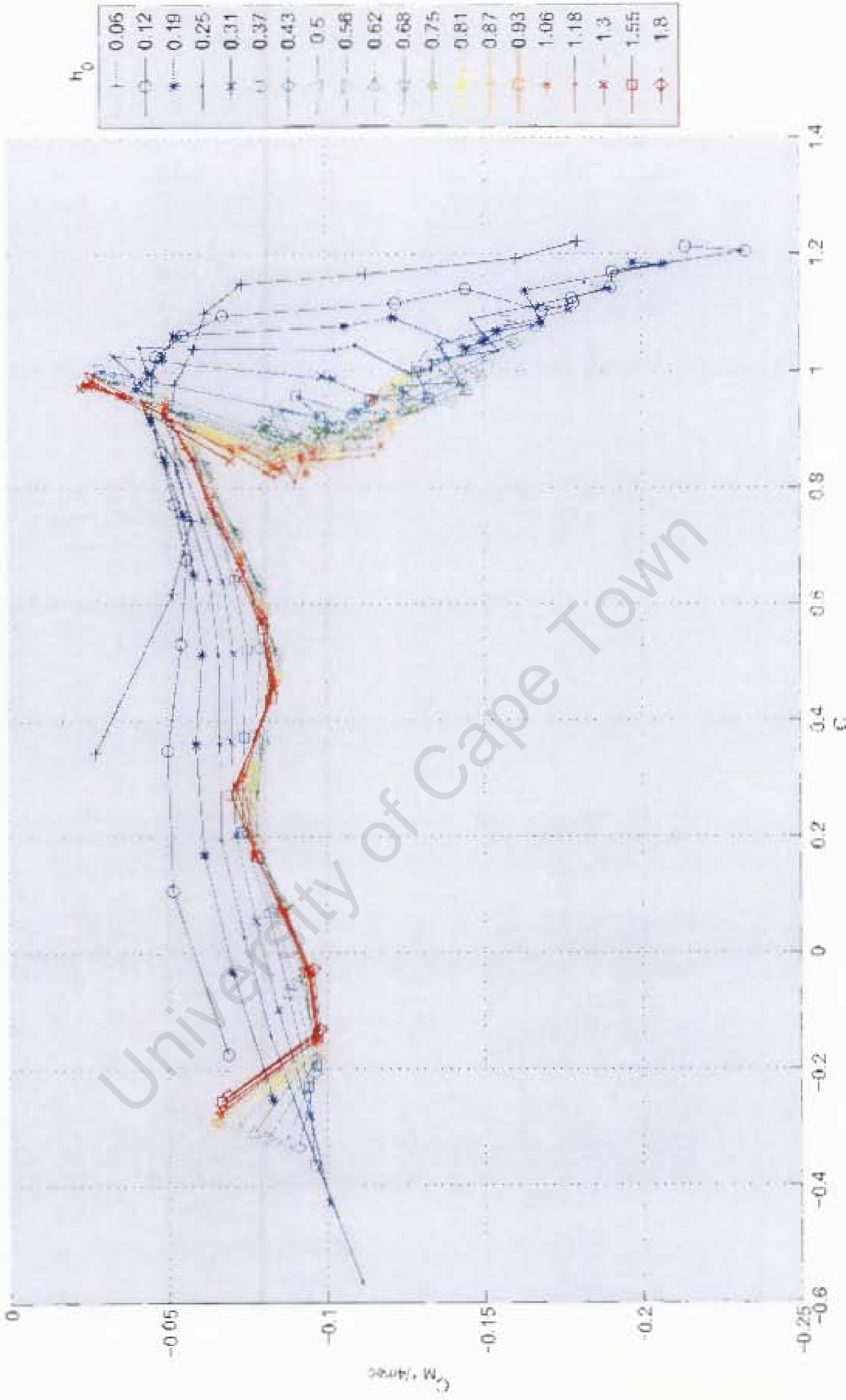

Figure A.11: C_M *vs.* C_L for constant values of h_0

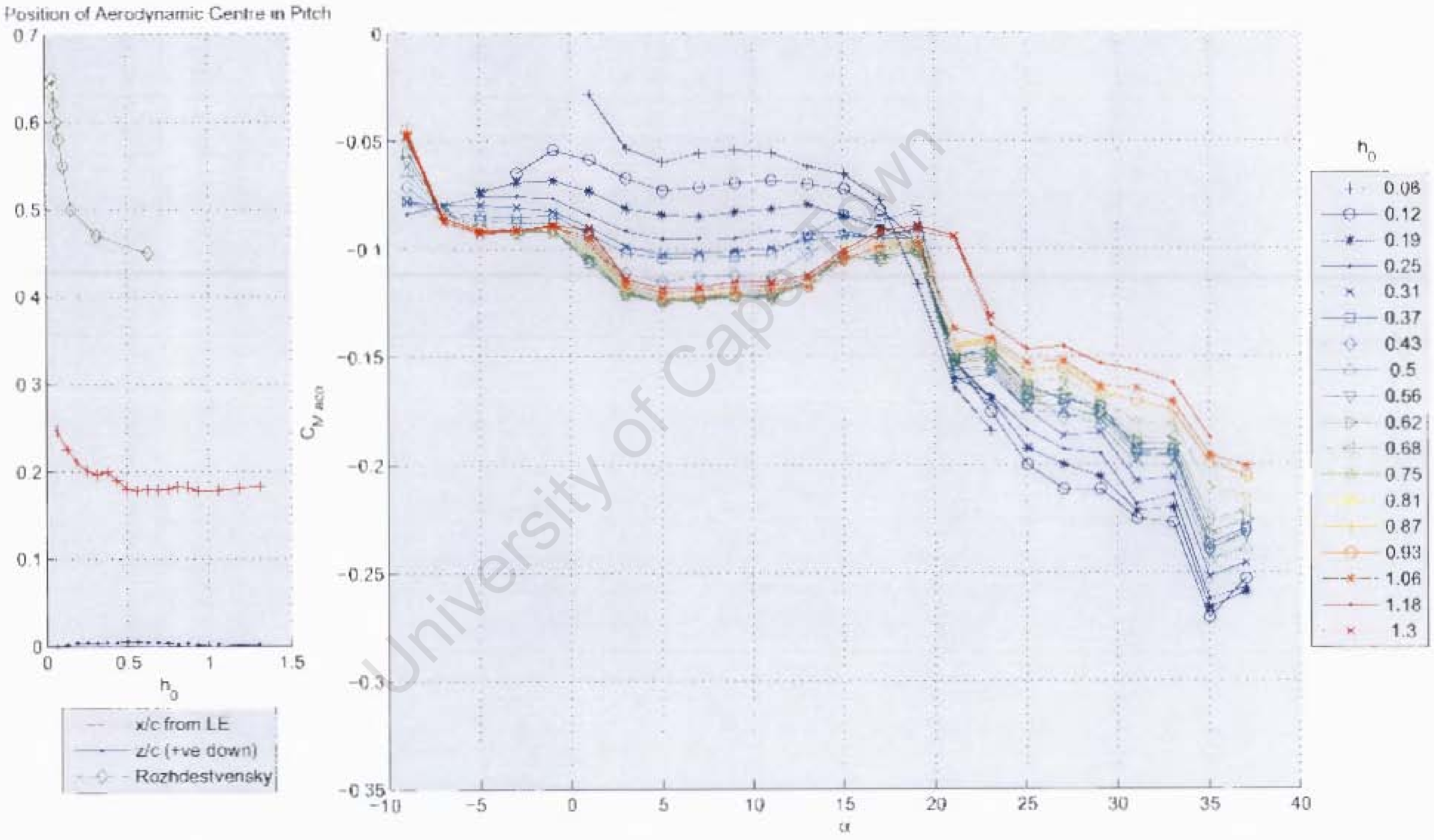

Figure A.12: Variation of aerodynamic centre in pitch with ground clearance

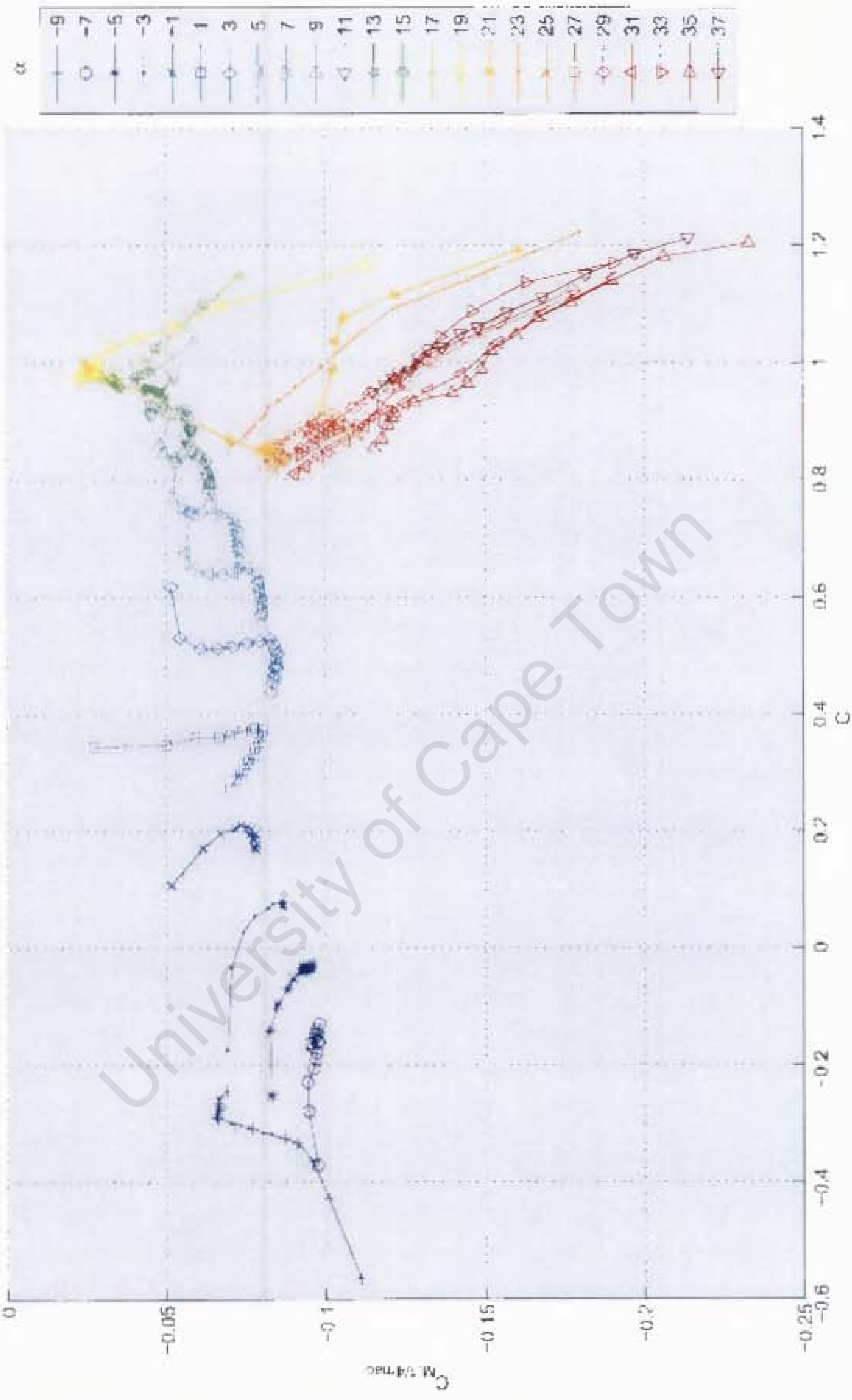

Figure A.13: C_M *vs.* C_L for constant values of α

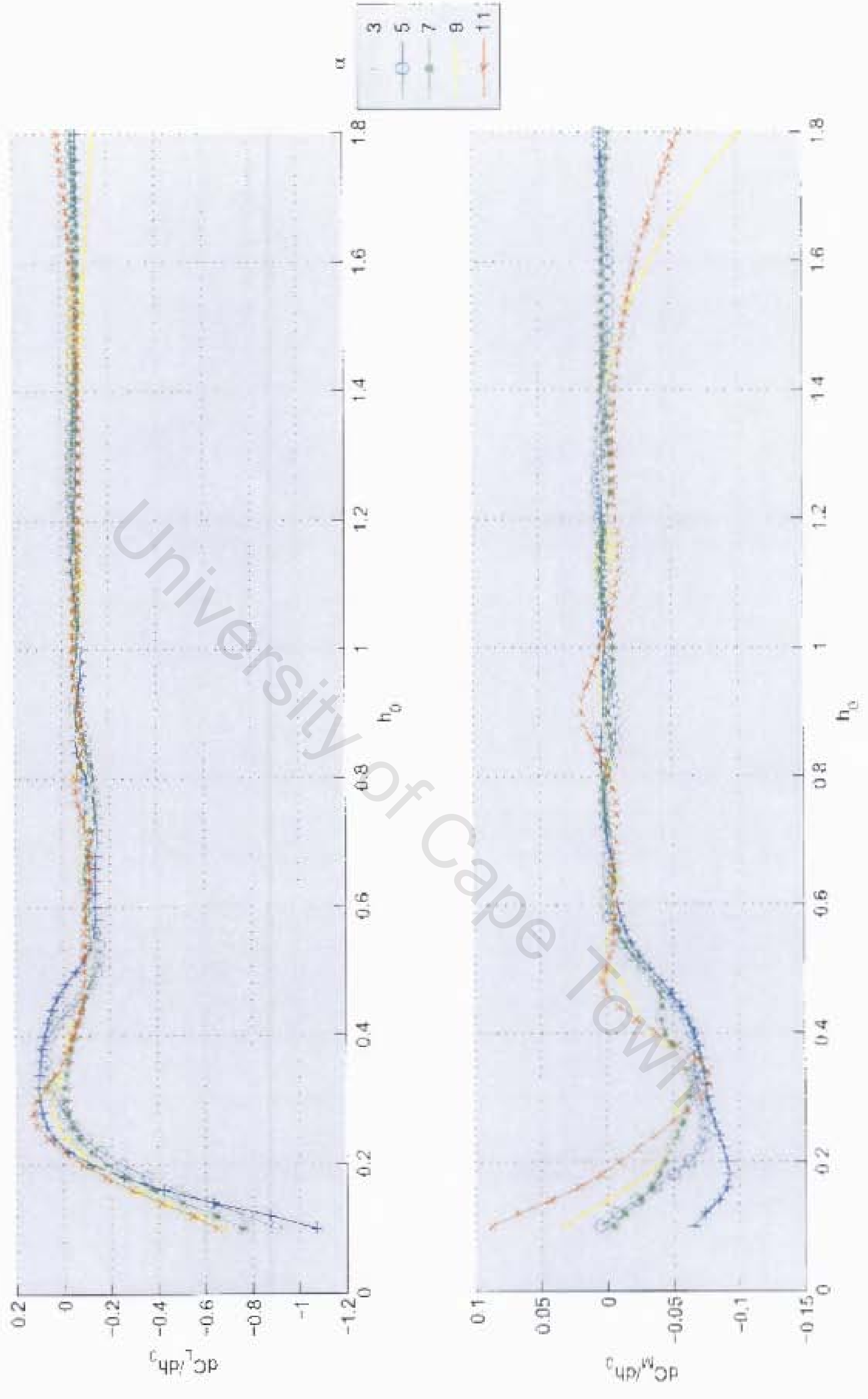

Figure A.14: $\partial C_L/\partial h_0$ and $\partial C_M/\partial h_0$ vs. h_0

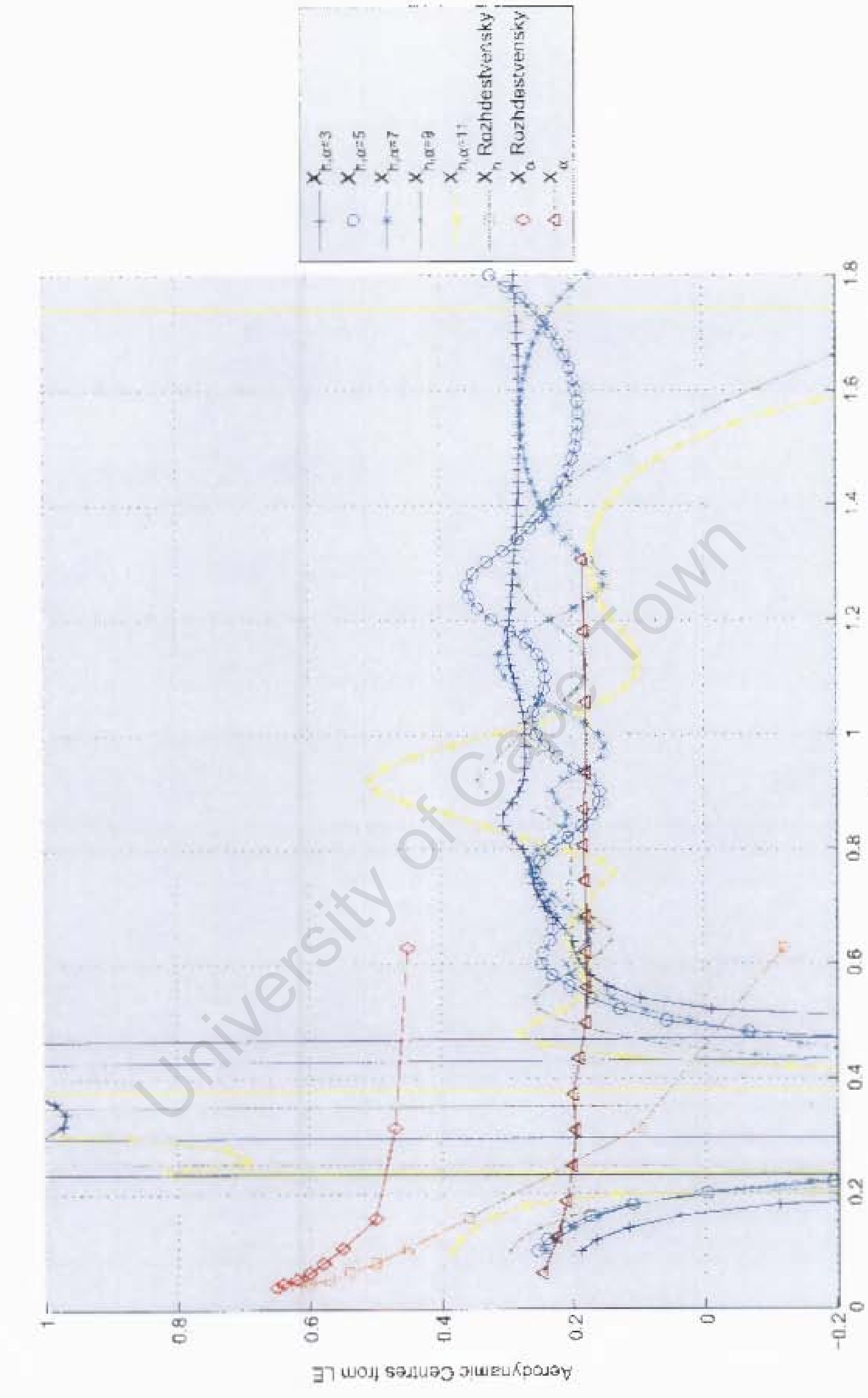

Figure A.15: Variation of aerodynamic centre in height with ground clearance

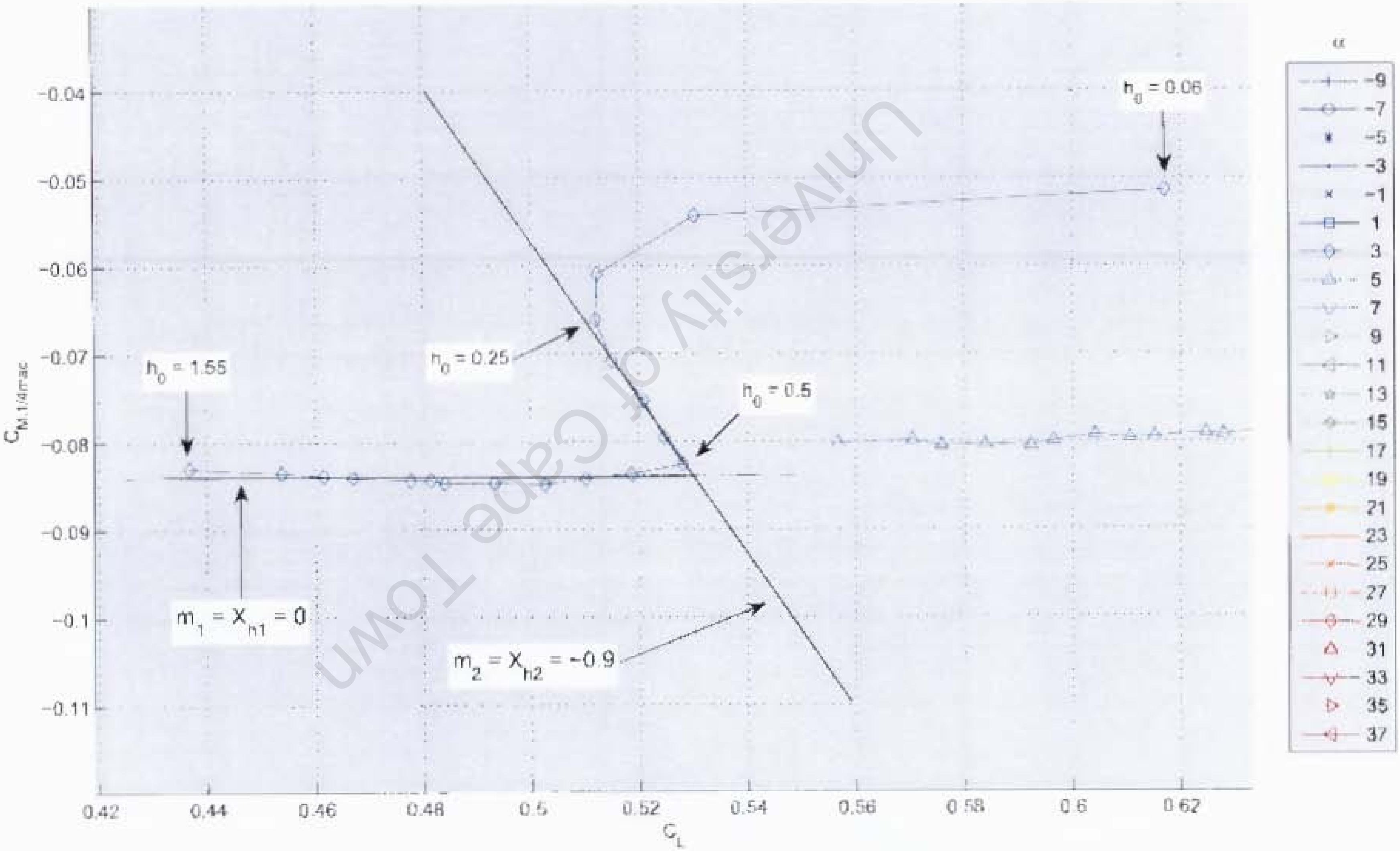

Figure A.16: $(C_M \text{ vs. } C_L)_{h\alpha=3}$

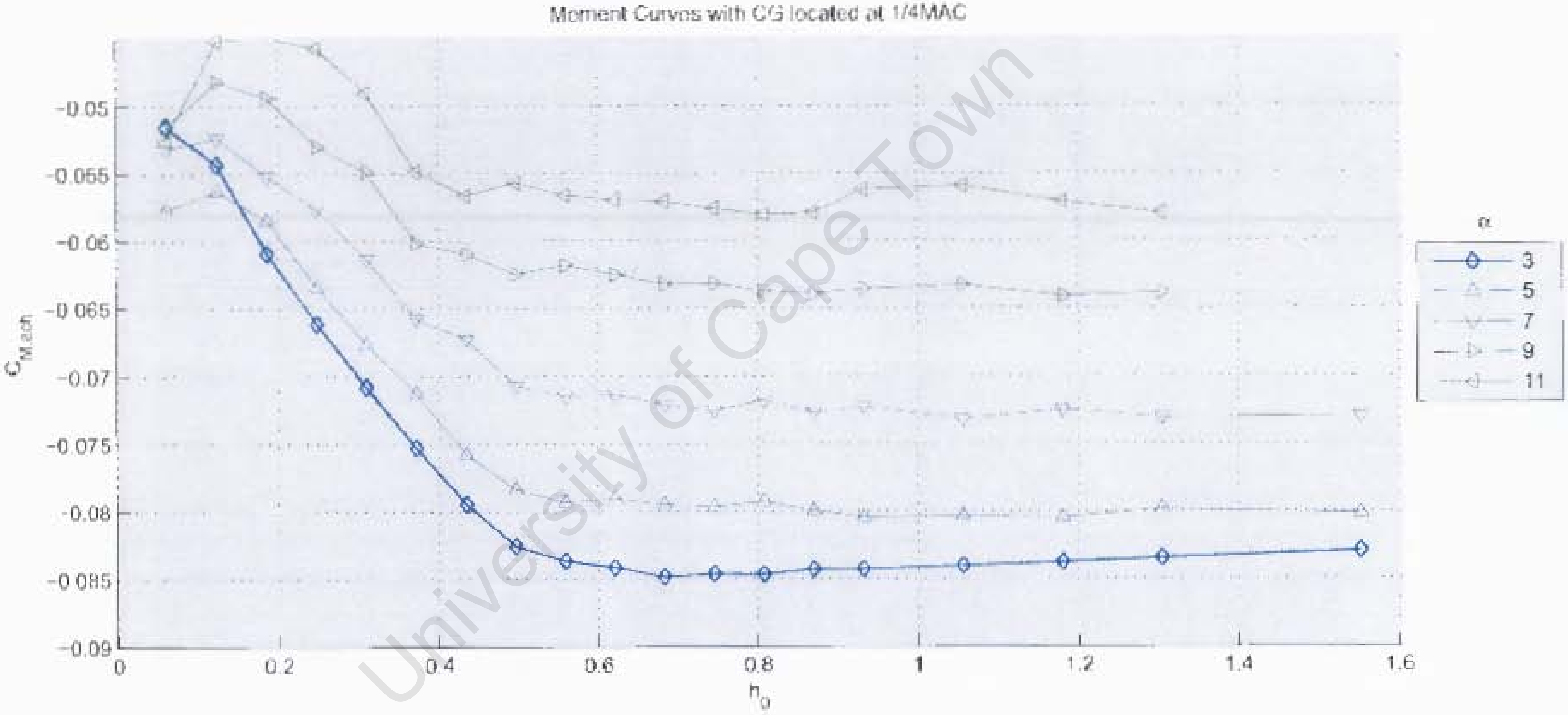

Figure A.17: C_{Mach1} vs. h_0

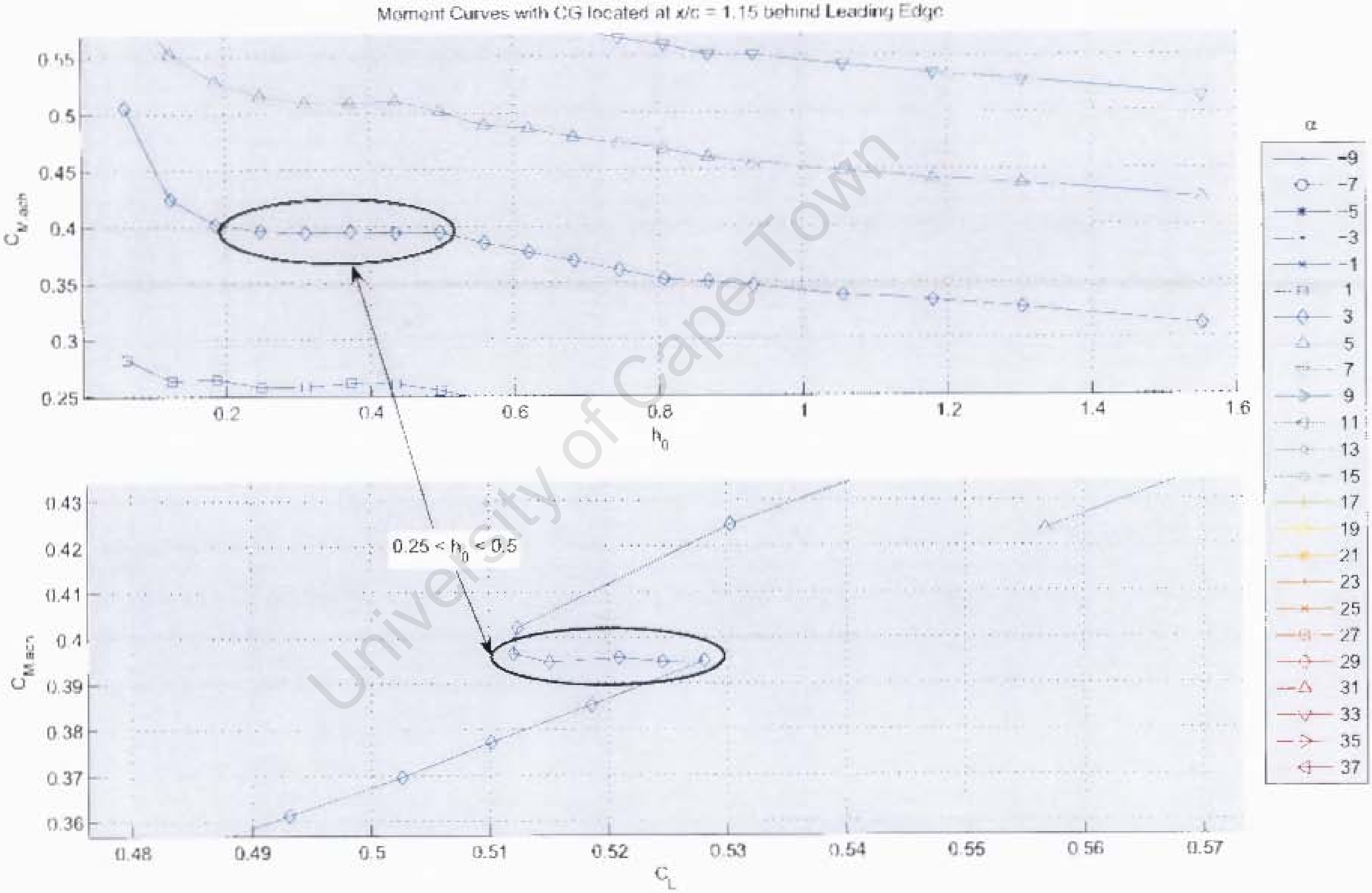

Figure A.18: C_{Mach2} vs. h_0 and C_L

Appendix B

The DHMTU Airfoil

The DHMTU airfoil was developed by the Department of Hydromechanics of the Marine Technical University in St. Petersburg. They were developed specifically for use in ground effect. The airfoils are generally characterised by a flat section on the lower surface of the wing, and an S-shaped mean line. The airfoils are not defined by a mean line and a thickness distribution, as with the NACA profile, but by separate definitions for the upper and lower surface. The DHMTU sections have eight defining parameters, one for the nose radius, four for the lower surface and three for the upper surface. The general designation of a DHMTU airfoil is given as:

$$DHMTU\ a - b - c - d - e - f - g - h$$

where;

- a = maximum ordinate of the upper surface (%c)
- b = position of the maximum ordinate (%c)
- c = ordinate of the start of the flat section (%c, below the horizontal is positive)
- d = position of the start of the flat section (%c–)
- e = ordinate of the end of the flat section (%c, below the horizontal is positive)
- f = position of the end of the flat section (%c)
- g = slope parameter of the upper trailing edge
- h = nose radius parameter

The airfoil used in these experiments had a span of 465 mm, an aspect ratio, $AR = 3$, was chosen. This gave a chord length of $c = 155\,mm$. A $DHMTU$ $10-40-2-10-2-60-21-5$ wing profile was arbitrarily chosen for these experiments and is shown in figure B.1. This wing was relatively slender with a 10% maximum thickness at 40% chord. The wing had a flat section on the lower surface from 10% to 60% chord and a nose radius parameter of 5.

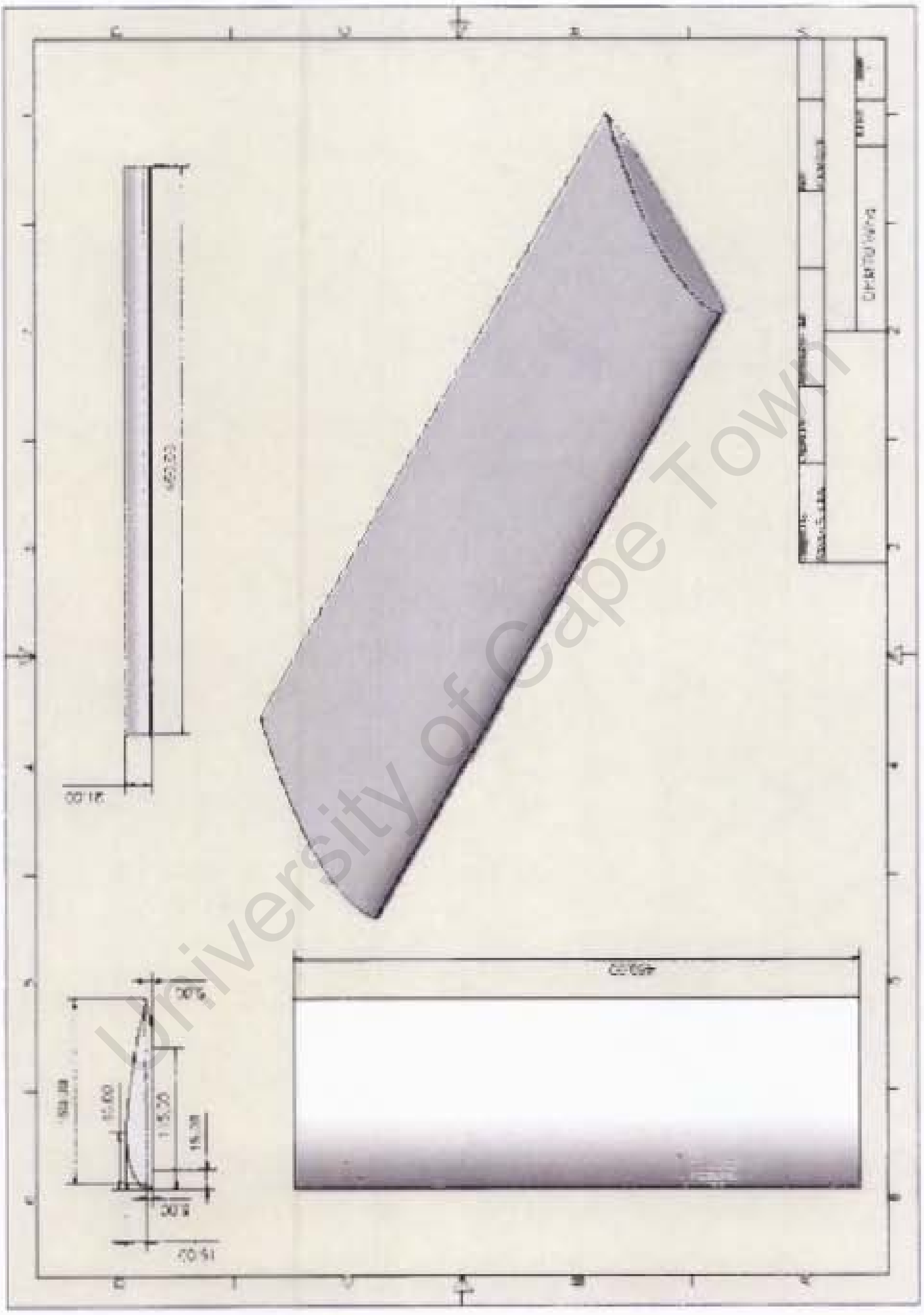

Figure B.1: Design Drawings of $DHMTU$ $10-40-2-10-2-60-21-5$

Appendix C

Design Drawings

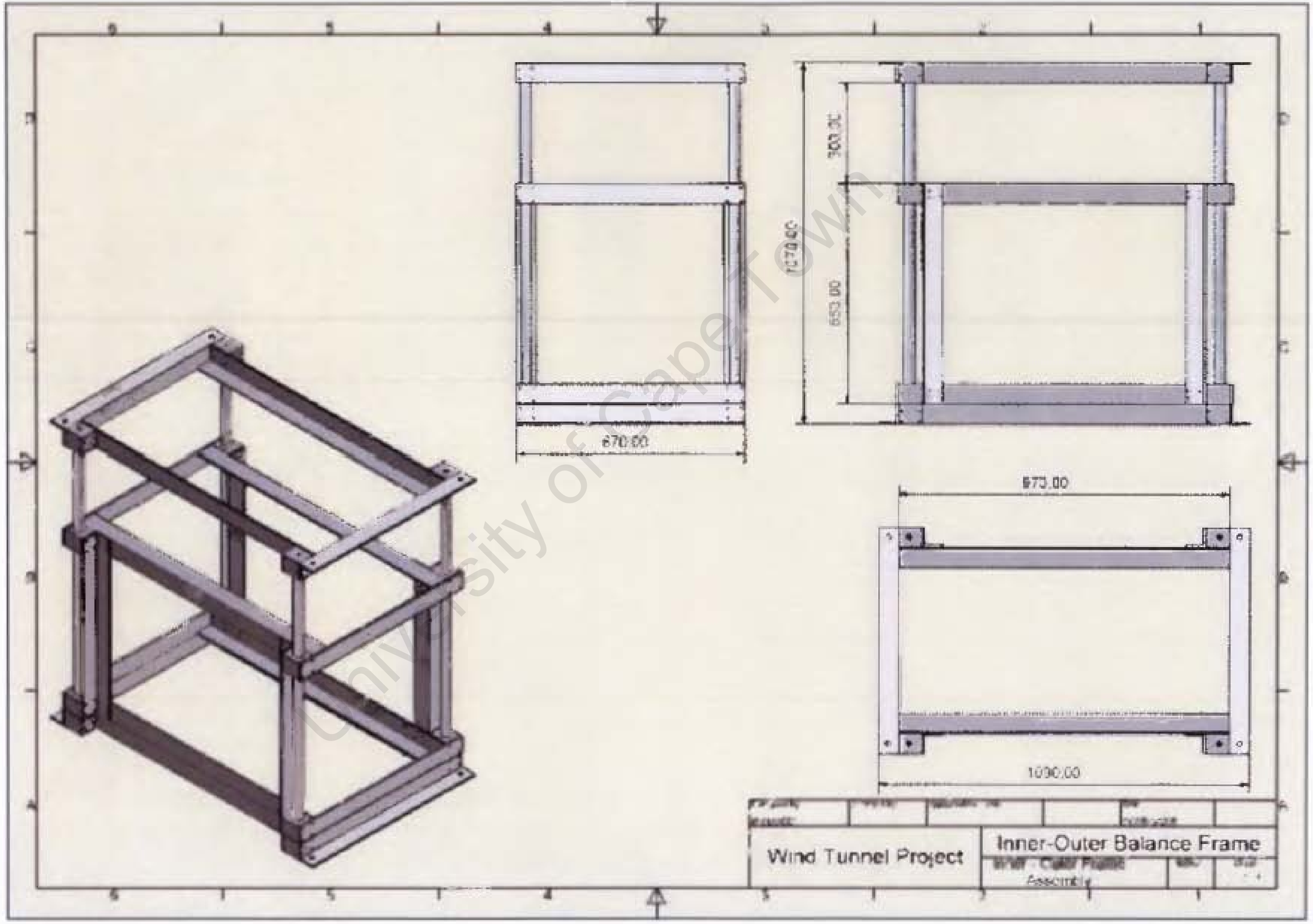

Figure C.1: TEM Balance Elevator

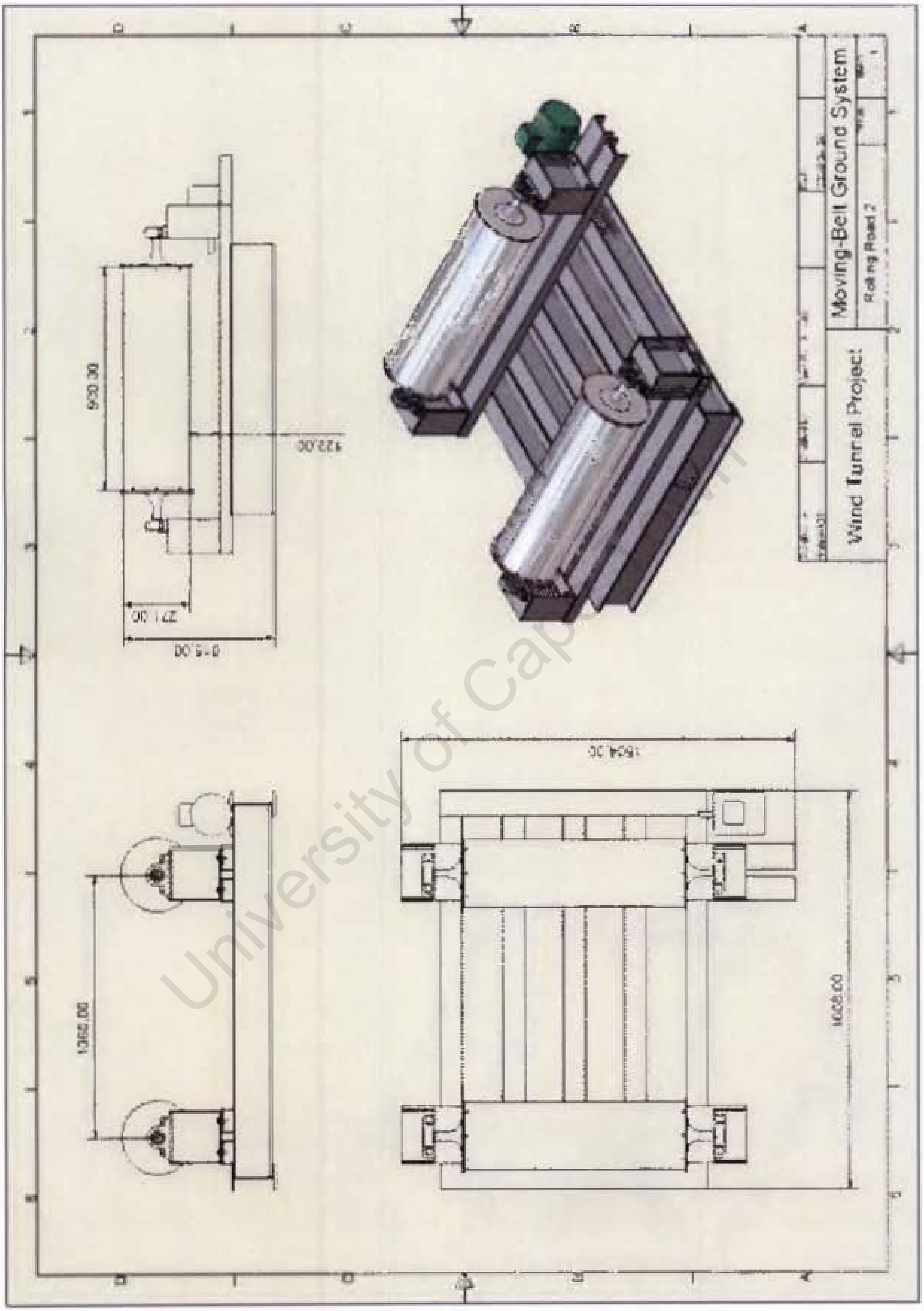

Figure C.2: Moving-Belt Ground System

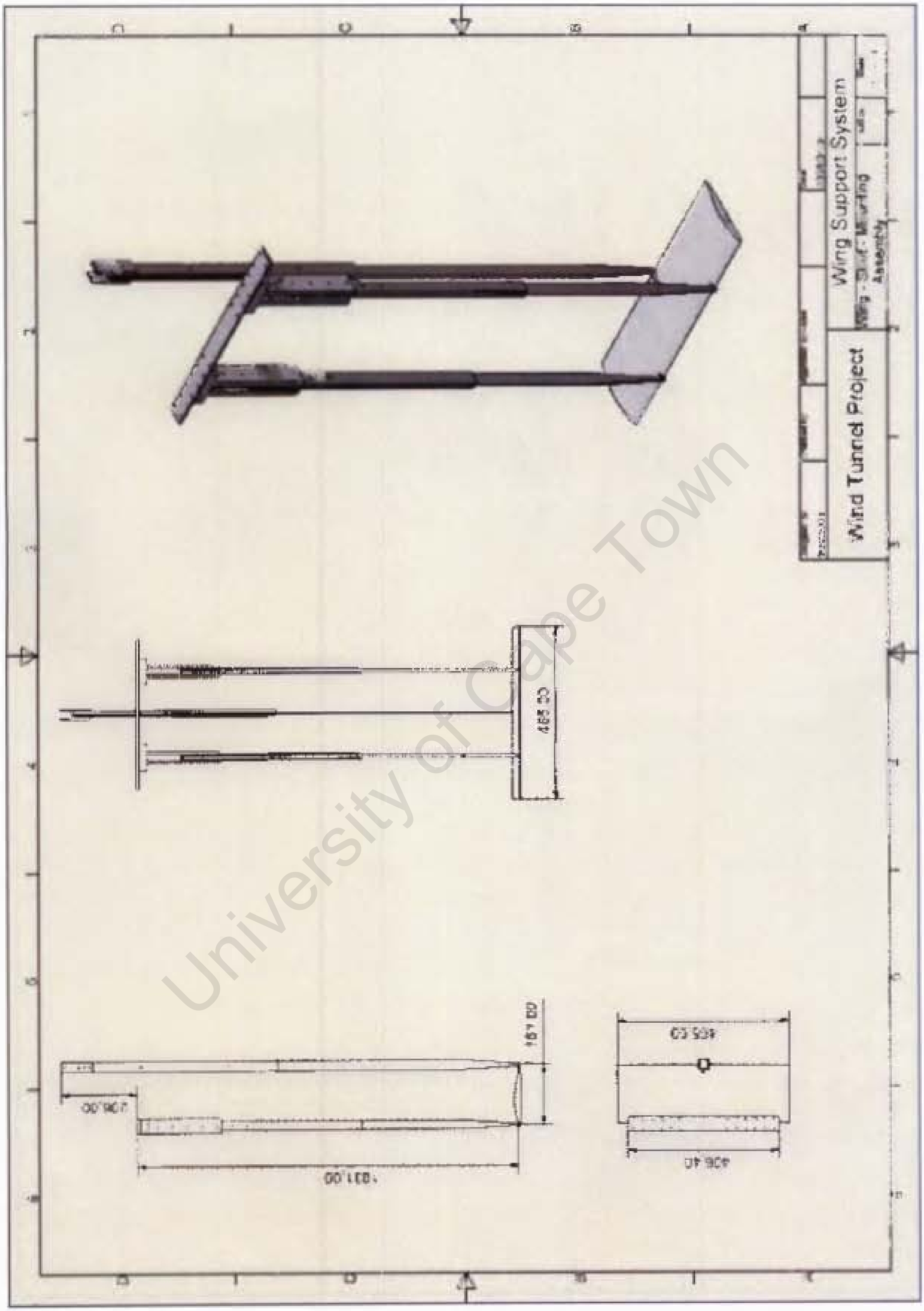

Figure C.3: Wing Support System

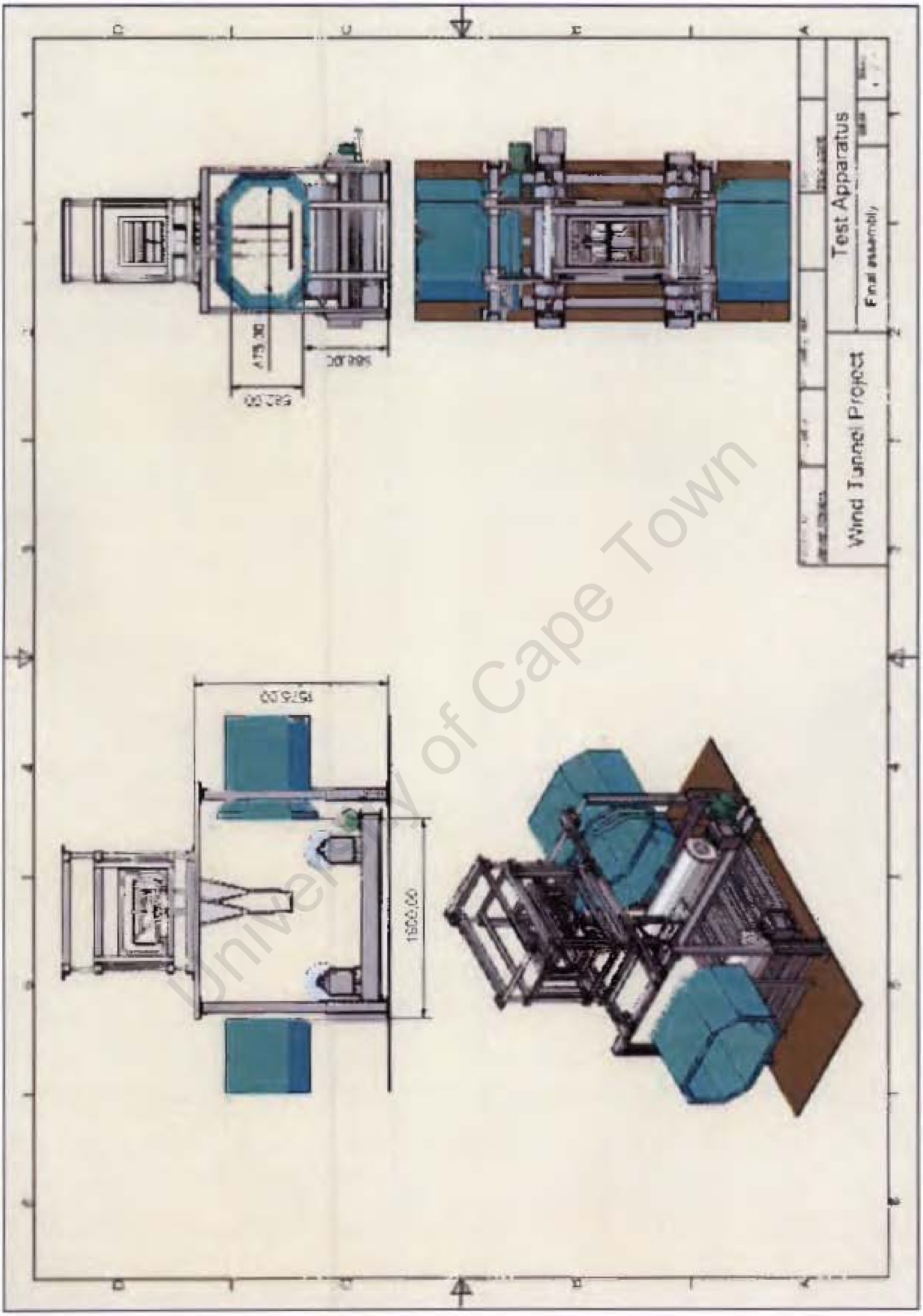

Figure C.4: Final Tunnel Assembly

Appendix D

Matlab Code

Included on CD

Appendix E

Data

Included on CD